DEVELOPMENT OF A CONTROLLED-RELEASE PLATFORM FOR INVESTIGATION OF PROTEASES FOLLOWING ROTATOR CUFF TEAR

A Dissertation

Presented to

The Academic Faculty

by

Elda Alicia Treviño

In Partial Fulfillment

of the Requirements for the Degree

Doctor of Philosophy in the

Department of Biomedical Engineering

Georgia Institute of Technology and Emory University

August 2020

DEVELOPMENT OF A CONTROLLED-RELEASE PLATFORM FOR INVESTIGATION OF PROTEASES FOLLOWING ROTATOR CUFF TEAR

Approved by:

Dr. Johnna S. Temenoff, PhD, Advisor
Department of Biomedical Engineering
Georgia Institute of Technology and Emory University

Dr. Manu O. Platt, PhD
Department of Biomedical Engineering
Georgia Institute of Technology and Emory University

Dr. Nick J. Willett, PhD
Department of Biomedical Engineering
Georgia Institute of Technology and Emory University

Dr. Edward A. Botchwey, PhD
Department of Biomedical Engineering
Georgia Institute of Technology and Emory University

Dr. Hicham Drissi, PhD
Department of Orthopaedics
Emory University

Date Approved: 05/29/2020

Dedicated to Mom and Dad for without you

both none of these words would be here.

Dedicated to Lorena who walked this

arduous journey alongside me.

ACKNOWLEDGEMENTS

I would first like to thank my committee for encouraging me to develop the knowledge and skills that would make me worthy of an advanced degree. I would like to extend a special acknowledgment to my advisor, Johnna Temenoff, who made all this work possible. Thank you for patience, encouragement, and mentorship. Your guidance has allowed me to develop the skills and connections I needed for the next stage of my career. I would also like to thank Dr. Nick Willett, Dr. Edward Botchwey, and Dr. Hicham Drissi for their insight and probing questions that allowed me to think more broadly about my thesis work. Lastly, I would also like to thank Dr. Manu Platt allowing me to work and learn in his laboratory space, which allowed me to master gelatin zymography, which was vital to this thesis work. Thank you for teaching to ask more probing questions about the world around me and giving me a deep appreciation for the role proteases play in our body. Finally, thank you for enlisting me to work with you outside of the laboratory. I really enjoyed helping with the various programs you have developed and supported within our department and across Georgia Tech. Your dedication to fostering student development both inside and outside of the laboratory is admirable and your commitment to supporting underrepresented minorities in higher education has inspired me to adopt similar goals in the future.

I would be remiss if I didn't also take this opportunity to acknowledge the contributions of several mentors at The University of Texas at Austin. I would first like to thank Dr. Laura Suggs who encouraged me to apply for the TREX program and for allowing me to work in her laboratory for three years. Dr. Suggs was incredibly

supportive and wrote countless letters of recommendation on my behalf. I would also like to thank my graduate student mentor Dr. Laura Ricles for her patience and mentorship. Laura was always very kind to me and modeled how to have a successful career in graduate school. Lastly, I would like to thank my Ronald E. McNair advisor, Dr. James Brown, otherwise known as the godfather of physics. Dr. Brown and the McNair program were instrumental in preparing me to successfully apply for graduate school. Even after my accepting the offer at Georgia Tech, Dr. Brown frequently checked in on me and reminded me that I had the potential to earn the PhD at the end of my name.

I would like to thank members of the Temenoff laboratory past and present. Thank you to Jen, Torri, and Liane for helping me at the start of my graduate school career. In particular, I would like to thank Torri for treating me like a contributing member of the laboratory and always taking the time to talk with me about both science and life. I would like to extend a special thank you to Jennifer McFaline-Figueroa, who was the laboratory manager when I started my graduate work in the Temenoff laboratory. Jennifer and I became great friends and have kept in touch after she left to pursue her own advanced degrees. I would not have been able to accomplish everything in my very first author paper without fundamental work that she did for the laboratory. I want to thank Jennifer for keeping me sane during late summer nights with pizza and Beyoncé dance parties. I would also like to thank Jimmy Shah, the undergraduate student I had the honor and privilege to mentor in our laboratory. Jimmy was such an incredibly hard worker and was constantly asking very insightful questions that kept me on my toes. He was an absolute joy in the laboratory, and I am so thankful that he was around to help me develop the microfluidic device outlined in chapter 4 of this dissertation.

Furthermore, I would like to thank my current Temenoff lab mates: Molly, Joe, Gilad, Leah, Nettie and Zoe. I would like to thank Molly for being such an incredible post-doc to our laboratory. Her value and contribution cannot be quantified. She is incredibly knowledgeable and was always willing to help in whatever way she could, and I am so grateful for her. She will go on to become an incredibly accomplished faculty member and I envy the students she will have the opportunity to mentor. While Joe is relatively new in the group, I would like to thank him for his calm disposition and for his patience with me and my last minute orders. Joe has been a great addition to our group, and I am glad we had the opportunity to cross paths and get to know one another. I would like thank Gilad for being a good lab mate and helping with me with surgeries when he could. I would like to thank Leah, who has become a wonderful friend and confidant during my time in graduate school. I am so thankful to her for always willing to help me with surgeries or to be a sounding board to talk through unexpected data or difficulties in my personal life. Her friendship significantly improved my time in graduate school (*$p<0.05$). I would like to thank Nettie B. for inspiring me to be my authentic self all the time. Nettie's smile and humor are infectious and her presence in *T - LAB* has only had overwhelmingly positive results. Last but certainly not least, I would like to thank Zoe for being a wonderful friend and lab mate. I could always count on Zoe for a fun chat or unwavering support and encouragement when I had encountered difficulties and was feeling down. I am so thankful that I had the opportunity to form these friendships with my lab mates. It is an incredible feeling knowing that the people you work with have your best interests at heart and genuinely care for you and your wellbeing. I feel very lucky to have known each of you and I will miss our chats and laughs very much.

I would like to extend a special thanks to Dr. Akia Parks and Dr. Simone Douglas for sharing their “Platt Lab Magic” with me. While many graduate students are made to work with one another, I am thankful that we became real friends and cheered one another on as we struggled and overcame this PhD. I would also like to thank my friend, Fabrice Bernard, for all his help with the near infrared imaging and analysis in chapter 5 of this work. Thank you for your seemingly infinite patience with me in completing this study. Finally, I would like to thank Dr. Chunlei Zhu and Dr. Younan Xia for their help in developing our novel microfluidic device in chapter 4 of this dissertation work.

To my friends at Georgia Tech, I would like to extend my heartfelt gratitude for lifting me up when I was down and cheering me on when I was up. My graduate school experience has been shaped by your friendships. Specifically, I would like to thank Sandra, my *comadre* and very first graduate school friend. I am so glad I racially profiled you on Day 1 because it resulted in our beautiful friendship. To Shaquia, I treasure your friendship and I am so happy that I have gotten to know you as a friend, scientist, wife, and mother. To my long-time friend, Marissa, I am so glad that we had the opportunity to get to know one another better once we got to Georgia Tech. It was amazing to have a fellow Texan to commiserate with and I thoroughly enjoyed your recurring appearances in the Temenoff office space for gossip and chit chat. Finally, to the other two-thirds of the triple threat lunch team, Ian and Nusaiba, you both have been so instrumental in getting me through this final stretch of graduate school. I cannot thank you both enough for being the two amazing humans you both are.

To my friends at Emory, or more affectionately known as the Party People™, I would like to thank each of you for your friendship, jokes, and willingness to chant to just

about anything. You all have essentially been an assortment of additional parents to Lorena and I love you all for it. Specifically, I would like to thank Jessie and Roxana for inviting me to Girl's Night shortly after Edgar and I started dating. I was incredibly nervous about making a good impression but you both have given me so much love and support that imagining my life without you two is incomprehensible. I would also like to thank Jackie and Caro for their love and friendship. You both are wildly passionate, smart, incredible women and I am so thankful to call you both friends. Last but certainly not least, I would like to thank the fedora boiis, Luis and Seyi. Thank you for treating me like a friend and not just Edgar's girlfriend. You both are incredibly funny, wonderful guys and I'm very glad I know you both. *Tips fedora*

I would like to extend a particularly special acknowledgement to my partner, Edgar Sherman, who has witnessed my every triumph and failure in both life and lab. Thank you for keeping me grounded and reminding me that I am a smart, capable, strong independent woman who don't need no man. Thank you for your unwavering love and support over these (almost) four years. I definitely could have done it without you, but I'm glad I didn't have to. You have brought so much love, joy, and laughter into my life. You are my best friend and I love you very much.

Finally, I would like to thank my family, who have relentlessly loved and supported me throughout my life. Thank you to my mother, Sylvia Treviño, for ensuring that I developed her same work ethic and resilience. Thank you to my father, Arnoldo Treviño, who is the best man I know. Thank you for always supporting me and believing in me. Thank you to you both for making countless sacrifices and always ensuring that Lorena and I were always well taken care of. I would also like to extend gratitude to my

brother, Arnold, for supporting me and cheering me on while he also worked towards an advanced degree. With two doctors in the family, we have given our family a lot to brag about. Lastly, I would like to thank my daughter, Lorena Sylvia Treviño. Thank you for being the most wonderful child a mother could ask for and accompanying me on this very long, arduous journey called graduate school. When we first moved to Atlanta, you were just a tiny cute first-grader, but over these many years I have seen you grow into an incredible young woman. You are a tough, hilarious, intelligent person and I am incredibly proud of you. I love you so very much, Lorena.

TABLE OF CONTENTS

LIST OF TABLES

LIST OF FIGURES

LIST OF SYMBOLS AND ABBREVIATIONS

AcCl	Acryloyl Chloride
AF633	Alexafluor633
ApMAm	N-(3-Aminopropyl) Methacrylamide Hydrochloride
BCA	Bicinchoninic Acid Assay
CT	Computed Tomography
DTT	Dithiothreitol
E-64	Trans-Epoxysuccinyl-L-Leucylamido(4-Guanidino)Butane
ECM	Extracellular Matrix
EDC	1-Ethyl-3-(3-Dimethylaminopropyl)-Carbodiimide
EDTA	Thylenediamine Tetraacetic Acid
EVA	Ethylene-Vinyl Acetate
GAG	Glycosaminoglycan
H&E	Hematoxylin And Eosin
Hep-MAm	Heparin-Methacrylamide
LHBT	Long Head Biceps Tendon
Mam	Methacrylamide
MMP	Matrix Metalloproteinases
MRI	Magnetic Resonance Imaging
Na_2HPO_4	Disodium Phosphate
NaH_2PO_4	Monosodium Phosphate
NIH	National Institute Of Health
NIR	Near Infrared
NMR	Nuclear Magnetic Resonance
NSAID	Nonsteroidal Anti-Inflammatory Drug
OCT	Optical Cutting Temperature

PBS	Phosphate Buffered Saline
PCL	Poly(E-Caprolactone)
PDMS	Poly(Dimethyl Siloxane)
PEG	Poly(Ethylene Glycol)
PEG-4MAL	4-Arm Poly(Ethylene Glycol)-Maleimide
PEGDA	Poly(Ethylene Glycol) Diacrylate
PEGMMA	Poly(Ethylene Glycol) Monomethacrylate
PLA	Poly(Lactic Acid)
PLGA	Poly(DL-Lactic-Co-Glycolic Acid)
PRL	Physiological Research Laboratory
PVA	Poly(Vinyl Alcohol)
PVC	Poly(Vinyl Chloride)
ROI	Region of Interest
SHG	Second Harmonic Generation
Sulfo-NHS	N-Hydroxysulfosuccinimide
TIMP	Tissue Inhibitor Of Metalloproteinases
UV	Ultraviolet
wt%	Weight Percent
µCT	Micro- Computed Tomography

SUMMARY

Surgical reattachment of torn rotator cuff tendons has a high rate of re-tear (failure) and the procedure does not reverse joint tissue degeneration present at the time of surgery. Following rotator cuff tear, three different joint tissues (tendon, muscle, and articular cartilage) develop degenerative changes. A possible cause for the extensive joint tissue degeneration observed following rotator cuff tear is the prolonged activation of proteases, which are specialized enzymes whose primary function is to degrade proteins. Systemic delivery of several protease inhibitors have been tested in human clinical trials to for a variety of diseases including osteoarthritis and osteoporosis, but all have been abandoned due to off-target effects. However, local delivery of protease inhibitors could reduce disease progression without deleterious side effects.

The long-term goal of this dissertation was to understand how proteases contribute to joint tissue degeneration (tendon, muscle, and cartilage) after rotator cuff tear. Understanding the spatial and temporal distribution of upregulated proteases after rotator cuff tear can best inform therapeutic treatments to prevent degeneration, which would result in improved surgical outcomes after rotator cuff tear re-attachment surgery. First, using a rat model of rotator cuff tear that has been shown to replicate degenerative damage seen in humans, we investigated active proteases in each joint tissue over time. Second, we designed a novel microfluidic device to fabricate uniformly sized microparticles that can be loaded with protease inhibitors for subsequent use *in vivo*. Also, we reinvented a currently available fluorogenic substrate assay for the detection of E-64 (a broad, small molecule cathepsin inhibitor), which was our desired therapeutic. Lastly, we tested our E-64 loaded microparticles system on supraspinatus tendon tissue in

our rat model of rotator cuff tear as a test bed to elucidate the effect of sustained release of a broad cathepsin inhibitor on active proteases.

CHAPTER 1 INTRODUCTION

1.1 Motivation

Rotator cuff tears, including partial and full-thickness tears of the supra- and infraspinatus tendons, are among the most common shoulder injuries. It is estimated that approximately 34% of the population has a partial or full-thickness tear [1]. Following rotator cuff tear, all of the joint tissues are affected including the tendon, its respective muscle, and articular cartilage. After rotator cuff injury, tendon becomes disorganized with decreased collagen content [2], while muscle atrophies and is infiltrated with fibrous tissue and fatty deposits [3]. Additionally, the force balance between tendons of the rotator cuff is disrupted, which may lead to the development of osteoarthritic changes in the articular cartilage including loss of glycosaminoglycan (GAG) content, increased surface roughness, and loss of cartilage tissue [4,5].

Rotator cuff tear treatment includes use of nonsteroidal anti-inflammatory drugs (NSAIDs), physical therapy, and possibly surgical reattachment of the torn tendon. Surgical re-attachment includes stitching the torn tendon onto the humeral head bone via a bone tunnel. It is considered to be a very painful procedure and has variable documented re-tear rates from 30-94% [6,7]. Surgical re-attachment of the tendon aims to restore the force balance between tendons of the shoulder but does not reverse or halt degeneration that has already occurred in the tendon, its respective muscle, or articular cartilage. Additionally, there is a positive correlation between the level of degeneration in the muscle at the time of re-attachment and re-tear rates [8].

A possible cause for the extensive joint tissue degeneration observed following rotator cuff tear is the prolonged activation of proteases. Proteases are specialized enzymes whose primary function is to degrade proteins. Of particular interest are cysteine cathepsins and matrix metalloproteinases (MMPs), which play a role in many facets of homeostasis within the human body including extracellular matrix remodeling, bone resorption, and intracellular protein turnover [9–11]. However, these two families of proteases have also been observed to be upregulated in a variety of degenerative diseases in orthopaedics, including atrophy of the tibialis anterior muscle [12], osteoarthritis of the knee [13], and tendinopathy [14,15]. This work specifically investigated both cathepsin and MMP families of proteases in joint tissues after rotator cuff tear to better understand how they may contribute to characteristic degeneration seen after injury.

The implication that proteases are a potential cause for tissue degeneration in musculoskeletal diseases makes protease inhibitors an appealing potential treatment. Several protease inhibitors have been tested in human clinical trials to treat dysregulated cathepsins and MMPs, but all have been abandoned due to off-target effects [16,17]. These clinical trials have tested the safety and efficacy of protease inhibitors using systemic delivery, meaning both healthy and diseased tissues are equally exposed to the therapeutic treatment. As mentioned previously, proteases play a variety of roles in the human body and thus are not localized to any one area of the body. Consequently, regulated proteases in healthy tissue may be inhibited and prevented from performing their normal functions, causing negative side effects including headache, gastrointestinal disturbance, lung fibrosis, and skin lesions [16]. Moreover, systemic delivery requires a much larger amount of therapeutic molecules in order to achieve a detectable effect in the

diseased tissue, which will only receive a small fraction of the initial dose [18]. Thus, local, sustained delivery of protease inhibitors could reduce disease progression without deleterious side effects and with reduced amounts of therapeutic molecules to reduce cost-barriers to treatment.

To achieve local, sustained delivery of protease inhibitors, many laboratories have enlisted the use of polymer-based microparticles, such as those formed from poly(ethylene glycol) diacrylate, PEGDA [19–22]. Microparticles can be synthesized a variety of ways, but fabrication by way of microfluidic device has distinct advantages. Benefits of using a microfluidic device include fabrication of uniformly sized microparticles, which eliminates the need for filtering microparticles that are too small or too large, which is common in other types of synthesis. The ability to keep all fabricated microparticles thusly reduces waste of polymer materials and allows for the incorporation of expensive ligands or crosslinkers. Additionally, with complete control over the microfluidic device size and phase speeds, we were able to adjust the size of our microparticles for future studies.

Development and characterization of our novel microfluidic device allowed us to select a desirable set of parameters to investigate other applications. First, we were able to confirm that therapeutic molecules could be loaded into our uniformly sized microparticles, which expanded the number of uses of our novel microfluidic device platform. Specifically, we loaded broad, small molecule inhibitor, E-64 into our microparticles and confirmed consistent sustained release over 14 days. With this evolution, we evaluated how varying several microparticle components would alter release of our small molecule *in vitro* over time. In addition to showing that E-64 release

could be tuned by altering the microparticle make up, this study established that biologically relevant amounts of E-64 could be released from our microparticles. Thus, we assessed *in vivo* release of E-64 indirectly via chemical modification with near infrared dye and near infrared imaging.

Finally, this thesis work resulted in the fabrication of a microparticle vehicle loaded with a broad, small molecule protease inhibitor injected into a rat model of rotator cuff tear. The purpose of this final study was to understand how this treatment altered active protease levels after injury and if degeneration of tendon tissue could be reduced or prevented. The research in this thesis contributes foundational knowledge to develop therapeutic strategies to halt joint tissue degeneration after rotator cuff tear and improve surgical outcomes following tendon re-attachment surgery.

1.2 Research Objectives

The **long-term goal** of this dissertation was to understand how proteases contribute to joint tissue degeneration (tendon, muscle, and cartilage) after rotator cuff tear. Understanding the spatial and temporal distribution of upregulated proteases after rotator cuff tear can best inform therapeutic treatments to prevent degeneration, which would result in improved surgical outcomes after rotator cuff tear re-attachment surgery. First, using a rat model of rotator cuff tear that has been shown to replicate degenerative damage seen in humans [23], we investigated active proteases in each joint tissue (tendon, muscle, and cartilage) over time. Second, we designed a novel microfluidic device to fabricate uniformly sized microparticles that can be loaded with protease inhibitors for subsequent use *in vivo*. Also, we reinvented a currently available

fluorogenic substrate assay for the detection of E-64 (a broad, small molecule cathepsin inhibitor), which was our desired therapeutic. This was important because previous therapeutic use of E-64 had been limited to systemic, soluble injections of known amounts because E-64 is unable to be quantified by other standard methods [24,25]. Lastly, we tested our E-64 loaded microparticles system on tendon tissue in our rat model of rotator cuff tear to elucidate the effect of sustained release of a broad cathepsin inhibitor on active proteases.

The **rationale** for this thesis project is that a comprehensive understanding of the spatial and temporal distribution of destructive proteases after rotator cuff tear injury and uniformly-sized inhibitor loaded microparticles for localized therapeutic treatment of proteases can together reduce joint tissue degeneration after rotator cuff tear and improve surgical outcomes of tendon re-attachment surgery. The overall **hypotheses** for this thesis project are that (1) there are spatial and temporal differences in active protease levels in joint tissues following rotator cuff tear and (2) localized treatment with protease inhibitor (E-64)-loaded microparticles into tendon tissue at the time of injury will result in a significant decrease in active protease levels (cathepsins and MMPs) relative to injury alone. These hypotheses were tested using the following three aims:

<u>Specific Aim 1:</u> Characterization Of Active Proteases (Cathepsins And MMPs) And Structural Damage Within Joint Tissues (Tendon, Muscle, And Cartilage) Following Rotator Cuff Tear.

In rotator cuff tear injuries, the supraspinatus tendon is the most commonly torn tendon. Subsequent to supraspinatus tendon tear, the supraspinatus muscle undergoes

muscle atrophy, fibrous infiltration, and develops fatty deposits throughout the muscle [3]. The torn tendon also causes a force imbalance in the shoulder and articular cartilage of the glenohumeral joint can undergo osteoarthritic changes including loss of glycosaminoglycan (GAG) content, increased surface roughness, and loss of cartilage tissue [4,5]. To replicate this damage in a rat model, previous work has shown that the injury requires transection of supraspinatus and infraspinatus tendons as well as denervation of the subscapular nerve, which directly enervates the supraspinatus muscle [23].

The ***objectives*** of this aim were to assess degenerative damage in joint tissues following rotator cuff tear in a rat animal model and characterize active proteases (both cathepsin and MMP families) spatially and temporally between the onset of injury and the manifestation of tissue degeneration. The ***hypothesis*** of this aim was that acute, full-thickness rotator cuff tear would result in significantly more active proteases (cathepsins and MMPs) early after tendon injury (1 week after transection), with delayed responses from cartilage and muscle (3-12 weeks after injury). Additionally, we hypothesized that protease upregulation timing would coincide with manifestation of visible tissue damage (as assessed by histology and/or μCT imaging) in each tissue. Following transection of the supraspinatus and infraspinatus tendons as well as denervation of the suprascapular nerve in the animal model, we assessed protease activity (cathepsins and MMPs) within the supraspinatus tendon, supraspinatus muscle, and humeral head cartilage via gelatin zymography at 1, 3, and 12 weeks post-injury. We assessed structural damage to tendon (cellular infiltration and changes in collagen alignment and orientation) via hematoxylin and eosin and second harmonic generation imaging 1 week after injury. Degeneration of

muscle was evaluated by quantifying fibrous infiltration via Masson's Trichrome staining 1 week after injury. Lastly, cartilage degeneration was assessed via micro-computed tomography at 1 and 12 weeks after injury.

<u>Specific Aim 2:</u> Development Of Novel Microfluidic Device For Uniform Microparticle Fabrication For Release Of Broad, Small Molecule Cathepsin Inhibitor, E-64.

Thus, the ***first objective*** of this aim was to develop a novel microfluidic device to fabricate uniformly sized poly(ethylene glycol) diacrylate (PEGDA) microparticles. To characterize the system, we varied several parameters of the system including continuous phase speed, discontinuous phase speed, and surfactant concentration in the continuous speed. This variation allowed us to better understand the range of microparticle sizes that could be achieved with our system. Previous microfluidic device work has asserted that particle size can be tuned by varying the speed of each phase independently. For example, a faster continuous or discontinuous phase would result more frequent particle pinch off, resulting in smaller microparticles [26]. Additionally, microfluidic devices that employ immiscible phases for particle formation use surfactants (such as span-80) to stabilize the shape of particles and prevent coalescence of particles [27]. It has been shown that particle size will vary with surfactant concentration below a certain threshold limit, which is dependent on the system and surfactant used [28]. The ***first hypothesis*** of this aim was that microparticle size would be inversely proportional to the speed of both the continuous and discontinuous phases. Additionally, we hypothesized that 40% span-80 would yield significantly smaller microparticles compared to 20% span-80 with any

given set parameters. We assessed microparticle size distribution using light microscopy and size analysis in ImageJ (NIH).

The ***second objective*** of this aim was to characterize release of E-64 *in vitro* over time using different fabrication parameters in our microfluidic device system. To determine the limits of E-64 release from our microparticles fabricated with our microfluidic device we varied: polymer weight percentage (10 wt% and 20 wt%), dithiothreitol (DTT) concentration (5 mM and 10 mM), and initial loading concentration (167 μg and 333 μg). Incorporation of DTT into the polymer network allows for hydrolytic degradation of PEGDA. The ***second hypothesis*** of this aim was that E-64 release over 14 days could be tuned based on the aforementioned parameters. Specifically, we hypothesized that larger polymer wt% would result in less E-64 release over time. Use of larger polymer wt% creates a smaller mesh size and can delay the diffusion of molecules out of the polymer network [29]. Second, we hypothesized that larger amounts of DTT would result in greater release of E-64 over a longer period of time due to faster degradation and increased spacing between polymer chains. Third, we hypothesized that greater initial loading of E-64 would result in a larger amounts of E-64 released over 14 days. Finally, we hypothesized that E-64 would achieve sustained released from our microparticles and remain bioactive over 14 days. E-64 bioactivity and release was assessed using a DQ Gelatin Fluorogenic Substrate Assay (Thermofisher).

<u>Specific Aim 3:</u> The Effect Of Sustained Release Of E-64 On Relative Amounts Of Active Proteases Found Within Tendon Following Full-Thickness Rotator Cuff Tear In A Rat Model.

In Aim 1 of this study, we found our rat model of rotator cuff tear showed significantly more active cathepsin L and MMP-2 in tendon 1 week following injury [30]. The ***objective*** of this aim is to understand how the proteolytic network responds to local cathepsin inhibition within the tendon 1 week after injury. The ***hypothesis*** of this aim is that E-64 loaded microparticle delivery to supraspinatus tendon will result in significantly less active cathepsin proteases after rotator cuff tear compared to injury only, soluble E-64 treatment, and unloaded microparticle treatment. Previous work has demonstrated that active cathepsin proteases can cleave and activate MMPs [31]. Thus, we hypothesize that detection of decreased levels of active cathepsin will correspond to significantly less active MMP proteases.

Our rat model of rotator cuff tear includes transection of the supraspinatus and infraspinatus tendons as well as denervation of the suprascapular nerve. At the time of surgical injury, treatments were directly injected into the supraspinatus tendon. We injected each treatment into the proximal third of the tendon and assessed active protease levels (cathepsins and MMPs) within that same region of the supraspinatus tendon using multiplex gelatin zymography 1 week after injury.

1.3 Significance and Scientific Contribution

Many treatment strategies have focused primarily on restoring the affected muscle due to its distinctive increasingly severe degeneration, which is considered the primary

reason for failed re-attachment surgeries [23]. However, this work showed that degeneration progressed throughout all three joint tissues (tendon, muscle, and cartilage) when rotator cuff tear was left untreated. Tendon exhibited significant protease upregulation at 1 and 3 weeks after injury, with the manifestation of degeneration after 1 week. Conversely, muscle exhibited significant protease upregulation at 1 and 3 weeks with the manifestation of degeneration at 3 weeks only [19]. Similarly, cartilage exhibited significant protease upregulation at 1 week, but degeneration was only detectable at the 12 week assessment. Overall, this work found that degeneration occurs in all three joint tissues following rotator cuff tear, therefore rotator cuff tear treatment strategies should include tendon and cartilage consideration in addition to muscle. Additionally, this work investigated active protease upregulation relative to the manifestation of degeneration in joint tissues after rotator cuff tear, which suggests that active protease upregulation, while brief, could have lasting effects on the health of joint tissue.

We found each tissue experienced a unique combination of active cathepsins and MMP proteases, which changed over time. Specifically, tendon showed upregulated cathepsin L at 1 week and upregulated MMP-2 at 1 and 3 weeks after injury, muscle demonstrated significantly more active cathepsin L at 1 and 3 weeks and significantly more MMP-2 at 3 weeks after injury, and cartilage presented with significantly more active cathepsin L and K 1 week after injury. Interestingly, we detected a pattern whereby cathepsin proteases tended to occur concurrently or preceded active MMP proteases after rotator cuff tear. A large portion of previous work has investigated MMP inhibition to halt or reduce tissue degeneration [32–34], but this work suggests that significant degenerative damage may have already occurred prior to the activation of MMPs by

activated cathepsin proteases. Thus, this work demonstrates a strong need to investigate cathepsin proteases are a potential upstream therapeutic target to prevent tissue degeneration.

The research outlined in this dissertation is significant because we investigated active proteases in joint tissues (tendon, muscle, and cartilage) after rotator cuff tear in a rat model with similar degenerative damage seen in humans over time [23]. Understanding the temporal and spatial distribution of active proteases within joint tissues would better inform ideal intervention times and therapeutic strategies for each afflicted tissue. Taken together, this could reduce joint tissue degeneration and yield better surgical outcomes following tendon re-attachment procedures.

In terms of technology, the work in this thesis provides laboratories and researchers with a new, simple microfluidic device platform that can synthesize uniformly sized microparticles in a variety of sizes. A device such as this has practical applications in a variety of fields including drug delivery and tissue engineering [19,20,35–37]. The ability to form microparticles that will incorporate materials loaded into the discontinuous phase allow the user to reduce material waste which may include polymers, crosslinkers, or proteins of interest with the confidence that it will be incorporated into a biomaterial carrier of a desired size. In addition, we found that our novel microfluidic device can incorporate therapeutic molecules into microparticles for sustained release, which expands potential uses of this new technology.

In addition to designing a novel microfluidic device, we also redesigned a currently available fluorogenic substrate assay for E-64 quantification in solution. E-64 is

the small molecule analog of the endogenous cysteine cathepsin inhibitor [38] and has been shown to irreversibly bind cathepsins L, S, and K [39,40]. Previously, therapeutic use of E-64 had been limited to systemic, soluble injections of known amounts because E-64 is unable to be quantified by other standard methods, which would be required to investigate E-64 release from a biomaterial carrier *in vitro* [24,25]. For example, antibodies to E-64 do not exist and therefore an ELISA cannot be used. E-64 does not contain a ring structure and therefore cannot be detected using an absorbance reading on a plate reader [41]. Furthermore, E-64 cannot be detected on Bicinchoninic Acid assay (BCA) or Pierce Coomassie assay, which are to commonly used protein quantification assays. While vendor websites (including Millipore-Sigma and Selleck Chem) have listed high-performance liquid chromatography (HPLC) as the chosen method used to purify E-64, there is limited information on how to replicate the protocol, the limit of detection of E-64, and if microparticle materials would interfere with E-64 detection and quantification. Thus, the reinvention of the currently available DQ gelatin fluorogenic substrate assay allows our laboratory and others to more easily quantify E-64 release from biomaterial carriers, which may increase its use for therapeutic applications.

For the purposes of this dissertation, we also developed a tendon injection protocol and demonstrated that therapeutic molecules loaded into microparticles remain at the site of injection significantly longer than soluble injection. Previous work that aimed to treat tendons with injection-based therapies, described various injection protocols including injection into the subacromial space, the supraspinatus muscle, or simply into the rotator cuff repair site [42–45]. However, in this work we demonstrated we can consistently inject our microparticles directly into the proximal third of the

supraspinatus tendon. Additionally, through the use of tagging E-64 with a near infrared dye, we demonstrated that E-64 loaded into microparticles persists in the rotator cuff area over 21 days. This suggests that our platform has the capacity to provide sustained treatment to a localized area.

This dissertation work is the first step in investigating protease contribution to joint tissue degeneration after rotator cuff tear. While our treatment with E-64 loaded microparticles did not yield reduced levels of active proteases, additional work is warranted to better determine the cellular source of active proteases and the localization of proteases (intra vs. extracellular) to improve the efficacy of our microparticle delivery treatment. This work demonstrates the complexity of the proteolytic network and demonstrates that the challenges in developing therapeutic strategies for diseases characterized by dysregulated proteases may not be straightforward. After further refinement of this animal model, such a system could be used to probe the role of protease inhibition in both tendon degeneration, as well as, more broadly, acute inflammation in musculoskeletal tissues.

The work outlined in this dissertation first identified specific protease targets within joint tissues over time. This information provided a baseline to develop a plan for more tailored treatment in our rat model of rotator cuff tear. Second, this thesis work provided two new technological advancements to subsequently be used to treat dysregulated proteases *in vivo*. Our novel microfluidic device allows us to fabricate suitably sized microparticles loaded with therapeutic molecules in a high throughput way. Additionally, we reinvented a currently available fluorogenic substrate assay that allows E-64 (whose uses had been previously limited by detection methods) to be investigated as

a potential therapeutic treatment. The culmination of this thesis work allowed us to test a localized protease-inhibitor based treatment to treat upregulated proteases in supraspinatus tendon in an established rat model of rotator cuff tear. The contribution of this body of work provides key first steps therapeutic strategy to improve the current gold standard of treatment following rotator cuff tear. The ability to locally inhibit proteases may provide clinical therapeutic treatment for diseases characterized by significant protease-mediated degeneration and also provide a platform to investigate the intricacies of the proteolytic network.

CHAPTER 2 BACKGROUND AND LITERATURE REVIEW

2.1 Glenohumeral Joint and Rotator Cuff

Three bones form the shoulder: the scapula, the clavicle, and the humerus [46]. The glenohumeral joint of the shoulder is a ball and socket joint, whereby the head of the humerus (humeral head) is the ball and the glenoid cavity of the scapula is the socket. The humeral head is considerably larger than the glenoid cavity and they share a limited interface, which provides the shoulder a very high level of mobility. Consequently, the glenohumeral joint is stabilized by a network of connective tissues including the rotator cuff. The rotator cuff is composed of four muscles [46]. All four muscles of the rotator cuff (supraspinatus, infraspinatus, teres minor, and subscapularis) are attached to the humeral head through their respective tendons, which fuse to form a continuous structure near the site of insertion [47].

2.1.1 Tendon Structure and Function

Tendons are a class of fibrous connective tissue that connects muscle to bone. Tendon tissue is predominately composed of collagen and tenocytes (fibroblast-like tendon cells) within a well-ordered extracellular matrix [48]. Tendon tissue is linear with hierarchical structure. Type I collagen is the smallest unit of tendon. Collagen is composed of three polypeptides that assemble into a triple helix. Triple helical collagen is assembled into fibrils. The fibril level of organization contains a high level of intermolecular cross-linking, which increases the overall tensile strength of the tendon tissue [49]. Collagen fibrils are assembled into collagen fibers in a crimped pattern, which allows for 1-3% elongation of tendon [50,51]. This protects the tendon from injury

following a sudden increase in mechanical loading. Tenocytes, the cells of the tendon, are located between collagen fibers and are responsible for maintaining the extracellular matrix. The extracellular matrix between collagen fibers contains proteoglycans such as aggrecan and decorin, which attract water in order to reduce friction and allow fibers to glide past one another under mechanical loading [52,53]. Collagen fibers are further assembled into fascicles surrounded by endotendon, a connective tissue that surrounds individual strands of tendon [52]. Tendon fascicles are subsequently bundled and surrounded by epitenon to form the tendon. The epitenon houses a network of blood vessels, lymphatic vessels, and neurons that maintains tenocytes [52]. The hierarchical arrangement of collagen within tendons allows extensive deformation under axial loading: wavy fibrils can be uncrimped, twisted triple helical collagen molecules can be straightened, and finally collagen can be uncoiled at the molecular level [47].

2.1.2 Muscle Structure and Function

The four muscles of the rotator cuff are skeletal muscles. Skeletal muscles are voluntary muscles that function to move the human skeletal system. The smallest structural unit of skeletal muscle is the muscle fiber, which is a single cylindrical muscle cell. Individual muscle fibers are bundled together to form a fascicle, which is surrounded by endomysium connective tissue [54]. Muscle fascicles are bundled together and surrounded by perimysium connective tissue to form the muscle surrounded by the epimysium [54]. Blood vessels and nervous tissue run the length of the muscle between fascicles, which ensure muscle tissue is vascularized and enervated [54].

The muscles of the rotator cuff include the supraspinatus, infraspinatus, teres minor, and subscapularis and are responsible for movement of the arms. The supraspinatus muscle originates from the supraspinous fossa in the scapula [47] and is responsible for overhead abduction of the arm. The infraspinatus and teres minor muscles originate from the infraspinatus fossa and fibrous septum [47]. The infraspinatus and teres minor muscles allow for external rotation of the arm [55,56] and together exert posterior force to keep the humeral head within the glenoid cavity [57]. The subscapularis muscle originates from the subscapular fossa [47] and provides an anterior force to balance the force of the infraspinatus and teres minor muscles and keep the humeral head in the glenoid cavity [57].

2.1.3 Cartilage Structure and Function

Cartilage is a specialized connective tissue found on the ends of bones to provide a smooth surface for movement of joints. In the shoulder, cartilage is located at the end of the humeral head and in the glenoid cavity. Cartilage is composed primarily of type II collagen and aggrecan proteoglycans to create a solid extra-cellular matrix [47]. The cells found in cartilage and responsible for its maintenance are called chondrocytes. Cartilage tissue contains four zones of varying composition, namely the superficial, middle, deep, and calcified zones. The superficial zone consists primarily of densely packed type II and type IX collagen oriented parallel to the articular surface [47,58]. A large population of chondrocytes care found in the superficial zone and normally present with a flat and elongated morphology [58]. The middle zone contains the highest percentage of proteoglycans and collagen fibers are randomly oriented [47,58]. Chondrocytes found in the middle zone have a spherical morphology and are found at a lower concentration

[58]. The cartilage deep zone contains large collagen fibers oriented perpendicular to the articular surface [47]. Chondrocytes in the deep zone are slightly elongated and oriented parallel to the collagen fibers (perpendicular to the articular surface) [58]. A thin line at the bottom of the deep zone is called the tidemark and marks the division of the calcified and non-calcified zones [58]. The calcified zone is transitional to the subchondral bone directly beneath the cartilage, which minimizes the stiffness gradient between cartilage and bone [59]. The collagen found in the deep zone originates in the calcified zone, which anchors cartilage to bone [58]. Chondrocytes in the calcified zone are scarce and are hypertrophic [58].

2.2 Rotator Cuff Tear and Treatment

2.2.1 Rotator Cuff Tear and Prevalence

Injury of the shoulder usually involves a partial or full-thickness tear of one or more rotator cuff tendons [60]. It is estimated that 34% of the population has a partial or full-thickness tendon tear in at least one shoulder [1]. Additionally, it has been documented that risk of rotator cuff tear increases with age, whereby 50% of patients over 60 years of age present with a partial or full-thickness tendon tear in at least one shoulder [1]. Rotator cuff tendon tear can occur by acute trauma to the shoulder such as a fall or chronic overuse of the shoulder [61]. In the case of chronic overuse, small molecular changes can occur in tendon over time and result in a partial thickness tear. If left untreated, the partial tear can propagate in size and cause a full-thickness tear of the tendon and result in degeneration of neighboring muscle, cartilage, and bone [47,61].

2.2.2 Tendon Degeneration In the Context of Rotator Cuff Tear

Tendon is a metabolically active tissue that has the capacity to adapt to changes in mechanical loading. Specifically, tenocytes have been shown to upregulate collagen expression and synthesis in response to strain [62]. Conversely, an increase in catabolic protease expression and collagen turnover has been seen following exercise [63]. Thus, a balance exists between anabolic and catabolic factors to maintain tendon health. In the case of chronic tendon overuse, there is a net negative balance whereby more collagen is being lost than replaced. Thus, chronic overuse of tendon results in the development and accumulation of microinjuries creating a mechanically inferior connective tissue. Human patients presenting with shoulder pain in the absence of a tendon tear are subsequently diagnosed with tendinosis or tendinopathy. Characteristic changes of tendon experiencing chronic overuse include cell rounding of tenocytes, reduced tenocyte numbers, increased apoptosis, increased proteoglycan content, and disorganization of collagen [64]. Additionally, tear of any rotator cuff tendon causes additional strain to neighboring intact tendons due to the disrupted force balance, which results in increased tendon stiffness [65].

An acute tear in one or more of the rotator cuff tendons causes an inflammatory response. During the inflammatory response, vasodilation increases blood flow and vascular permeability allows a greater influx of inflammatory cells to enter the site of injury [66]. The recruited inflammatory cells, including neutrophils, produce cytokines and growth factors that elicit cellular recruitment of macrophages [66]. Neutrophils and macrophages at the site of injury secrete proteases for the purpose of clearing debris, wound healing, and tissue remodeling [67–69]. Unfortunately, the human rotator cuff

tendons do not have a high capacity for self-renewal and healing [66]. However, following repair the recruited inflammatory cells can influence resident tenocytes to proliferate and produce a disorganized collagen scar at the repair site [66]. Nevertheless, without surgical intervention, rotator cuff tendons undergo extensive degeneration including fiber disorganization and decreased collagen content [2].

2.2.3 Muscle Degeneration after Rotator Cuff Tear

Following rotator cuff tendon tear, the accompanying muscle will similarly experience degeneration after injury. Specifically, the muscle will atrophy [70] and develop fatty deposits within the muscle belly, [3] which prevent normal muscle contraction [47]. Human patients presenting with shoulder pain can be imaged with computed tomography **(**CT) or magnetic resonance imaging (MRI) to test for muscle atrophy and fatty infiltration, two hallmarks of rotator cuff tear. Additionally, several groups have found fibrous scar tissue development within muscles after rotator cuff tear in several animal models including sheep, rat, and rabbit [23,71,72]. The addition of fibrous infiltration as a hallmark of muscle degeneration after rotator cuff tear preceded atrophy and fatty infiltration because it cannot be differentiated from muscle tissue on CT or MRI scans in humans.

2.2.4 Cartilage/Bone Degeneration after Rotator Cuff Tear

Articular cartilage in the glenohumeral joint is located on the humeral head and the glenoid cavity. As mentioned previously, the humeral head and glenoid cavity are not perfectly matched in size. This size difference is overcome by creating a force balance around the humeral head with the tendons and muscles of the rotator cuff. Together, this

force balance keeps the humeral head appropriately aligned with the glenoid cavity. Thus, even a single tendon tear causes a disruption in the force balance and an increased risk of articular cartilage degeneration, eventually resulting in the development of osteoarthritis of the shoulder [5]. Specifically, after a rotator cuff tendon tear the articular cartilage will demonstrate cartilage tissue loss, increased surface roughness, softening of subchondral bone, and a decrease in proteoglycan content [4,47,73].

Under normal conditions, the humeral head bone experiences mechanical stress from rotator cuff muscles transmitting forces through tendon. However, following a rotator cuff tear, the humeral head will no longer experience mechanical loading at the tendon insertion site and eventually cause a decrease in bone density, which is characteristic of subchondral bone osteoporosis [54]. Furthermore, tear of the supraspinatus tendon causes upward displacement of the humeral head, which can cause erosion of the acromion [5].

2.2.5 Current Treatment of Rotator Cuff Tears

Current guidelines by American Academy of Orthopaedic Surgeons does not offer recommendations on how to decide which patients would benefit from invasive vs. non-invasive rotator cuff tear treatment. The current gold standard of treatment to treat rotator cuff tear include regimented nonsteroidal anti-inflammatory drugs (NSAIDs), physical therapy, and potentially surgical reattachment of the torn tendon [74]. Surgical re-attachment includes anchoring the torn tendon onto the humeral head bone via a bone tunnel. One group reviewed national hospital and ambulatory surgery databases and found that in a single decade the number of rotator cuff tear surgeries increased by 141%

[75]. Interestingly, they also found that there was a significant shift from open rotator cuff repair surgery to arthroscopic rotator cuff repair surgery [75]. Nevertheless, surgical reattachment surgery has a documented re-tear rate of 30-94% [6,7]. Instance of tendon re-tear following surgical reattachment has been found to correlate to muscle degeneration (muscle atrophy and fatty infiltration) at the time of surgery, tendon tear size (partial vs. full-thickness), and patient age [76–78]. The most common method of tendon reattachment failure is the tendon pulling away from the sutures in the humeral head [79].

The purpose of surgically reattaching a torn rotator cuff tendon is to restore the force-balance of the glenohumeral joint and manage patient pain. Interestingly, treatment does not always involve reattachment of every torn tendon. If a patient presents with tears in both the supraspinatus and infraspinatus tendons, repair of the infraspinatus alone would restore the force balance [57]. Additionally, injury to the rotator cuff tendons can cause damage to adjacent tendons, including the long head of the biceps tendon (LHBT). Tenodesis or tenotomy of the LHBT has shown a reduction in pain with minimal effect on the force balance of the glenohumeral joint [80]. In a rat model of multiple rotator cuff tears, transection of the LHBT improved shoulder function and reduced joint damage [81].

Ultimately, the primary function of surgical reattachment of a torn rotator cuff tendon is to restore the force balance of the shoulder. However, even in the case of a successful reattachment (no re-tear), the procedure does not treat degeneration that has already occurred in the tendon, its respective muscle, or articular cartilage. Current surgical reattachment procedures do not replicate the tendon-to-bone insertion site and

the reattached tendon does not regain normal structure after being anchored to the humeral head [61]. Similarly, patients presenting with low to moderate muscle atrophy at the time of reattachment surgery have shown maintenance of degeneration (no improvement) over time after surgical repair [82]. However, patients with severe muscle degeneration at the time of reattachment will continue to atrophy and develop advancing fatty infiltration [82]. Additionally, cartilage loss and subchondral bone softening that occurred prior to surgical reattachment will not be reversed [5].

Most recently, there has been a deliberate push to advocate for early surgical repair of rotator cuff tendons [83]. Non-invasive methods have been shown to improve patient-reported outcomes (including strength and reduced pain) and overall improvement in glenohumeral joint kinematics [83], but the improvements can be temporary. Instead, small asymptomatic tears have been shown to progress in size and consequently advance to full-thickness tears with concomitant pain and decreased shoulder function [84,85]. While early intervention could prove beneficial, many patients are either asymptomatic or ignore increasing pain and therefore do not seek medical attention until after considerable degeneration has occurred, which limits treatment options [83].

2.2.6 Animal Models of Rotator Cuff Injury

Animal models provide a platform for researchers to study the etiology of tendinopathy and joint degeneration after rotator cuff tear. The use of animal models allows us to analyze tissue at all stages of injury and allow the use of terminal methods, which cannot be performed in humans. Several animal models have been used to

investigate rotator cuff tear injuries including rat [23,86,87], mice [88,89], sheep [71,90,91], and rabbit [72,92,93]. However, the Soslowsky group evaluated 33 different animals on a 34 point checklist to determine their appropriateness to serve as an animal model of rotator cuff injuries and found that rats were the only animal that satisfied each criteria [94]. Despite rats being quadrupeds, they share similar shoulder anatomy to humans. Specifically, the supraspinatus tendon passes under the acromial arch and normal forward locomotion causes the rat supraspinatus tendon to repetitively pass under the acromion, which can replicate overuse injuries seen in humans [94].

Several different animal models exist to replicate different aspects of rotator cuff injury. An animal model that undergoes surgical transection of one or more rotator cuff tendons can be used to study acute rotator cuff tendon tear caused by trauma which stimulates an inflammatory response or be used as a test bed to treat degenerative damage seen in humans [30]. An animal model that performs sustained downhill running would replicate chronic tendon injuries caused by repetitive overhead motion (overuse injury) [14,15]. Several studies have performed a combination of overuse and acute injuries in their animal models to mimic patients such as athletes or laborers that are likely to resume activities soon after surgical treatment [65,95]. Furthermore, to better replicate the human condition, several studies have performed surgical reattachment of torn rotator cuff tendons on animal models both at the time of injury and several weeks afterward [71,96,97].

Most often, laboratories develop animal models of acute rotator cuff tendon tear in order to recreate degenerative damage seen in humans. Human patients that have suffered a rotator cuff tear often seek treatment after significant degeneration has already

occurred including atrophy and fatty infiltration of rotator cuff muscles [83]. Thus, several groups have sought to mimic this degenerative damage in rodent animal models in order to test therapeutic interventions [4,23,87–89,98,99]. Several groups have developed personalized acute rotator cuff tear models for their purposes. The Soslowsky laboratory has tested several variations of rotator cuff tear including: transection the supraspinatus tendon alone [100], transecting both the supraspinatus and infraspinatus tendons [87], and transecting the supraspinatus and subscapularis tendons [101]. The Feeley laboratory has developed rotator cuff tear animal models in both rats [23] and mice [88]. Additionally, they have tested various injuries including tear of both the supraspinatus and infraspinatus tendons [4,88,89,98] and a much more severe injury that involved transection of the supraspinatus, infraspinatus, and teres minor tendons [23].

As can be expected different injuries models (one vs. two vs. three tendon tears) will cause different levels of degeneration. The Feeley laboratory demonstrated that massive rotator cuff tear (transection of the supraspinatus, infraspinatus, and teres minor tendons) in rats resulted in significant muscle atrophy of the supraspinatus and infraspinatus muscles 2 weeks after injury [23]. Additionally, they demonstrated that massive rotator cuff tear resulted in significant fibrous infiltration of the supraspinatus and infraspinatus muscles, while only the infraspinatus muscle developed significant fatty infiltration 6 weeks after injury [23]. Similarly, the Feeley laboratory transected both the supraspinatus and infraspinatus tendons in mice and found significant atrophy in both muscles 12 weeks after injury [88]. However, they found that neither muscle developed significant fatty infiltration 12 weeks after injury [88]. Additionally, the Feeley laboratory found that transection of the supraspinatus and infraspinatus tendons caused

significant degeneration of humeral head cartilage and glenoid cartilage 12 weeks after injury [4].

The supraspinatus tendon is the most commonly ruptured tendon of the rotator cuff in humans [102] and often presents with significant atrophy and fatty infiltration [103]. Therefore, the aforementioned animal models of rotator cuff tear did not sufficiently mimic degeneration seen in humans with tendon transection alone. Thus, the Feeley laboratory sought to increase muscle degeneration in their animal models of rotator cuff tear by the addition of denervation of the suprascapular nerve, which directly enervates the supraspinatus muscle. They found that the combination injury of massive rotator cuff tear (transection of the supraspinatus, infraspinatus, and teres minor tendons) and denervation did not cause additional atrophy, fibrous infiltration, or fatty infiltration to either the supraspinatus or infraspinatus muscles in rats [23]. However, in a mouse model that underwent transection of supraspinatus and infraspinatus tendons and denervation of the suprascapular nerve, they found the combination injury caused significantly more muscle atrophy of the supraspinatus and infraspinatus muscles relative to either injury alone [88]. Similarly, they found the combination injury caused significantly more fibrous infiltration compared to either injury alone [88]. Interestingly, they found that denervation alone caused significantly more fatty infiltration in both the supraspinatus and infraspinatus muscles compared to tendon transection alone [88]. The combination injury did not cause significantly more fatty infiltration in the supraspinatus muscle compared to denervation alone, but the injury was additive in the infraspinatus muscle [88]. Furthermore, they found that transection of the supraspinatus and

infraspinatus tendons alone caused similar damage compared to denervation alone in humeral head and glenoid cartilage [4].

2.3 Proteolytic Degradation

A possible cause for the extensive joint tissue degeneration observed following rotator cuff tear is the prolonged activation of proteases. Proteases are specialized enzymes whose primary function is to degrade proteins. Of particular interest are cysteine cathepsins and matrix metalloproteinases (MMPs), which play a role in many facets of homeostasis within the human body including extracellular matrix remodeling, bone resorption, and intracellular protein turnover [9–11]. However, these two families of proteases have also been observed to be upregulated in a variety of musculoskeletal diseases, including atrophy of the tibialis anterior muscle [12], osteoarthritis of the knee [13], and tendinopathy [14,15].

2.3.1 Cysteine Cathepsins

There are 11 members of the cysteine cathepsin family of proteases [11]. Cathepsins proteases are responsible for a variety of homeostatic functions including extracellular matrix remodeling, bone resorption, and intracellular protein turnover [11]. The 3D structure of cysteine cathepsins is generally conserved and consists of two domains. The left and right domains form an inverted cone shape with the catalytic active site located at the top. The left domain contributes an active cysteine reside to the catalytic active site, while the right domain provides an active histidine residue. Together, these two catalytic residues form the thiolate-imidazolium ion pair, which is essential for the proteolytic activity of cathepsins [11].

The cathepsin family of proteases has been observed in a variety of musculoskeletal disease states. Not surprisingly, the cathepsin family of proteases includes cathepsin K and cathepsin V, which are considered to be the most potent collagenase [104] and elastase [105] respectively. Cathepsin K is highly expressed in osteoclasts, but dysregulation has implicated it in the development of osteoporosis and osteoarthritis of the knee [10,16]. Additionally, upregulated levels of cathepsin K have been found in calcified human tendons and a rabbit model of flexor tendon injury [106,107]. Cathepsin L has been shown to have the capacity to cleave multiple extracellular matrix proteins including type I collagen, type IV collagen, type XVIII collagen, elastin, fibronectin, and laminin [108,109]. Additionally, cathepsin L has been shown to be upregulated in instances of muscle atrophy in both rats and mice [104,110]. Cathepsin S is a potent elastase and has been shown to be expressed by endothelial cells and macrophages [109]. Additionally, active macrophages have been shown to express cathepsins L, S, and V [105] and cathepsin B is required for TNF-α secretion, which is a mediator of the inflammatory response [111].

Due to the highly destructive nature of cathepsin proteases, they are tightly regulated by various methods including required cleavage for activation, pH sensitivity, and endogenous inhibitors. Cathepsins are synthesized as inactive proenzymes, which require cleavage of the N-terminus for activation. Cathepsins can be activated by other proteases or autocatalytically under acidic pH conditions [11,112]. Most cathepsins are lysosomes proteases and are optimally active at acidic pH. However, cathepsin L has been shown to cleave multiple extracellular matrix proteins at neutral pH, while cathepsin S, is also active at neutral and even mildly alkaline pH [11,109]. Thus, cellular

necrosis and subsequent exposure to active cathepsins is mitigated by cathepsin pH sensitivity. Lastly, cathepsins are regulated by a large family of inhibiters, including cystatins, thyropins, and serpins [11]. Stefins are considered to be intracellular cathepsin inhibitors, while cystatins and thyropins inhibit extracellular cathepsins. Cathepsin inhibitors tightly bind the active site of cathepsin proteases in a reversable way, which prevents substrate binding [11].

2.3.2 Cystatin C and E-64

The cystatin family of inhibitors are responsible for inhibiting lysosomal cysteine proteases, including the cathepsin family of proteases. Cystatin C is the most prominent inhibitor of the cystatin family and is produced by most nucleated cells [109]. Cystatin C binds cathepsins in a tight, yet reversible fashion [113]. Inflammation can influence cystatin C secretion depending on the cell type. Specifically, it has been shown that cystatin C production decreases in mouse peritoneal macrophages following treatment with pro-inflammatory molecules [114], while human gingival fibroblasts increased the secretion of cystatin C following treatment with pro-inflammatory cytokines [115].

In addition to cystatin C, trans-Epoxysuccinyl-L-leucylamido(4-guanidino)butane, more commonly known as E-64 is also an inhibitor of the cysteine cathepsin family of proteases. E-64 is the isolated active site of cystatin C, and therefore considered to be the small molecule analog of cystatin C [38]. Thus, E-64 is a cell impermeable, small molecule, broad cathepsin inhibitor [39]. E-64 has been shown to have the capacity to irreversibly bind cathepsins L, S, and K [39,40]. In addition to the

therapeutic potential of E-64, analogs of E-64 have been developed to uncover the crystal structure of many cathepsin proteases [11].

Since the discovery of E-64 in 1977, there have been high hopes for its use to treat diseases characterized by upregulated proteases that result in significant tissue degeneration, such as cathepsin K mediated osteoporosis. A study performed in mice suffering from sickle cell anemia found that daily E-64 injections improved trabecular bone density and mechanical properties of femurs compared to mice with untreated sickle cell anemia [25]. However, human clinical trials that have used cathepsin proteases inhibitors have all been abandoned due to off-target effects [16]. More recently, several groups have aimed to create E-64 analogs with increased specificity to inhibit a specific cathepsin subtype as opposed to all cysteine cathepsin proteases [16]. However, off-target effects could be mitigated and development of a more specific cathepsin inhibitor would not be required if E-64 treatment could be localized to the site of disease or injury with a biomaterial carrier. However, the use of E-64 with a biomaterial carrier has been challenging due to the inability to detect it in solution to quantify release *in vitro*. E-64 is a small molecule and thusly does not have a readily available ELISA kit and does not have a ring structure that can be detectable with color changes or fluorescent light excitation/emission. Thus, the development of an assay to detect and quantify E-64 would increase the usefulness of E-64 as a therapeutic treatment for diseases characterized by upregulated cathepsin proteases.

2.3.3 Matrix Metalloproteinases

Matrix metalloproteinases (MMPs) are a family of 23 zinc-dependent endopeptidases that play a role in a variety of biological functions including cell proliferation, cell migration, tissue remodeling, wound healing, and angiogenesis [116]. MMPs have similar overall 3D structure, usually consisting of a propeptide region, a zinc-containing catalytic domain, a linker peptide, and a hemopexin domain [117,118]. MMPs can be found as secreted proteins or membrane-bound proteins and are optimally active a physiological pH [119].

The MMP family of proteases can be categorized by their substrates. MMP -1, -8, and -13 are collagenases and have the ability to cleave triple helical collagen at a single location, which generates characteristic ¾ and ¼ collagen fragments [104,118]. MMP-3 and -10 are stromelysins which are secreted into the extracellular space and play a role in immunity and would healing [116,118]. Additionally, stromelysins are responsible for activating proMMP collagenases and proMMP-9 [118]. MMP-7 and -26 are matrilysins and can degrade type IV collagen, laminin, and entactin [118]. Additionally, MMP-26 has been shown to cleave and activate proMMP-9 [118]. The gelatinases of the MMP family are MMP-2 and -9 and can degrade a broad spectrum of extracellular matrix proteins including type I, IV, V, VII, X, IX collagen, elastin, fibronectin, aggrecan, vitronectin, and laminin [120]. MMPs that cannot be classified into the aforementioned subgroups are labeled as “other archetypal MMPs” and include MMP-12, -19, 20, and -27. MMP-12 is the most potent elastase of the MMP family but can also cleave other extracellular matrix proteins including aggrecan, fibronectin, laminin, and type IV

collagen [118,120]. MMP-19 is characteristically destructive of basement membrane proteins including type IV collagen, gelatin, and aggrecan [121].

Collectively, the MMP family of proteases is capable of degrading all extracellular matrix components [118]. Thus, MMPs have been implicated in several musculoskeletal diseases. Specifically, MMP-1 activity has been shown to be significantly greater in human supraspinatus tendon following rupture [122] and MMP-1 and -3 have been shown to be upregulated within synovial fluid following rotator cuff tendon tear in humans [123]. Additionally, MMP-2, -9, and -13 have been shown to be more active in osteoarthritic cartilage compared to healthy cartilage in both humans and rats [124,125], while increases in MMP-2 and -9 activity positively correlated with the occurrence of muscle atrophy in rats [110,126]. MMP-19 has been detected in the inflamed synovium of patients suffering with rheumatoid arthritis [127]. MMP-12 is highly expressed in macrophages [128] but is also secreted by hypertrophic chondrocytes and osteoclasts [129].

Expression and translation of MMPs is maintained at low basal levels, but can readily be increased in response to stimuli including inflammatory cytokines, growth factors, cellular interactions, or extracellular matrix protein binding [130]. In the absence of regulation, the destructive nature of MMPs would completely degrade any extracellular matrix protein. MMP are primarily regulated at the transcriptional level [118], but the presence of endogenous inhibitors also provide a level of MMP regulation. The family of endogenous MMP inhibitors is called the Tissue Inhibitor of Metalloproteinases (TIMPs). Four TIMPs have been identified that inhibit MMPs with varying affinity [9]. TIMP-3 has the broadest inhibition spectrum and unlike the other

three TIMPs is found tightly bound to extracellular matrix proteins [9]. TIMP-2, TIMP-3, and TIMP-4 have been found to bind and inhibit MMP-2, while TIMP-1 and TIMP-3 have been shown to bind and inhibit MMP-9 [9].

2.3.4 Complexity of Proteolytic Network

The proteolytic network consists of all families of proteases and their naturally occurring inhibitors. The purpose of this vastly complex network is to maintain an appropriate ratio of proteases and inhibitors to achieve homeostasis within the body. For example, in the instance of wound healing, there is an increase in protease levels relative to their inhibitors in order to breakdown and clear any injured or diseased tissue and allow for the movement and replacement of healthy cells and tissue. However, in a disease state or chronic injury, such as rheumatoid arthritis, the ratio of inhibitor to protease becomes unstable and the amount of inhibitor is insufficient to prevent vast digestion of collagen resulting in irreplaceable degeneration of cartilage tissue [131].

Proteolytic network complexity is further heightened due to interactions of proteases within the same family and with other protease families. Specifically, it has been shown that cathepsin S in the presence of substrate and cathepsin K would preferentially cleave and degrade cathepsin K [132]. Similarly, it has been shown that cathepsin K and cathepsin cannibalize one another in the presence of tendon ECM [133]. Additionally, degradation of type I collagen and tendon ECM was enhanced following sequential introduction of cathepsin K followed by cathepsin L relative to each cathepsin protease alone, which suggests cooperation between cathepsin proteases [133]. Lastly, it

has been documented that cathepsin proteases have the capacity to cleave and activate MMPs [31].

While type I collagen is a substrate for multiple proteases, they do not all act on collagen equally. Cathepsins L, B, and S has been shown to have the ability to cleave collagen I within the telopeptide region, which is involved in intra- and intermolecular bonds between collagen units and generates type I collagen monomers [104]. Conversely, cathepsin K has the ability to cleave type I collagen in its native triple helix at multiple locations, which generates collagen fragments of various sizes [104]. Interestingly, MMP-1, -2, -8, and -13 have the ability to cleave type I collagen in its native triple helix but at a single site, which generates characteristic ¼ and ¾ fragments [104].

Investigation of protease inhibitors for the therapeutic purpose of treatment degenerative diseases characterized by prolonged upregulated proteases has further highlighted the complexity of the proteolytic network. It was observed in MDA-MB-231 cells (epithelial, human breast cancer cell line) that in the presence of broad cathepsin inhibitors E-64 and cystatin C, a decrease in the amount of active cathepsin L was seen, but paradoxically an increase in the amount of active cathepsin S was detected [38]. However, MCF-7 (breast cancer cell line) and MCF10A cells (human breast epithelial cell line) did not demonstrate increased cathepsin S levels in the presence and absence of E-64 treatment [38]. Additionally, THP-1 cells (human monocyte cell line) treated with E-64 caused a significant increase in active cathepsin S and V but a decrease in active cathepsin L [38]. Furthermore, it has been shown that bolus treatment of cystatin C can cause cellular endocytosis, which subsequently traffics cystatin C to the lysosome where it is less potent due to the acidic environment [38] and not fulfilling its intended

purpose. Together, this demonstrates that broad spectrum inhibitors can cause unexpected upregulation of cathepsin proteases, which could depend on the cell type and the location of the protease (intracellular vs. extracellular). Thus, perturbing the proteolytic network is vital to both seeking therapeutic treatments for a variety of diseases as well as gain fundamental knowledge of the vast and complex network of proteases and inhibitors that play a vital role in many basic homeostatic functions.

2.4 Biomaterial Delivery Vehicles

The implication that proteases are a potential cause for tissue degeneration in musculoskeletal diseases makes protease inhibitors an appealing potential treatment. Several protease inhibitors have been tested in human clinical trials to treat dysregulated cathepsins and MMPs, but all have been abandoned due to off-target effects [16,17]. These clinical trials have tested the safety and efficacy of protease inhibitors using systemic delivery, meaning both healthy and diseased tissues are equally exposed to the therapeutic treatment. As mentioned previously, proteases play a variety of roles in the human body and thus are not localized to any one area of the body. Consequently, regulated proteases in healthy tissue may be inhibited and prevented from performing their normal functions, causing negative side effects including headache, gastrointestinal disturbance, lung fibrosis, and skin lesions [16]. Moreover, systemic delivery requires a much larger amount of therapeutic molecules in order to achieve a detectable effect in the diseased tissue, which will only receive a small fraction of the initial dose [18]. Thus, local, sustained delivery of protease inhibitors could reduce disease progression without deleterious side effects and with reduced amounts of therapeutic molecules to reduce cost-barriers to treatment.

2.4.1 Microparticles for Drug Delivery

Microparticles are a frequently used biomaterial vehicle for therapeutic drug or protein delivery [134]. Compared to larger biomaterial vehicles (such as bulk hydrogels), microparticles have several important advantages. First, microparticles are injectable, which is important for clinical applications. Second, they provide a high surface area to volume ratio, which permits greater release of loaded drugs or proteins [134]. While hydrogels can be made to be injectable, it would require exposure to free radical initiators and could negatively affect both the patient and the delivered therapeutic [135–137]. Lastly, microparticle fabrication is highly customizable. Microparticles can be made from a variety of synthetic or natural materials and include specialized crosslinkers [138].

Additionally, microparticles can be directly injected into the diseased or injured tissue of choice including tendon, muscle, or the intra-articular space of cartilage, which would localize treatment to the desired area. Compared to systemic delivery, there are several advantages of using a microparticle vehicle to deliver therapeutics drugs or proteins. Systemic delivery is a bolus dose of therapeutic drug, whereas microparticles have the capacity to achieve sustained delivery over a longer period of time [134]. Sustained delivery is advantageous because fewer doses would be required, which could improve patient compliance. Sustained, localized release of therapeutic drugs is less likely to cause off-target effects, which has been observed in patients treated with cathepsin inhibitors [16]. Moreover, systemic delivery requires a much larger amount of therapeutic molecules in order to achieve a detectable effect in the diseased tissue, which will only receive a small fraction of the initial dose [18]. Decreasing the required amount to achieve a therapeutic dose would also reduce cost barriers to treatment.

2.4.2 Poly(ethylene-glycol)-Based Microparticles

Poly(ethylene-glycol) (PEG) is an attractive polymer that is commonly used in biomaterial applications because it is hydrophilic, does not adsorb many proteins *in vivo*, and is easily modified [139]. PEG can be chemically modified for a variety of purposes including for the purposes of chemical crosslinking, the addition of peptide binding sequences, and to enhance degradation. PEG can be functionalized with acrylate, thiol, or maleimide groups to allow for chemical crosslinking to itself, which is required for microparticle fabrication [21]. Additionally, peptide sequences can be chemically bound to PEG to allow for cellular attachment. PEG has been previously functionalized with two integrin binding peptides. Specifically, the RGD tripeptide, which is a common cellular recognition sequence found on many extracellular matrix [21] proteins and the GFOGER hexapeptide, which is the cellular recognition sequence found on triple helical collagen [140].

Poly(ethylene-glycol)-diacrylate (PEGDA) is a hydrolytically degradable polymer due to the presence of an ester bond on the backbone (as can be seen in Figure 2.1 below) [141]. However, the time scale for degradation is several months, which is significantly longer than needed for many applications for acute treatment [141]. Thus, many groups have incorporated crosslinkers to increase the rate of PEGDA degradation. Our group has previously incorporated dithiothreitol (DTT) into our PEGDA network to increase the susceptibility of the ester bond [142]. Previous work has demonstrated that microparticle degradation rate is proportional to DTT levels incorporated into the microparticle network [143]. Furthermore, release of loaded therapeutics could be modulated by the hydrolytic degradation rate. For example, slower degradation could result in sustained

release over a longer period of time [134]. Another method that has been used to increase hydrolytic degradation of PEG is the addition of poly(lactic acid) (PLA) [29]. It has been shown that the degradation rate of PEG-PLA hydrogels can be tuned by adjusting the polymer content of the hydrogel and the length of the hydrolytically degradable PLA segments [29].

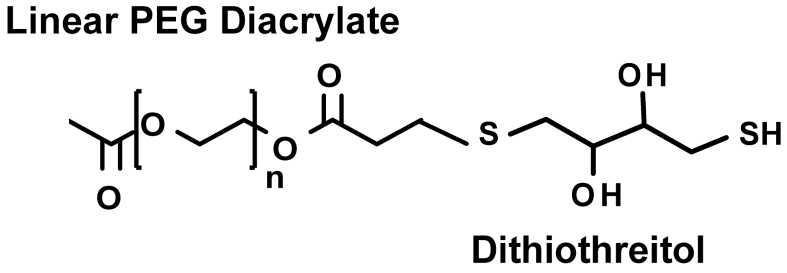

Figure 2.1: Chemical structure of poly(ethylene-glycol)-diacrylate (PEGDA) and Dithiothreitol (DTT) bound by Michael Type addition. *Adapted from Tellier LE, Treviño EA, Brimeyer AL, Reece DS, Willett NJ, Guldberg RE, Temenoff JS. Intra-articular TSG-6 delivery from heparin-based microparticles reduces cartilage damage in a rat model of osteoarthritis. Biomaterials science. 2018;6(5):1159-67.*

However, degradation of PEG-based materials is not limited to hydrolytic degradation, they can also be modified to undergo degradation by specific enzymes such as matrix metalloproteinases (MMPs) for on demand release of cargo. One study modified PEGDA with an MMP-1 susceptible peptide so that degradation was dictated by macrophage infiltration [144]. Protease-sensitive crosslinkers have also been used to provide enhanced control of biomaterial degradation to match cellular infiltration or release therapeutic molecules in response to active protease cleavage [22,145]. Additionally, other groups have incorporated enzyme-labile caprolactone units into PEG-based hydrogels [146,147]. This system allows the user to dictate the rate of degradation by controlling the delivery of exogenous lipase [146,147]. Overall, PEG-based materials

are highly customizable and can be broadly applied to a variety of purposes and therapies.

Numerous hydrolytically degradable PEG-based hydrogel systems have been developed for controlled delivery of biomolecules. Fluvastatin, which has been shown to stimulate BMP-2 production in osteoprogenitors, was released from PEG-monomethacrylate (PEGMMA) functionalized with lactic acid to allow for hydrolytic degradation [148]. In this work, lactic acid of varying repeat units was incorporated into the network, to better understand how Fluvastatin release could be tuned by degradation rate [148]. All groups released 100% of loaded Fluvastatin, but the rate was dependent on the speed of degradation [148]. Specifically, the fastest degrading hydrogel (greatest number of lactic acid repeat units) achieved 100% release by day 7, while the medium degrading gel achieved 100% release by day 13 and the slowest degrading gel (lowest number of lactic acid repeat units) achieved 100% release by Day 18 [148]. Another group used eight-arm PEG-acrylate and DTT crosslinkers to investigate how degradation rate affected the release of a covalently bound fluoroscopic probe [149]. The fluoroscopic probe was covalently bound to the PEG-acrylate network via the reactive thiol group on the fluoroscopic probe and the acrylate group on PEG [149]. Thus, release of the fluoroscopic probe was dependent on hydrolytic degradation of the resulting ester bond. They found faster degradation resulted in faster achievement of 100% fluoroscopic probe release by day 8, while relatively slower degradation resulted in 100% release of the fluoroscopic probe after 10 days [149].

Furthermore, PEG-based hydrogel systems with protease-sensitive crosslinkers have also been developed for controlled delivery of biomolecules. One group fabricated

PEGDA microparticles crosslinked with an MMP-1 sensitive peptide and tested the release of an encapsulated small molecule (dexamethasone) and model protein (biotinylated horseradish peroxidase) [144]. They found increasing rates of release in the presence of increasing amounts of collagenase [144]. Specifically, 100% of loaded dexamethasone was released after 15 hours in the presence of 3 μg/mL of collagenase, while the same amount of loaded dexamethasone was not released until 25 hours of incubation in the presence of 0.6 μg/mL [144]. Similarly, 100% of loaded biotinylated horseradish peroxidase was released after 25 hours of incubation in the presence of 3 μg/mL of collagenase, while incubation without collagenase only resulted in 50% release of loaded biotinylated horseradish peroxidase after 25 hours [144]. Another group assessed the release of covalently bound VEGF in a 4-arm poly(ethylene glycol)-maleimide (PEG-4MAL) microgel with protease-sensitive crosslinker VPM and hydrolytically degradble DTT [22]. VEGF was covalently bound to the PEG-4MAL network via the reactive thiol group on VEGF and the thiol group on PEG [22]. They found PEG-4MAL gels with incorporated VMP in the presence of collagenase achieved 100% release of loaded VEGF after 70 hours of incubation [22]. Additionally, they demonstrated that PEG-4MAL gels with incorporated VMP or DTT in the presence of PBS alone achived roughly 20% release of loaded VEGF after 70 hours of incubation [22].

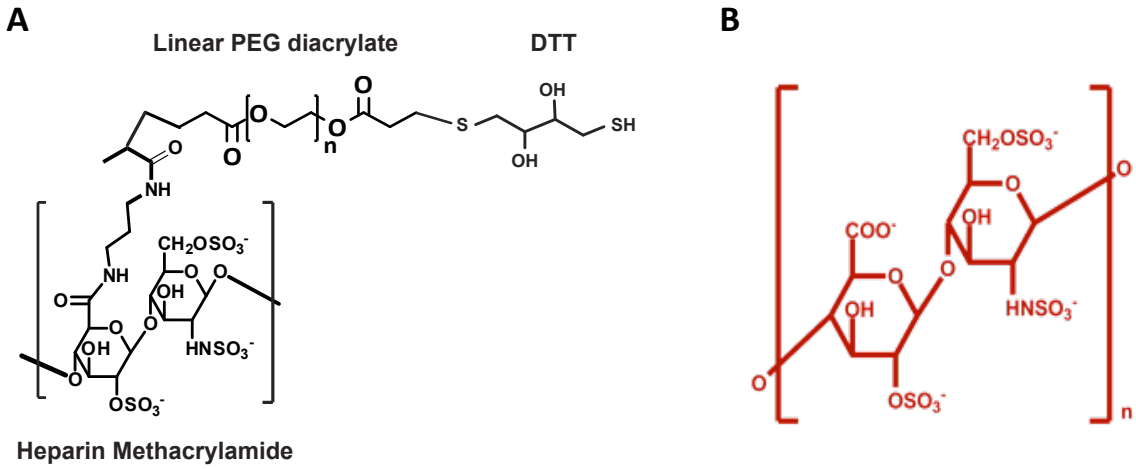

Figure 2.2: Chemical structure of heparin based biomaterials. (A) Chemical structure of degradable heparin-based biomaterial fabricated via Michael type addition and free radical polymerization. (B) Disaccharide Unit of Heparin glycosaminoglycan. *Adapted from Tellier LE, Treviño EA, Brimeyer AL, Reece DS, Willett NJ, Guldberg RE, Temenoff JS. Intra-articular TSG-6 delivery from heparin-based microparticles reduces cartilage damage in a rat model of osteoarthritis. Biomaterials science. 2018;6(5):1159-67.*

Lastly, PEG can be functionalized with additional biomolecules to modulate controlled release. Heparin is a negatively charged glycosaminoglycan that is naturally produced by mast cells [150]. Heparin has been extensively used in PEG-based biomaterials applications because it is biocompatible, relatively non-toxic, and inexpensive [151]. The highly negative charge of heparin makes it an attractive material for release of positively charged proteins and has been shown to protect bound proteins [35,152–154]. Heparin is negatively charged due to the presence of various sulfate groups along the backbone. Our laboratory has the capacity to selectively remove sulfate groups from heparin, which have been shown to modulate protein release and can alter the protective properties of heparin [35,153]. Our laboratory and others have used heparin and its desulfated analogs for a variety of studies. We previously found that native heparin can maintain bone morphogenetic protein-2 (BMP-2) activity under thermal stress in a concentration dependent manner [153]. Additionally, we found that more

desulfated forms of heparin were unable to protect BMP-2 from thermal stress to the same extent [153]. Similarly, we found that incorporation of more sulfated heparin into PEG-based microparticles caused faster microparticle degradation, significantly more BMP-2 release, and significantly more BMP-2 bioactivity compared to more desulfated heparin microparticle groups [35]. Additionally, we found that incorporation of more sulfated heparin into PEG-based hydrogels resulted in greater amounts of anti-inflammatory, small molecule, positively charged crystal violet [36]. Furthermore, we found that fully sulfated heparin and N-desulfated heparin significantly enhanced the anti-plasmin activity of TSG-6 activity *in vitro*. We found that treatment with 10% N-desulfated heparin microparticles loaded with TSG-6 prevented significant knee degeneration in an rat model of osteoarthritis [20]. While heparin can be used to modulate sustained release of positively charged proteins, it can also be used to sequester positively charged proteins [37].

2.4.3 Microfluidic Devices

Historically our laboratory and others have fabricated microparticles with a homogenizer and a water-in-oil emulsion system [19,20,35,37,152]. A major drawback of this system is the inability to control microparticle size, which generates microparticles with a wide distribution of sizes. Fabricating microparticles that are too large or small would consequently require filtering, which wastes materials and time. Furthermore, in order to use the microparticles to release therapeutics, the therapeutics would need to be loaded onto the microparticles after fabrication (post-loading), which would require more time and waste potentially expensive therapeutics. Post-loading is inherently wasteful

because therapeutic molecules do not necessarily bind microparticles with 100% efficiency [35,153].

An alternative method to fabricate microparticles is the use of a microfluidic device, which have become increasingly popular due to their distinct advantages [26]. Microfluidic devices create a water-in-oil emulsion at a small scale, which allows for greater control of microparticle size [26]. Thus, microfluidic devices can synthesize uniformly sized microparticles, which eliminates the need for filtering and reduces material waste and time. Additionally, the characteristic control of a microfluidic device ensures that all of the polymer solution is introduced into the device and turned into microparticles. Thus, any expensive crosslinkers added to the polymer solution will be incorporated into the resulting microparticles, which eliminates waste. Furthermore, therapeutics can also be added to the polymer solution, eliminating the time and therapeutics waste characteristic of post-loading.

To fabricate microparticles with a microfluidic device two immiscible phases are used: the continuous phase and the discontinuous phases. In a water-in-oil system, the continuous phase would consist of oil and the discontinuous phase would consist of the water soluble polymer solution. Unlike a homogenizer that creates a water-in-oil emulsion through mechanical or shear force, a microfluidic device creates an emulsion by uniform breakup of a stream of the discontinuous phase [26]. Microparticle size can be tuned by adjusting several parameters. Previous work has shown that higher phase speeds cause increased shear stress on the microparticle droplet [26]. The increased shear stress causes more frequent discontinuous phase stream break-up and consequently generates smaller microparticles [26]. When the microparticle droplet is smaller than the syringe

needle, the force applied is negligible [26]. However, as the discontinuous phase is continuously injected via the syringe pump, the microparticle droplet will increase in size and the applied force will similarly increase [26]. The increased force on the microparticle droplet causes it to be pinched off from the tip of the needle [26].

Furthermore, microparticle size can be tuned by the amount of surfactant used in the system. It has previously been shown that particle size decreases with increasing amounts of surfactants [28]. Microfluidic devices that utilize immiscible phases to fabricate microparticles use surfactants to stabilize the shape of the microparticles and prevent coalescence of microparticles [27]. There is a thermodynamic driving force towards homogenization of the system whereby all microparticles coalesce and minimize contact with the oil-based continuous phase [27]. To overcome this thermodynamic driving force, surfactants are added to stabilize microparticles. Without the addition of surfactants, when microparticle droplets come into close contact the continuous phase between them will be depleted and allow the microparticle droplets to coalesce [27]. However, in the presence of surfactants on any two microparticle droplets, steric repulsion of the surfactant molecules will prevent the depletion of the continuous phase, which lengthens the time to continuous phase depletion and stabilizes both microparticles droplets against coalescence [27]. Previous groups that have investigated surfactants in the context of microfluidic devices have found that microparticle stability increases with increasing amounts of surfactants, which result in microparticle sizes of decreasing size [28,155]. However, using increasingly greater amounts of surfactant will eventually result in a microparticle size plateau, where the microparticle droplets are saturated with

surfactant molecules. The surfactant threshold varies depending on microparticle droplet size, the surfactant used, and the size of the microfluidic device [28].

Various microfluidic device systems have been developed for fabrication of microparticles with a variety of uses. Of particular interest, microfluidic device platforms have been developed that allow for incorporation of additional biomolecules and cellular encapsulation [156]. The Garcia laboratory fabricated a poly(dimethyl siloxane) (PDMS) microfluidic device using soft lithography and flow-focusing microfluidic chip [156]. They were able to fabricate uniformly sized PEG-4MAL microparticles with incorporated hydrolytically degradable crosslinker DTT, cell binding peptide RGD, and encapsulated islet cells [156]. They demonstrated that they could fabricate these complex microparticles with a size range from 137 – 300 μm by varying the continuous flow rates [156]. Additionally, they demonstrated selective permeability of loaded biomolecules depending on the size [156]. Specifically, they showed that microparticles loaded with insulin and glucose achieved near 100% release over 70 hours, while larger molecules such as immunoglobulin G (IgG) achieved about 25% release over 70 hours [156]. They demonstrated that encapsulated islet cells maintained high levels of viability over at least 8 days post-fabrication [156].

While PDMS-based microfluidic devices have the capacity to fabricate microparticles with a wide range of applications, there are several drawbacks to using this platform. Namely, the channels can leak and become clogged with polymer debris in the course of microparticle fabrication [26], which would compromise microparticle yield and quality. Additionally, many organic solvents are incompatible with PDMS molds because they can cause swelling [26] and compromise the flow of the immiscible phases.

More recently, several laboratories have begun to investigate simple microfluidic devices to overcome the characteristic problems of PDMS molds [26]. The Xia laboratory has fabricated a simple microfluidic device consisting of poly(vinyl chloride) (PVC) tubing, a syringe needle, and a glass capillary tube [26]. Their microfluidic device prevents the discontinuous phase from coming into contact with the capillary wall, which eliminates the risk of clogging seen in PDMS molds [26]. The Xia laboratory microfluidic device was able to synthesize microparticles from hydrophobic polymer poly(ε-caprolactone) (PCL) and hydrophilic, natural polymer gelatin [26]. In this microfluidic device platform, the discontinuous and continuous phases are introduced using syringe pumps with independently adjustable flow rates and allowed to mix at the end of the syringe needle [26]. The PCL microparticles were fabricated in an oil-in-water emulsion with a poly(vinyl alcohol) (PVA) continuous phase and were solidified via solvent extraction and evaporation in the collection phase, which also consisted of PVA [26]. The PCL microparticle size range with this simple microfluidic device platform was 75 – 230 μm [26]. Using the same microfluidic device, the Xia laboratory also fabricated gelatin microparticles with a continuous phase of toluene and span-80 [26]. Gelatin microparticles were collected in a solution of ethanol to allow for crosslinking and can be vacuum dried prior to use [26].

CHAPTER 3 FULL-THICKNESS ROTATOR CUFF TEAR IN RAT RESULTS IN DISTINCT TEMPORAL EXPRESSION OF MULTIPLE PROTEASES IN TENDON, MUSCLE, AND CARTILAGE[1]

3.1 Introduction

Rotator cuff tears, including partial and full-thickness tears of the supra- and infraspinatus tendons, are among the most common shoulder injuries and result in over 75,000 surgical repairs annually [157]. Following rotator cuff tear, several tissues are negatively affected including the tendon, its respective muscle, and articular cartilage in the shoulder joint. Such damage includes tendon disorganization with decreased collagen content [2], muscle atrophy, and fibrous tissue and fatty deposits within the muscle [3]. Additionally, the force balance between tendons of the rotator cuff is disrupted, which may lead to the development of osteoarthritic changes in the articular cartilage including loss of glycosaminoglycan (GAG) content, increased surface roughness, and loss of cartilage tissue [4,5].

While damage to joint tissue following rotator cuff tear is well documented, the exact biochemical processes responsible for extracellular matrix (ECM) turnover that contribute to this damage remain unknown. In joint tissues, both ECM components and

[1] Portions of this chapter were adapted from Treviño EA, McFaline-Figueroa J, Guldberg RE, Platt MO, Temenoff JS. Full-thickness rotator cuff tear in rat results in distinct temporal expression of multiple proteases in tendon, muscle, and cartilage. Journal of Orthopaedic Research. 2019 Feb;37(2):490-502.

the proteases that degrade them are secreted for the purposes of tissue remodeling [9]. For example, tenocytes have been shown to alter the rate of collagen synthesis [62] as well as protease secretion [63] in response to changes in mechanical loading. Furthermore, an acute injury such as rotator cuff tendon tear could incite an inflammatory response, whereby inflammatory cells such as neutrophils and macrophages would be recruited to the area. It is well known that inflammatory cells have the capacity to secrete proteases [67,68] that may further contribute to the net shift towards ECM degeneration. Thus, an imbalance between anabolic and catabolic factors through the increased presence of active proteases could be responsible for the decrease in ECM components, such as collagen and elastin [47,66], observed following rotator cuff tendon tear.

Cathepsins are papain-family cysteine proteases known to be some of the most powerful elastases and collagenases, are often associated with ECM remodeling and therefore warrant investigation in rotator cuff tear pathology [69]. Cathepsin K, canonically associated with osteoclasts and bone remodeling, has been previously observed in osteoporosis and osteoarthritis [10,38]. In particular, prior work has identified a positive correlation between amount of cathepsin K present and osteoarthritis severity in mice [158] and cathepsin L has been shown to be upregulated in instances of muscle atrophy in both rats and mice [104,110]. Additionally, our previous work investigating tendinopathy [14,15] has demonstrated upregulated cathepsin activity in the tendon at 4 and 8 weeks of overuse in a rat model.

Furthermore, matrix metalloproteinases (MMPs), zinc-dependent endopeptidases that play a role in ECM remodeling, have been previously implicated in tendon degeneration, muscle atrophy, and osteoarthritis development. Specifically, MMP-1

activity has been shown to be significantly greater in human supraspinatus tendon following rupture [122] and MMP-1 and -3 have been shown to be upregulated within synovial fluid following rotator cuff tendon tear in humans [123]. Additionally, MMP-2, -9, and -13 have been shown to be more active in osteoarthritic cartilage compared to healthy cartilage in both humans and rats [124,125], while increases in MMP-2 and -9 activity positively correlated with the occurrence of muscle atrophy in rats [110,126].

Both the cathepsin and MMP families contain potent collagenases and elastases, and thus are often seen in the same degenerative injury. For example, cathepsin L and MMP-2 have been observed to be upregulated in instances of muscle atrophy [110,126]. Interestingly, while both families of proteases can cleave collagen, they do so at different locations within the molecule and at different catalytic rates [104], and thus may act synergistically to enhance ECM degradation. Furthermore, cathepsins have the ability to cleave and activate pro-MMPs [31], which suggests they can work sequentially to digest collagen and promote tissue degradation [104]. Due to their shared substrates and cross-activation, it is important to investigate both families of enzymes individually and in connection to one another to better understand how proteases play a role in tissue degeneration after rotator cuff tear.

Thus, using early, middle, and late time points (1, 3, and 12 weeks respectively), the ***objective*** of this study was to characterize the protease activity profile over time in joint tissue following acute, full-thickness rotator cuff tear, and to relate these results to the timing of observed tissue structural damage, as monitored by histology or microcomputed tomography (μCT) imaging. To our knowledge, no work has investigated both families of proteases within all three soft tissues of the joint after full-thickness

rotator cuff tears. We ***hypothesize*** that acute, full-thickness rotator cuff tear will result in significantly more protease activity (cathepsins and MMPs) early after injury in supraspinatus tendon (1 week), with delayed responses from cartilage and supraspinatus muscle (3-12 weeks after injury). Additionally, we ***hypothesize*** that protease upregulation timing will coincide with manifestation of visible tissue damage (as assessed by histology and/or μCT imaging) in each tissue. A summary of outcome measures for each tissue over time can be found in Table 1.

3.2 Materials and Methods

3.2.1 Surgical Procedure and Outcome Measure Time Points

Rotator cuff injury was induced using a method previously established [19,88]. This animal model was chosen as muscle degeneration, an outcome we aim to characterize in this study, does not occur to a large degree in other models, such as tendon transection only, in rats [23]. Male Sprague-Dawley rats (N=30 total, 250-300 g initial weight and 8-10 weeks old) were used in accordance with protocols approved by the Georgia Institute of Technology Institutional Animal Care and Use Committee (Protocol #A15050). To induce injury, on the left side of the animal, a 5 mm portion of the suprascapular nerve was resected, and both the supraspinatus and infraspinatus tendons were transected at the insertion into the humeral head. The wound was closed using Vicryl 4-0 absorbable sutures (Ethicon) and wound clips. The right forelimb of each animal served as an internal, uninjured contralateral control. Because rats are quadrupeds and do not have a dominant forelimb for daily activities, we did not deem it necessary to randomize for this study.

Table 3.1: Experimental design and outcome measures performed in all three joint tissues over time.

	1 week	3 weeks	12 weeks
Supraspinatus Tendon	Zymography (N=6)	Zymography (N=8)	Zymography (N=6)
	Histology (N=3)	-	-
Supraspinatus Muscle	Zymography (N=6)	Zymography (N=8)	Zymography (N=6)
	Histology (N=3)	-	-
Humeral Head Cartilage	Zymography (N=6)	Zymography (N=6)	Zymography (N=3)
	EPIC μCT (N=8)	-	EPIC μCT (N=8)

Time points for this study were chosen based on previous data from our laboratory as well as when we expected to see significant structural damage in each tissue. Due to the acute injury of the tendon, we expected to observe damage to this tissue soon after injury and chose 1 week to capture effects of acute inflammation [159]. For muscle, we have previously shown significant fibrous tissue infiltration (indicative of muscle degeneration) 3 weeks following tendon injury [19]. In our previous studies with tendon overuse injuries [15], we have observed concomitant humeral head cartilage damage by 12 weeks after tendon injury onset.

3.2.2 Histology

Following tissue isolation, supraspinatus muscles and tendons (N=3) were fixed with 4% paraformaldehyde, embedded in optimum cutting temperature (OCT), and frozen in a liquid nitrogen-cooled ethanol. Supraspinatus muscle tissue was cross-sectioned and supraspinatus tendon tissue was sectioned longitudinally in 7 μm slices using a cryostat (CryoStar NX70, Thermo Fisher). Supraspinatus muscle sections were

stained with Masson's trichrome and hematoxylin and eosin (H&E) stains (VWR and Richard Allan Scientific respectively). Supraspinatus tendon sections were stained with H&E and both tissues were imaged using light microscopy (Nikon TE2000). For analysis, eight sections of supraspinatus tendon (each section was imaged at both proximal and distal ends) per sample and 12 sections of supraspinatus muscle per sample were used.

3.2.3 Quantification of Collagen Alignment in Tendon

Tendon sections (N=3) were imaged using a Zeiss 710 NLO inverted confocal microscope (Carl Zeiss Microscopy) with a mode-locked Ti:Sapphire Chameleon Ultra laser (Coherent Inc.) in combination with non-descanned detection (NDD) to visualize the collagen fibers and quantify their orientation and distribution as previously described [160]. The laser was set to 800 nm and emission was filtered from 380 - 430 nm. Second harmonic generation (SHG) images were collected using a Plan-Apochromat 20x objective and Zeiss ZEN software. The fiber direction was estimated using OrientationJ distribution, an ImageJ plug-in (NIH) developed for directional analysis. A distribution of local angles was generated for each optical slice, where 0° aligned to the horizontal axis (length-wise along the tendon) and ± 90° to the vertical axis. The mean and standard deviation of collagen fiber orientation was calculated from the distribution of each image. For analysis, eight sections of supraspinatus tendon (each section was imaged at both proximal and distal ends) were used.

3.2.4 Micro-computed Tomography (μCT)

Humeral head samples (N=8) were analyzed by EPIC-μCT (Equilibrium Partitioning of an Ionic Contrast-Microcomputed tomography) based on established techniques [15,161]. EPIC-μCT involves the use of a contrast agent to better visualize less radio-opaque tissues, such as cartilage. In this work, Hexabrix (Covidien) was employed, which is negatively charged and is therefore electrostatically repulsed due to the high amounts of negative charge on biomolecules such as proteoglycans found in cartilage. Therefore, cartilage attenuation is inversely related to proteoglycan content within the tissue.

Following isolation at 1 and 12 weeks following injury, humeral heads were submerged in a 10% Hexabrix solution at 37°C for 30 min. Humeral heads were scanned in the sagittal plane with the μCT50 (Scanco Medical) at 45 kVp, 200 μA, and a 600 ms integration time. Following segmentation and reconstruction, control and injured humeral heads were evaluated for cartilage volume, cartilage thickness, and cartilage attenuation using Scanco evaluation software. Hexabrix was removed from humeral head sample by incubating in PBS at 37°C for 30 min. The same contrast-enhanced scans were used to analyze subchondral and trabecular bone via Scanco evaluation software. Analysis of subchondral bone included thickness, volume, and density, while trabecular bone included volume and density. Additionally, the same scans were used to evaluate the subchondral bone directly under focal defects at 12 weeks. Control humeral heads were evaluated in the same region of the humeral head with equivalent numbers of slices.

3.2.5 Multiplex Gelatin Zymography

Following sacrifice, joint tissues were collected. Supraspinatus tendon and muscle were isolated together and then separated through fine-dissection under a stereomicroscope (Leica model: 165FC). Cartilage was carved from the humeral head using a scalpel. Tissues were homogenized using a sample grinding kit (GE Healthcare Life Sciences) and zymography lysis buffer (consists of 20 mM Tris-HCl, 5 mM EGTA, 150 mM NaCl, 20 mM glycerol-phosphate, 10 mM NaF, 1 mM sodium orthovanadate, 1% Triton-X 100, and 0.1% Tween 20 in 500 mL deionized water) with 0.1 mM freshly added leupeptin to stabilize proteins. Protein concentration was determined by microBCA kit (Thermo Fisher).

Cathepsin and MMP zymography was performed as previously described [69,162]. For supraspinatus muscle and tendon tissues (N=6-8), 15 µg of protein under non-reduced conditions were loaded on either 12.5% (cathepsin) or 10% (MMP) SDS–polyacrylamide gels laden with 0.2% gelatin substrate. For cartilage tissues (N=3-6), 10 µg of protein under non-reducing conditions were loaded onto 7.5% SDS–polyacrylamide gels laden with 0.2% gelatin substrate into both cathepsin and MMP gels. Recombinant proteins were used as positive controls on all gels. Recombinant cathepsin K (Enzo) was used for cathepsin zymograms at pH=6, recombinant cathepsin L (R&D Systems) was used for cathepsin zymograms at pH=4, and recombinant MMP-2 (R&D Systems) was used for MMP zymograms.

After separation by size, gels were washed in their respective renaturing buffer to allow proteases to return to active confirmation. Gels were incubated in their respective

assay buffer at 37°C for 18 hours to allow degradation of gelatin within gels. After rinsing with DI water, gels were stained with Coomassie Brilliant Blue (Thermo Fisher) for 1 hour at room temperature and constant agitation and destained for 1 hour under the same conditions. Gels were imaged using ImageQuant LAS 4000 (GE Healthcare) and densitometry analysis was performed using ImageJ (NIH).

3.2.6 Immunostaining

Immunostaining of supraspinatus tendon 1 week following injury (N=3) was used to confirm the presence of inflammatory cells within the joint. Supraspinatus tendon sections were rinsed with PBS to remove OCT and blocked with 5% goat serum (R&D) for 1 hour at room temperature. Ly6g+ FITC primary antibody (abcam ab25024) diluted in 5% goat serum (1:100) was applied to sections for 1 hour at room temperature in the dark. CD68+ primary antibody (abcam ab955) was applied to sections (1:200) and incubated overnight at 4°C in a humid chamber. Following three PBS washes, secondary antibody (abcam ab150113) was added to sections (1:500) for 1 hour at room temperature in the dark. Following antibody incubation, sections were washed with PBS and incubated with Hoechst (1:1,000) counterstain (Sigma-Aldrich) for ten minutes at room temperature in the dark. Following three PBS washes, sections were mounted and imaged immediately using confocal microscopy (Zeiss). Incubation with secondary antibody alone (i.e. no primary antibody) was used as a negative control to verify the absence of non-specific binding. To quantify the number of inflammatory cells within the tendon, ImageJ (NIH) was used to count total Hoechst stained cells and CD68+ or Ly6g+ cells using the color threshold analysis tool. Data is presented as total number of immune cells

divided by total cells. The same parameters were used for injured and control images. Eight sections of supraspinatus tendon per sample were stained and quantified.

3.2.7 Statistical Analysis

Power analysis (G*Power software) was performed on prior data [14,15] for both zymography ($\alpha = 0.05$, $\beta = 0.8$, $\Delta = 0.48$) and μCT ($\alpha = 0.05$, $\beta = 0.8$, $\Delta = 0.75$) to determine number of animals required for this study. Prior to statistical analysis, we performed a Shapiro-Wilk normality test to ensure our data was normally distributed and could undergo parametric tests. For humeral head evaluation (bone and cartilage) via μCT and zymography analysis with multiple time points, statistical significance was determined using a two-way ANOVA and Tukey's post-hoc test ($p \leq 0.05$) in GraphPad on raw values. Densitometry analyses of zymograms are graphed as fold change compared to uninjured contralateral control samples. For humeral head evaluation of bone at a single time point, a student t-test (two-tailed, $p \leq 0.05$) was used. To determine collagen alignment within supraspinatus tendon tissue for different samples, a student's t-test ($p \leq 0.05$) was used to compare the distribution of fiber orientation from zero degrees.

3.3 Results

3.3.1 Histology

H&E staining revealed that the control supraspinatus tendon showed dense, aligned collagen fibers and elongated cells at both the proximal and distal sections of the tendon 1 week following injury. In contrast, the injured supraspinatus tendon demonstrated cellular infiltration and changes in collagen alignment and orientation at

both the proximal and distal portions of the tendon (Figure 3.1a). The average alignment of collagen fibers in the control supraspinatus tendon relative to 0° was 8.5° ± 16.7° (distal) and 9.9° ± 16.0° (proximal), while the injured tendon had an average collagen alignment of -11.8° ± 51.7° (distal) and -8.3° ± 46.9° (proximal). The control supraspinatus tendon had significantly more aligned collagen fibers compared to the injured supraspinatus tendon at 1 week following injury (Figure 3.1b). Supraspinatus muscle samples were qualitatively analyzed using both H&E and Masson's trichrome. Both stains revealed similar morphology in control and injury muscle fibers, with little evidence of fibrous degeneration at this time point (Figure 3.2).

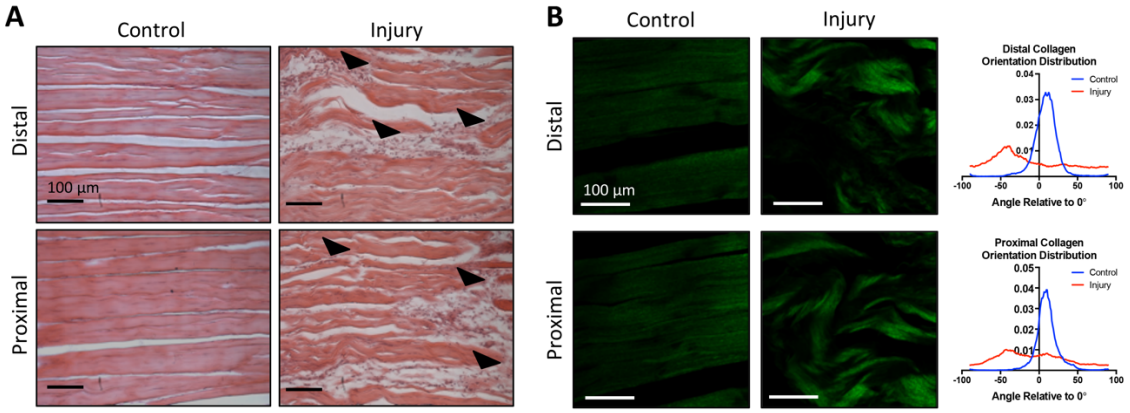

Figure 3.1: One week after injury tendon undergoes noticeable damage. (A) H&E staining of longitudinally-sectioned tendon reveals damage 1 week after injury, indicated by changes in collagen structure and cellular infiltration (arrowheads) (B) Second Harmonic Generation images of collagen within tendon sections with quantification of orientation distribution. The average alignment of collagen fibers in the control supraspinatus tendon relative to 0° was 8.5° ± 16.7° (distal) and 9.9° ± 16.0° (proximal), while the injured supraspinatus tendon had an average collagen alignment of -11.8° ± 51.7° (distal) and -8.3° ± 46.9° (proximal) relative to 0°. The orientation of collagen fibers in injured supraspinatus tendon was significantly different from control ($p<0.05$). Scale bars are 100 µm.

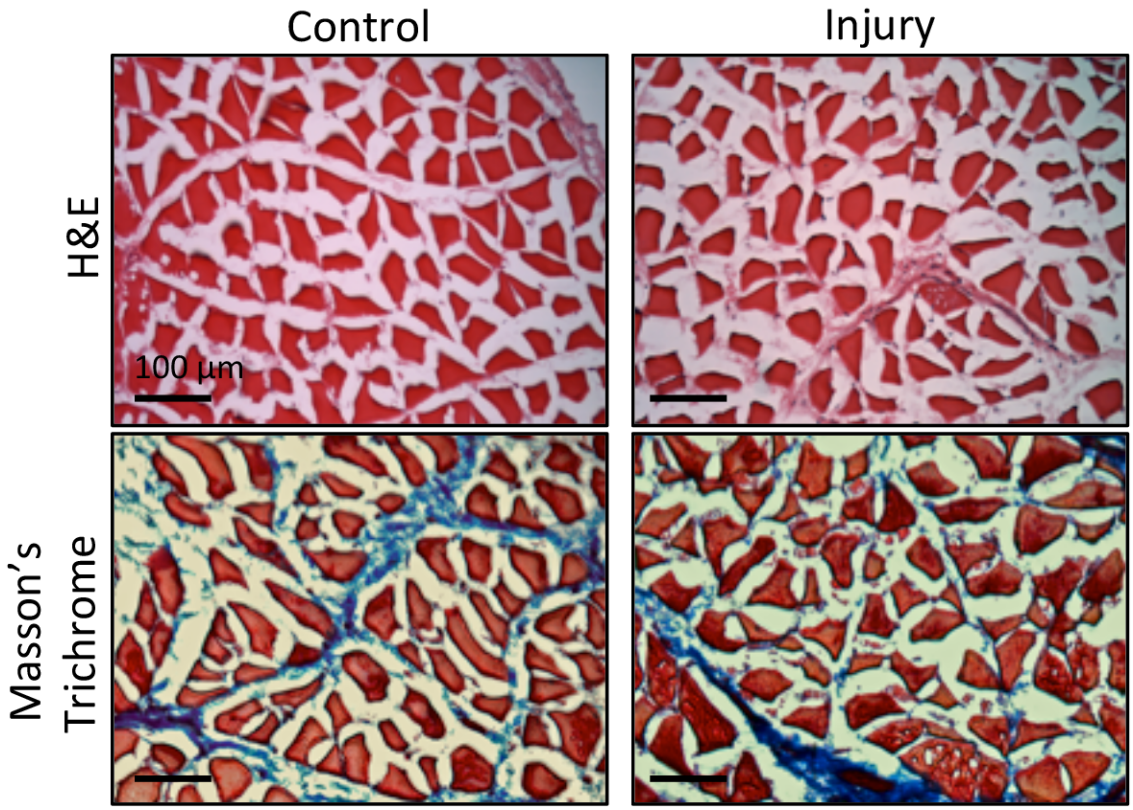

Figure 3.2: One week after injury muscle remains similar to control. H&E and Masson's trichrome staining of muscle cross-sections shows no differences compared to uninjured control 1 week after injury. Scale bar is 100 µm.

3.3.2 EPIC-µCT Analysis of Humeral Articular Cartilage, Subchondral Bone, and Trabecular Bone

Some animals developed localized loss of cartilage (focal defects) by 12 weeks following rotator cuff injury (4 of 8 animals), while no focal defects were observed in control cartilage or injured cartilage at 1 week (Figure 3.4a). Focal defects had an average volume of 0.12 ± 0.09 mm^3 and did not manifest in similar regions of the humeral head cartilage between animals (Figure 3.3). Previous work investigating rat knee cartilage demonstrated consistent defects in the medial third of cartilage in an animal model of osteoarthritis [161]. Despite the presence of focal defects in half of injured animals, there were no significant differences in cartilage volume, thickness, or attenuation (inversely

related to (GAG) content) between control and injury groups at either time point (Figure 3.4b). Analysis of humeral head subchondral bone showed no significant differences in bone volume, thickness, or density between injured and uninjured groups at either time point (Figure 3.5a-c). However, within each group, there was a significant increase in subchondral bone volume, thickness, and density, between 1 and 12 weeks. Analysis of trabecular bone at 12 weeks showed no significant differences in bone volume between injury and control groups (Figure 3.5d-e). Analysis of subchondral bone directly under the focal defect showed no difference in thickness, but significantly greater bone density (Figure 3.5f-g) on the injured side compared to control at 12 weeks.

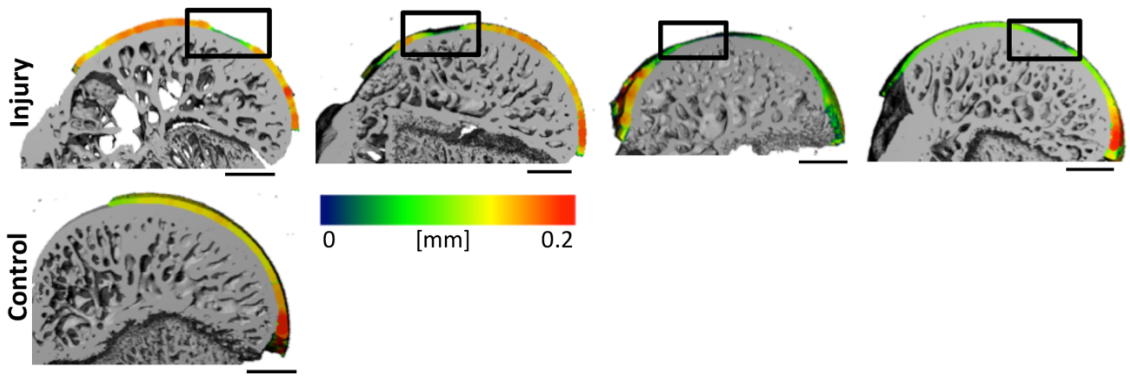

Figure 3.3: µCT analysis demonstrates that focal defects do not occur in the same location on humeral heads between animals. 3D reconstruction of humeral head cartilage thickness with overlaid bone 12 weeks following injury. Black box indicates location of focal defect. Scale bar = 1 mm.

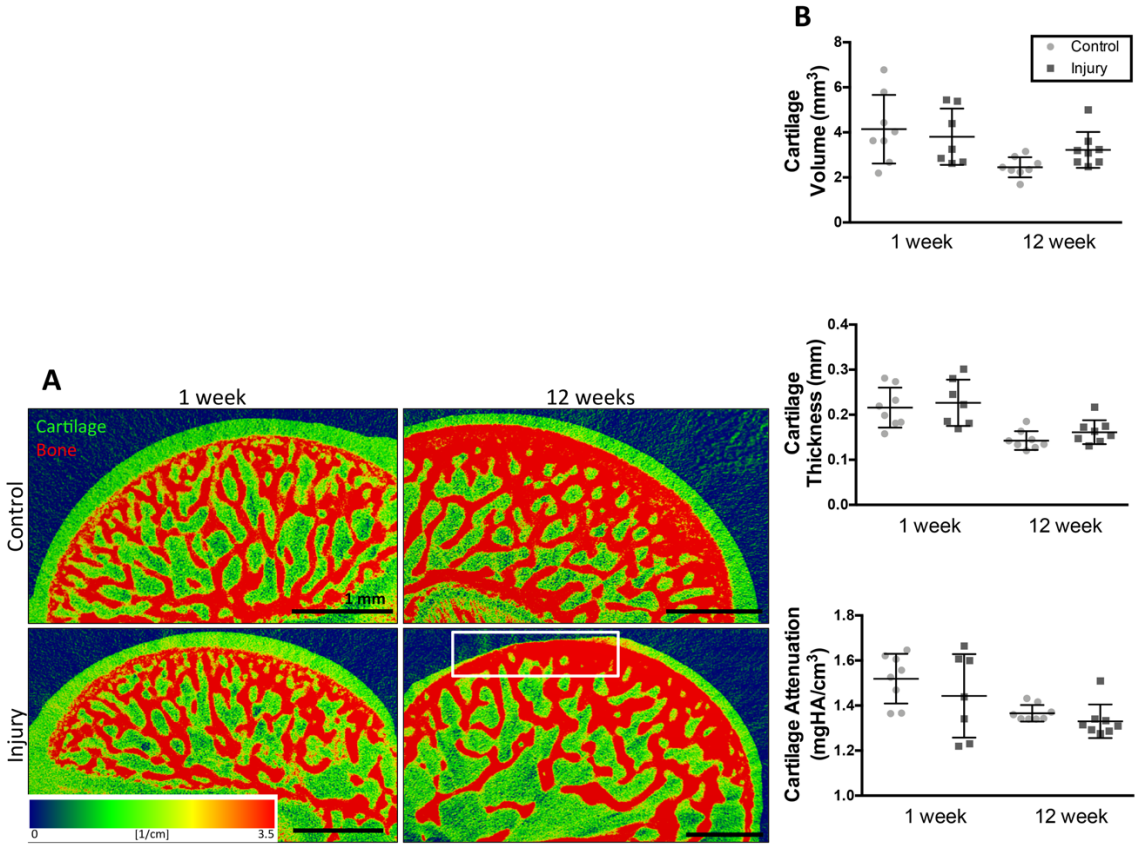

Figure 3.4: Contrast enhanced microCT reveals focal defects within cartilage 12 weeks post-injury. (A) contrast enhanced microCT of humeral heads. Loss of cartilage (focal defects) highlighted in white box. Defects present in 4 out of 8 animals. N=8. scale bar = 1mm. (B) Evaluation of cartilage thickness, cartilage volume, and cartilage attenuation. N=8, no significant differences present.

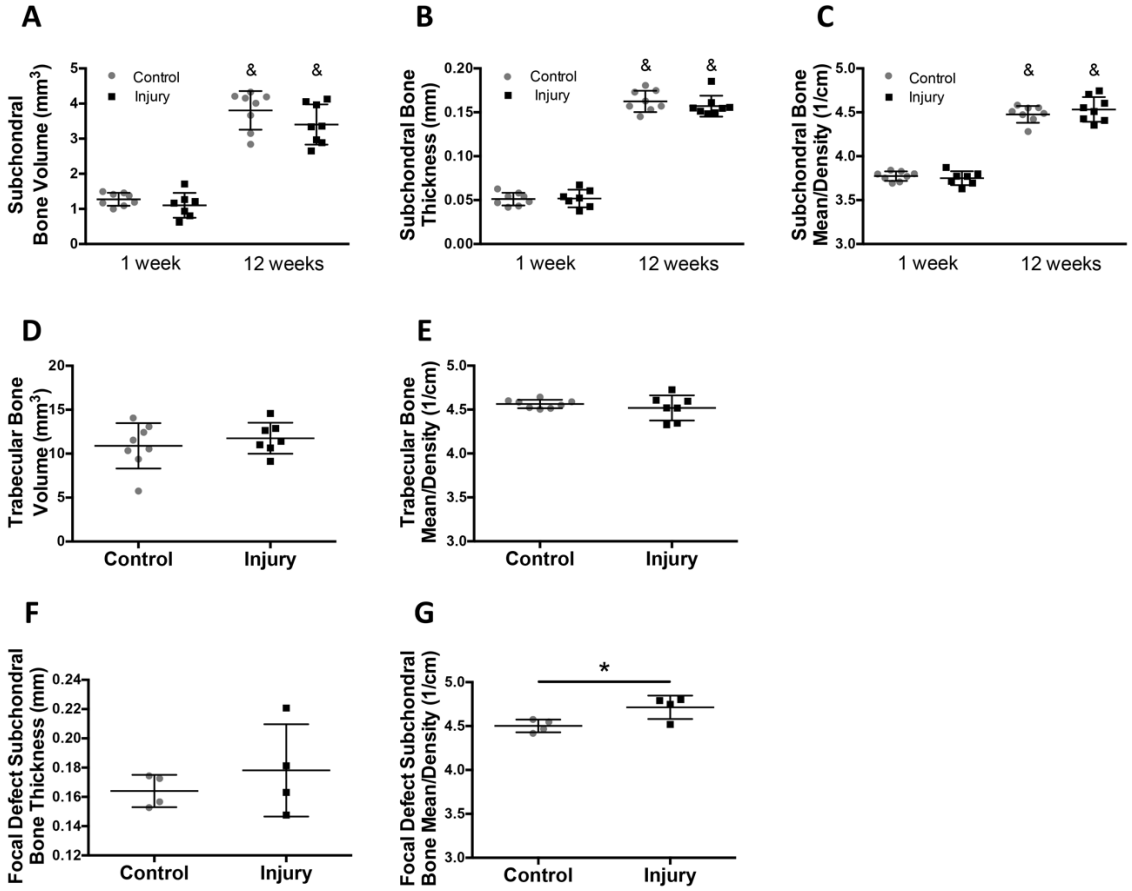

Figure 3.5: µCT analysis demonstrates few differences in humeral head bone following injury. (A) Subchondral bone volume (B) Subchondral bone thickness (C) Subchondral bone density (D) Trabecular bone volume (E) Trabecular bone density (F) Subchondral bone thickness directly under focal defect (G) Subchondral bone density directly under focal defect. A-E: N=8, F-G: N=4 *$p<0.05$, & indicates significantly different from 1 week samples.

3.3.3 Active Cathepsins and MMPs in Supraspinatus Tendon

Active cathepsin L was found in pH4 and pH6 cathepsin zymograms between 37 and 25 kDa (Figure 3.6a and 3.6c) and pro- and mature MMP-2 were detected in MMP zymograms (Figure 3.6e) between 50 and 75 kDa at all three time points (1, 3, and 12 weeks post-injury). Densitometric analysis revealed significantly higher amounts of active cathepsin L in injured supraspinatus tendon with an average of 5 fold increase over

control supraspinatus tendon at 1 week post-injury (Figure 3.6b and 3.6d). Additionally, active MMP-2 was significantly increased in injured supraspinatus tendon with an average of 10 fold increase over control supraspinatus tendon at 1 and 3 weeks post-injury (Figure 3.6f). There were no significant changes in protease activity at 12 weeks compared to control. Additionally, we investigated the amount of active protease over time within control supraspinatus tendon (Figure 3.10a-c). We found that there is a significant increase in the amount of active cathepsin L from 1 week to 3 weeks with a plateau between 3 and 12 weeks, whereby the amount of active cathepsin L is maintained.

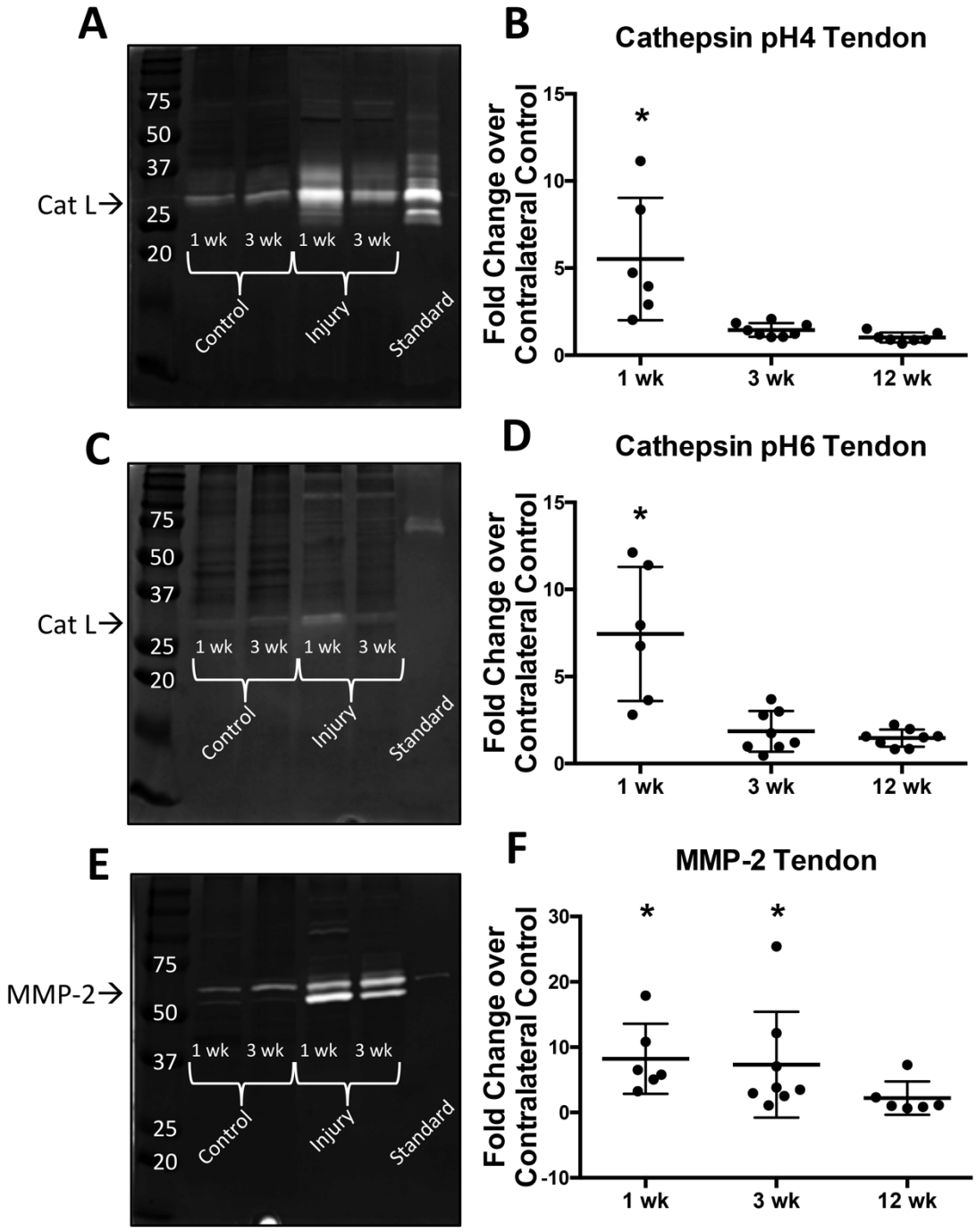

Figure 3.6: Gelatin zymography of tendon shows significant increase of proteases following injury. (A-B) cathepsin (pH=4 buffer) zymography gel and densitometry quantification (C-D) cathepsin (pH=6 buffer) zymography gel and densitometry quantification (E-F) MMP zymography gel and densitometry quantification. Recombinant protein used as standard: cathepsin L, cathepsin K, MMP-2 respectively. *$p<0.05$. N=6-8.

3.3.4 Active Cathepsins and MMPs in Supraspinatus Muscle

Active cathepsin L was found in pH4 and pH6 cathepsin zymograms between 37 and 25 kDa (Figure 3.7a and 3.7c) and pro- and mature MMP-2 were detected in MMP zymograms (Figure 3.7e) between 50 and 75 kDa at all three time points (1, 3, and 12 weeks post-injury). Densitometric analysis of cathepsin pH6 and cathepsin pH4 zymograms revealed significantly higher active cathepsin L (~5 fold increase) in injured supraspinatus muscle compared to control supraspinatus muscle at 1 week post-injury (Figure 3.7b and 3.7d). Additionally, cathepsin pH6 zymograms showed a continued increase in active cathepsin L (~5 fold increase) 3 weeks after injury (Figure 3.7d). The amount of active cathepsins within the supraspinatus muscle was comparable to the uninjured control at 12 weeks following injury. Active MMP-2 was significantly increased in injured supraspinatus muscle with an average 4 fold increase over control supraspinatus muscle at 3 weeks post-injury (Figure 3.7f), while there were no significant changes in the amount of active MMP at 1 and 12 weeks compared to control.

Additionally, we investigated the amount of active protease over time within control supraspinatus muscle (Figure 3.10d-f). Cathepsin pH4 zymograms demonstrated a significant increase in the amount of active cathepsin L from 1 week to 3 weeks with a plateau between 3 and 12 weeks, whereby the amount of active cathepsin L is maintained (Figure 3.10d). Conversely, cathepsin pH6 zymograms demonstrated low levels of cathepsin L with a significant increase in the amount of active cathepsin L at 12 weeks compared to 1 and 3 weeks (Figure 3.10e).

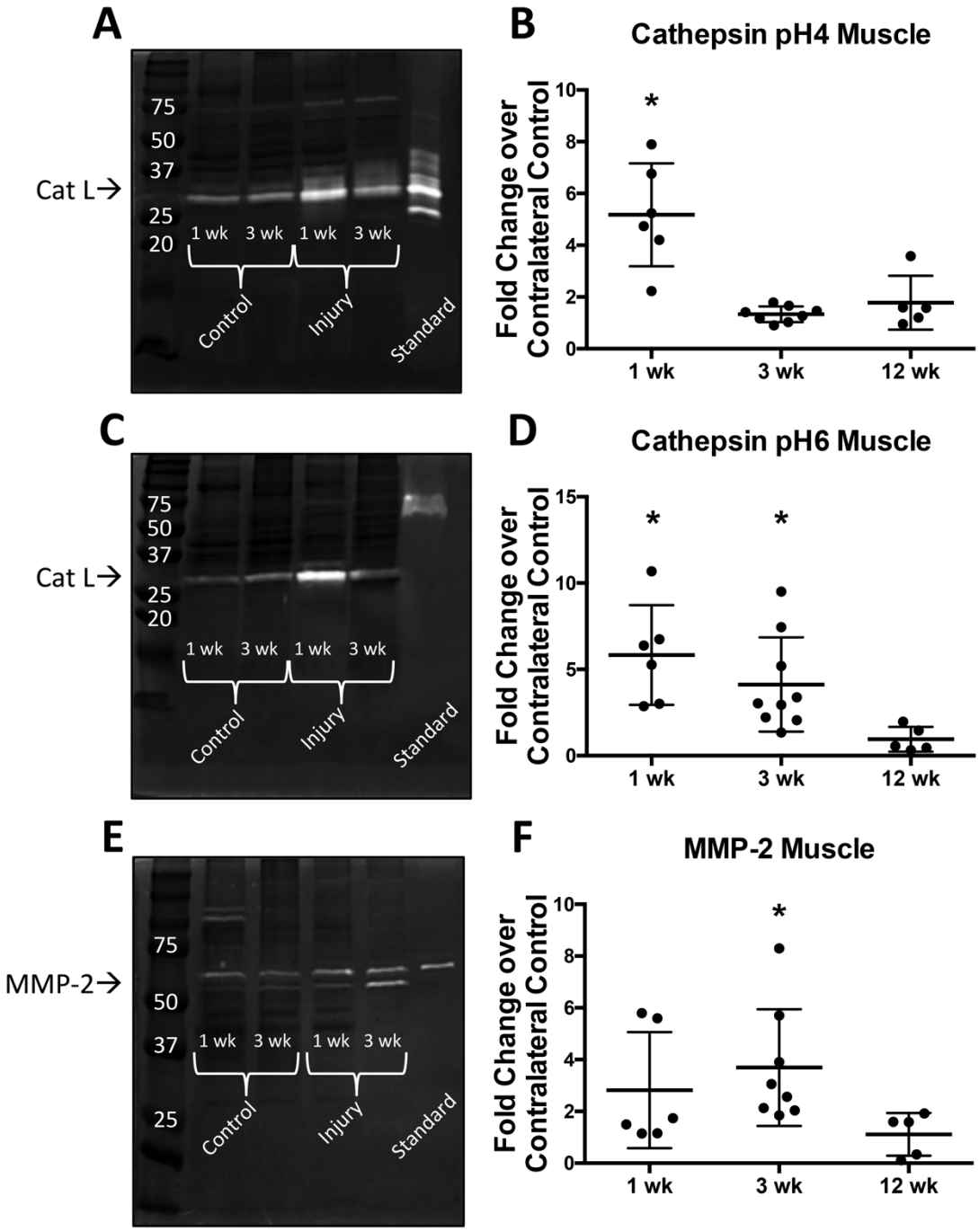

Figure 3.7: Gelatin zymography of muscle shows significant increase of proteases following injury. (A-B) cathepsin (pH=4 buffer) zymography gel and densitometry quantification (C-D) cathepsin (pH=6 buffer) zymography gel and densitometry quantification (E-F) MMP zymography gel and densitometry quantification. Recombinant protein used as standard: cathepsin L, cathepsin K, MMP-2 respectively. *$p<0.05$. N=6-8.

3.3.5 Active Cathepsins and MMPs in Humeral Head Cartilage

Following injury, active cathepsin L was found in pH4 cathepsin zymograms between 25 and 37 kDa (Figure 3.8a) at all three time points (1, 3, and 12 weeks), while active cathepsin K was found in pH6 cathepsin zymograms around 75 kDa (Figure 3.8c) at 1 week in cartilage (no cathepsin K was found at 3 or 12 week time points). Densitometric analysis revealed significantly higher active cathepsin L (3 fold difference) and active cathepsin K (6 fold difference) at 1 week following injury compared to control (Figure 3.8b and 3.8d). Active MMP-2 and MMP-9 were found at all three time points (1, 3, and 12 weeks) following injury at 50 to 75 kDa and 75 to 100 kDa respectively (Figure 3.8e). However, we detected no significant differences in the amount of active MMPs (Figure 3.8f and 3.8g). Due to limited sample availability and small sample size, we were unable to perform statistical analysis on 12 week cartilage samples. Bands with a molecular weight higher than 75 kDa were not analyzed due to the inability to correctly identify the protease associated with these bands. Additionally, we investigated the level of active proteases over time within humeral head cartilage (Figure 3.10g-j) and found no significant differences between 1 and 3 weeks for cathepsins or MMPs. Due to the small sample size for 12 week cartilage, we were unable to draw statistical comparisons with previous time points.

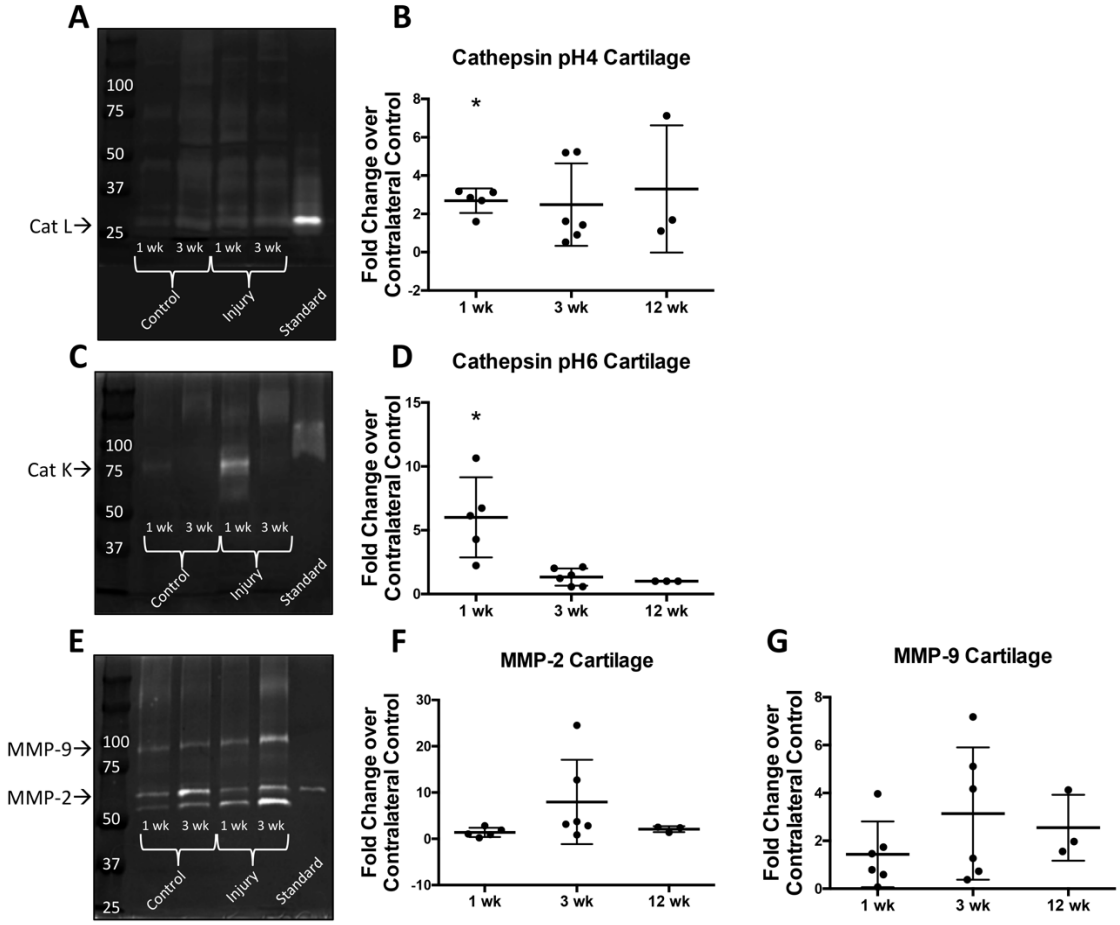

Figure 3.8: Gelatin zymography of cartilage shows significant increase of proteases following injury. (A-B) cathepsin (pH=4 buffer) zymography gel and densitometry quantification (C-D) cathepsin (pH=6 buffer) zymography gel and densitometry quantification (E-G) MMP zymography gel and densitometry quantification. Recombinant protein used as standard: cathepsin L, cathepsin K, MMP-2 respectively. *p<0.05. N=3. 12 week cartilage samples cannot be statistically analyzed due to low sample size.

3.3.6 Immunostaining for inflammatory cells

Staining for CD68+ and Ly6g+ cells indicated that both macrophages and neutrophils were present within supraspinatus tendon 1 week following injury (Figure 3.9). We found the average percentage of CD68+ cells were 24.1 ± 9.1% of all cells, while Ly6g+ cells were 31.0 ± 17.3% of all cells in injured supraspinatus tendon. Dissimilarly, control supraspinatus tendon had no CD68+ or Ly6g+ cells. Both

inflammatory cell types were seen within the proximal and distal regions of the supraspinatus tendon. Moreover, we found significantly more total cells within injured supraspinatus tendon with an average of 198 ± 54 cells per region of interest, while control supraspinatus tendon had an average of 103 ± 15 cells per region of interest.

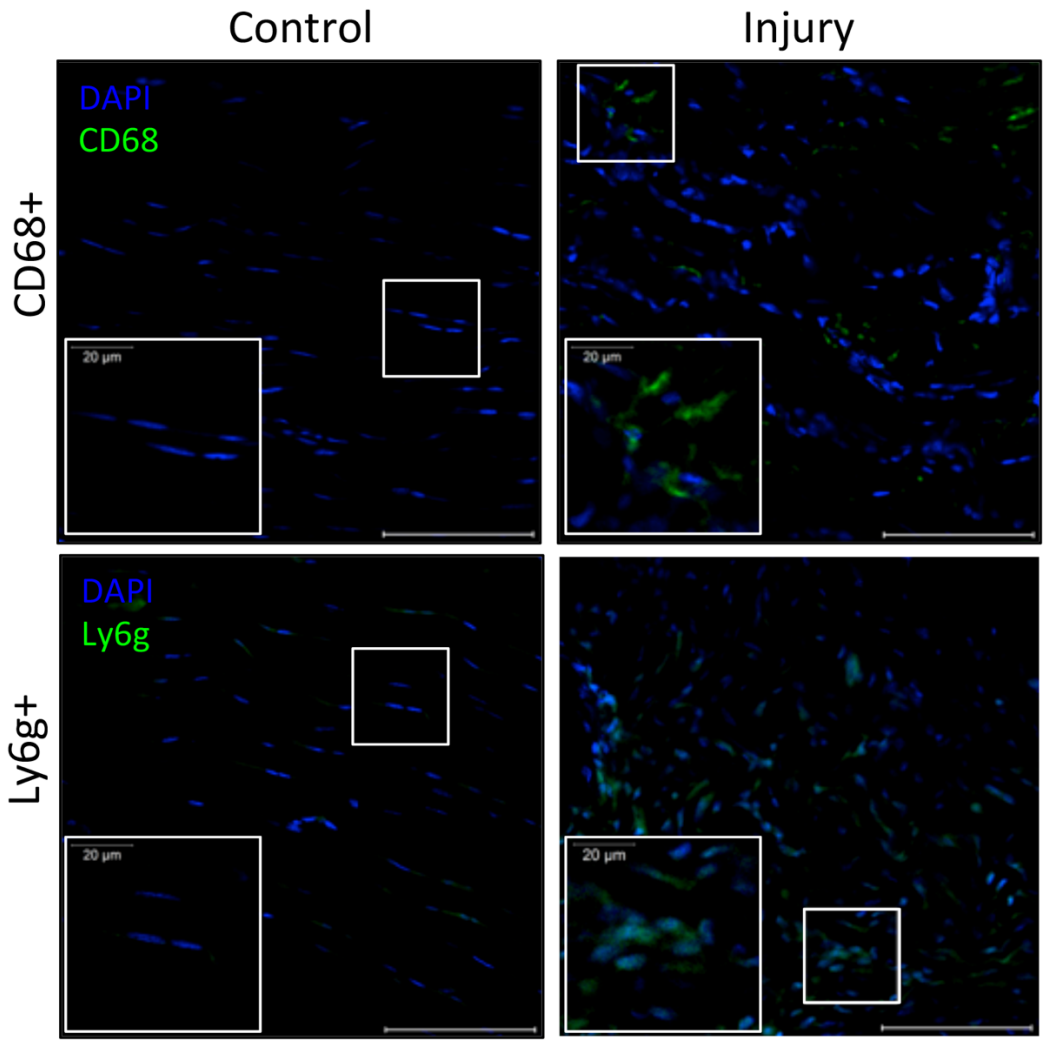

Figure 3.9: Immunostaining of tendon shows significantly higher prevalence of macrophage (CD68+) and neutrophil (Ly6g+) markers in injured tendon 1 week post-injury compared to uninjured control. Quantitative analysis via color thresholding demonstrated there was significantly more CD68+ cells in injured supraspinatus tendon (24.1 ± 9.1% of all cells) compared to 0% in control tendon ($p<0.05$). Additionally, there was significantly more Ly6g+ cells in injured supraspinatus tendon (31.0 ± 17.3% of all cells) compared to 0% in control supraspinatus tendon ($p<0.05$). DAPI used as nuclear stain. Image scale bar = 100 µm, insert scale bar = 20 µm.

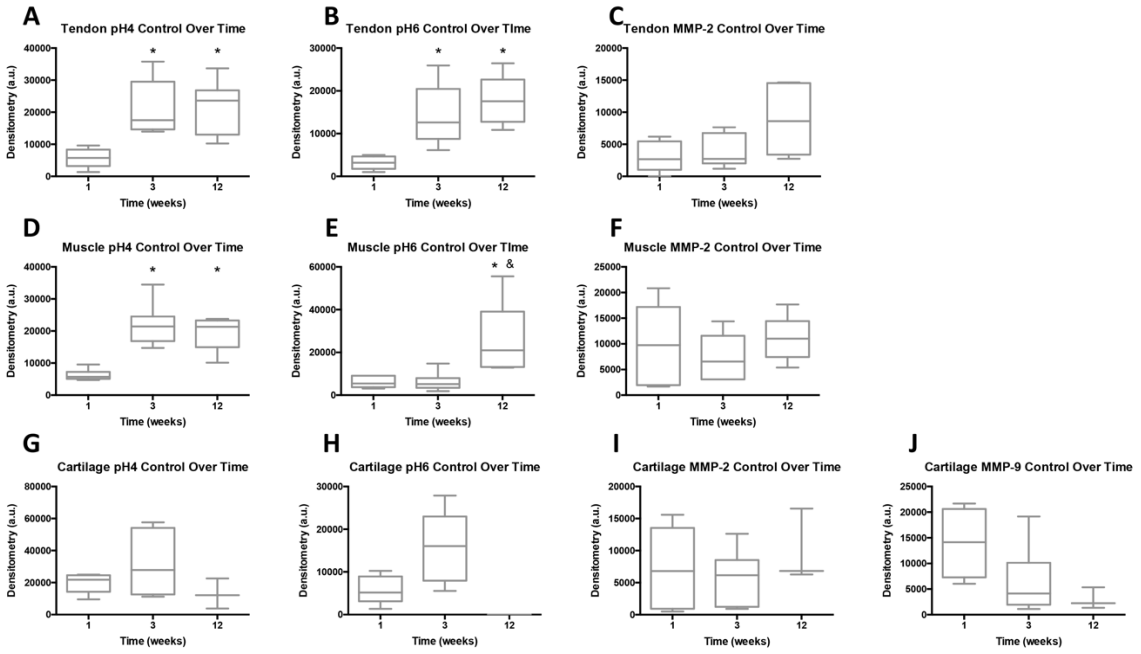

Figure 3.10: Analysis of basal levels of active proteases over time in control (uninjured) tissues. (A-C) Basal levels of cathepsin L and MMP-2 in supraspinatus tendon. N= 6-8. (D-F) Basal levels of cathepsin L and MMP-2 in supraspinatus muscle. N=6-8. (G-J) Basal levels of cathepsin L, cathepsin K, MMP-2, and MMP-9 in humeral head cartilage. N=3-6. *indicates significantly different from 1 week active protease levels ($p<0.05$). & indicates significantly different from 3 week active protease levels. 12 week cartilage samples cannot be statistically analyzed due to small sample size.

3.4 Discussion

This work employed an established animal model to replicate damage that has been observed in tendon, muscle, and humeral head cartilage following acute, full-thickness rotator cuff tear in humans [5,10,110,122,124]. As demonstrated in Figure 3.1, changes were observed in supraspinatus tendon morphology as early as 1 week, which was expected due to the transection of both the supraspinatus and infraspinatus tendons. Conversely, the supraspinatus muscle, which is not directly injured in this model, but suffers from secondary effects, such as lack of neural stimulation and mechanical loading, appeared comparable to control supraspinatus muscle at 1 week (Figure 3.2). However, our laboratory has previously shown significant fibrous infiltration of the

supraspinatus muscle in this animal model at 3 weeks post-injury [19] and maintenance of similar levels of fibrous tissue up to 6 weeks, which aligns with other groups using similar animal models of rotator cuff injuries [23,88].

Using contrast-enhanced EPIC–μCT, we were unable to detect any differences in cartilage volume, thickness, or attenuation 12 weeks following injury (Figure 3.4b). Prior work investigating denervation and tendon transection separately in a rat model has shown loss of safranin O staining in humeral head cartilage at 12 weeks [4], which should correspond to an increase in cartilage attenuation via EPIC-μCT [163,164]. However, because these results were found in a different injury model and employed a different technique, a direct comparison is limited. Additionally, we showed the presence of cartilage erosion (focal defects) within humeral head cartilage in half of all injured animals by 12 weeks. The lack of statistical difference in cartilage volume despite the presence of focal defects could be due to the fact that only half of the animals developed them, thus we would need a much larger sample size to demonstrate differences. Alternatively, it is possible the volume of cartilage lost as a focal defect was not large enough to render the overall volumes different between groups. Previous work examining humeral head cartilage following rotator cuff injury has demonstrated increased surface roughness and loss of tidemark integrity of humeral head cartilage 12 weeks post-injury in rats [4], but no indication of cartilage loss or erosion. However, contrast-enhanced μCT allows analysis of the entire humeral head and is a powerful tool to detect small defects in cartilage (Figure 3.3) that may be difficult to visualize through histological analysis [165]. A strong relationship between rotator cuff tear and subsequent degeneration of humeral head and glenoid cartilage has been seen in humans [5,73],

suggesting that this animal model at least partially recapitulates this aspect of human pathology.

Further μCT analysis revealed no differences in subchondral bone thickness, volume, or density as well as no differences in trabecular bone volume or density between control and injury groups at either time point. However, we found a significant increase in subchondral bone volume, thickness, and density between 1 and 12 weeks regardless of injury (Figure 3.5a-c). This is likely due to animal growth over time. Thus, it is possible that changes to subchondral bone properties caused by the injury were concealed by this normal growth. Nevertheless, we detected subchondral bone density increased directly beneath the focal defects 12 weeks following injury (Figure 3.5). Other studies have demonstrated overall bone loss in the humeral head of rats 12 weeks following transection of the supraspinatus and infraspinatus tendons followed by tendon reattachment [166]. These differences could be the result of differences in tendon injury vs. injury + repair models. Current methods for tendon reattachment in rodents, whereby a hole is drilled through the humeral head to allow suturing of the tendon, will intrinsically create bone loss. Previous findings show a correlation between chronic rotator cuff injuries presenting with cartilage loss and decreased bone density in humans [5], suggesting that this model does not fully recapitulate aspects of bone pathology at the time points studied. However, significantly denser subchondral bone directly under the focal cartilage defects was detected in our model. This aligns with previous literature investigating instances of osteoarthritis in the knee of humans in which an increase in bone mineral density is considered an early sign of osteoarthritis [167,168]. Combined with the presence of focal defects at 12 weeks, this model does appear to partially

replicate the increased risk of developing osteoarthritis following rotator cuff tear seen in humans [5].

Examining zymography results in each tissue, overall temporal protease activity profiles were different between cathepsins and MMP-2. Specifically, cathepsins were more active in the first week, while MMP-2 maintained prolonged activity in the supraspinatus tendon between 1 and 3 weeks and increased only at 3 weeks in supraspinatus muscle. These findings align with previous work showing cathepsins can activate MMPs [31] and could also indicate the possibility of cathepsins and MMP-2 sequentially acting on collagen to increase degradation [104]. Cathepsin L, present in both supraspinatus tendon and muscle in this work, is associated with protein turnover and tissue remodeling [108]. Cathepsin L has been shown to have the ability to cleave collagen I within the telopeptide region, which is involved in intra- and intermolecular bonds between collagen units [104]. Cathepsin L activity prior to MMP-2 activity would leave MMP-2 to cleave shorter collagen I molecules and enhance overall tissue degeneration. Similarly in cartilage, where no significant MMP-2 was detected, cathepsin K, which is typically associated with bone remodeling [169], has the ability to cleave type I collagen in its native triple helix at multiple locations [104], which would allow for significant degradation without the aid of MMP-2. Thus, the type of protease and the order of appearance could have a large effect on the degree of degeneration observed in each tissue.

As a part of this study, we also investigated basal levels of active proteases change over time in each tissue. Cathepsin pH4 zymograms of supraspinatus tendon and muscle, showed a significant increase in active cathepsin L from 1 week to 3 weeks with

no significant differences between 3 and 12 weeks, suggesting a plateau of active protease amounts after 3 weeks. In contrast, we did not observe any significant changes in the amounts of active MMP-2 over time in either of these tissues (Figure 3.10a-f), and no differences in active proteases over time in cartilage (Figure 3.10g-j). These findings are generally consistent with previous studies showing increased cathepsin activity in aged animals [170]. However, it should be noted that, in this work, we normalized the amount of active protease in the injured tissue to the uninjured contralateral control at each time point, therefore removing the confounding factor of age and time from the main comparisons in this work, which examined effect of injury.

In the supraspinatus muscle, significant upregulation of cathepsin L (associated with muscle atrophy in rats [110]) is observed at 1 week before obvious muscle fibrosis/atrophy could be observed at 3 weeks [19] (Figure 3.7). Furthermore in Figure 3.8, we see significant upregulation of active cathepsin K in cartilage at 1 week prior to visible damage at later time points (12 weeks). Thus, the onset of protease activity upregulation may not necessarily correlate with visible signs of damage. Previous findings have linked overactive proteases to degenerative damage because they were found simultaneously. For example, MMP-2 and -9 upregulation was detected in the presence of increasing muscle atrophy in rats [110,126]. Additionally, it was confirmed that cathepsin K concentration correlated to osteoarthritic severity in the knees of mice [158]. However, this work shows that proteases may be upregulated before the development of visible tissue damage and could be used as a potential biomarker to indicate risk for downstream damage. Additionally, this suggests that protease

upregulation, while brief, may have lasting effects on joint tissue and provides targets for early treatment to reduce tissue damage after traumatic injury to the shoulder.

By examining the temporal expression of proteases in multiple joint tissues simultaneously, this work begins to explore the biochemical relationship between acute damage to one tissue and eventual degradation of surrounding tissues. However, the cellular source of proteases has yet to be fully identified and are likely a combination of several tissue-resident cells, as well as cells recruited due to injury, as proteases released in one area can diffuse throughout the joint. Resident cells of the joint tissues, including tendon, muscle, cartilage, and synovium have all shown to be capable of producing proteases [63,110,131,158,171]. In addition to joint tissue cells, recruited inflammatory cells, such as macrophages and neutrophils, have the capacity to release proteases [67,68]. We have verified the presence of macrophages and neutrophils in the injured supraspinatus tendon in this animal model after 1 week (Figure 3.9) and have found increased levels of myloid cells, particularly macrophages, in the supraspinatus muscle at 1 week after acute tendon injury in previous work [19]. Further investigation of the cellular source of these enzymes would help better understand the causes of the varied protease profiles observed in this work.

Regardless, protease activity returned to baseline by 12 weeks following injury in both the supraspinatus tendon and supraspinatus muscle. This observation could be due to a general resolution of the acute inflammatory response over this time period. Prior work has shown inflammatory resolution is complete by 21 days following blunt dissection of Achilles tendon in rabbits [159]. In addition, this phenomenon could be caused, in part, by biological protease regulation, whereby proteases can both activate [112] and

cannibalize one another [132]. We have previously demonstrated cathepsin S has the ability to de-activate cathepsin K when present simultaneously [132]. Protease return to basal levels by 12 weeks also suggests their upregulation is a transient response to injury and that there may be a limited time window to prevent tissue degeneration through protease inhibition.

Inherent limitations of this study include the animal model chosen. Humans and rats have similar shoulder anatomies, but rats are quadruped animals and thus do not experience mechanical loading in the same way [94]. Additionally, while chosen due to the fact that this animal model developed shoulder joint damage similar to that seen in humans [5,10,110,122,124], this is an acute injury, which is not identical to how damage develops in humans in the clinical setting. A sham surgery control would have allowed the ability to distinguish how the surgery itself, which includes splitting the deltoid muscle to visualize the rotator cuff, can contribute to joint tissue degeneration. We did not investigate protease activity within the synovium or the presence of protease inhibitors over time following injury, although current findings indicate that this would be an interesting future study. Lastly, this study did not directly determine the biological cause of the visible tissue damage seen in the animal model of acute rotator cuff tear.

3.5 Conclusion

This work demonstrates that tissue degeneration occurs in supraspinatus tendon, supraspinatus muscle and humeral head cartilage after transection of the supra- and infraspinatus tendons in a rat model of full-thickness rotator cuff tear, and that there is significant protease upregulation in all three tissues, each with different temporal profiles. Interestingly, increased protease activity was found at early time points in all tissues

tested, even though only the tendon was injured directly. Both cathepsin L and MMP-2 activity were upregulated in supraspinatus tendon at 1 week in Figure 3.6, which coincided with visible damage. Conversely, supraspinatus muscle tissue experienced upregulated cathepsin L activity at 1 week with no obvious structural damage at this time point in Figure 3.7. Active cathepsin K and L were upregulated in cartilage 1 week after injury (Figure 3.8), and subsequent damage in the form of focal defects at 12 weeks following injury was found in ~half of all animals (Figure 3.4). A more comprehensive understanding of biochemical changes to joint tissue over time following rotator cuff tear will better inform ideal intervention times and treatments for each tissue. These results demonstrate concomitant degeneration in a number of rotator cuff tissues after traumatic injury and suggest that early intervention addressing multiple tissues simultaneously may be required to prevent joint degeneration after rotator cuff tear.

CHAPTER 4 DEVELOPMENT OF NOVEL MICROFLUIDIC DEVICE FOR UNIFORM MICROPARTICLE FABRICATION FOR RELEASE OF BROAD, SMALL MOLECULE CATHEPSIN INHIBITOR, E-64

4.1 Introduction

Cathepsins are a cysteine-family of proteases responsible for a variety of homeostatic functions throughout the body including extracellular matrix remodeling, bone resorption, and intracellular protein turnover [11]. However, upregulated cathepsins have been implicated in a variety of degenerative diseases, including atrophy of the tibialis anterior muscle [12], osteoarthritis of the knee [13], and tendinopathy [14,15]. Several clinical trials have investigated systemic delivery of cathepsin inhibitors as therapeutic treatments to reduce and halt tissue degeneration. However, systemic delivery results in healthy and diseased tissues experiencing equal exposure to the protease inhibitor treatment, which may prevent regulated proteases from performing their normal functions. Additionally, systemic delivery requires a very high amount of therapeutic molecules in order to achieve a detectable effect in the diseased tissue, which will only receive a small fraction of the initial dose [18]. Presently, all clinical trials utilizing cathepsin protease inhibitors have been abandoned due to severe side effects including headache, gastrointestinal disturbance, lung fibrosis, and skin lesions [16]. These severe effects are likely caused by inhibition of regulated cathepsins in healthy tissues.

An alternative strategy to systemic delivery is employing the use of a biomaterial vehicle for localized delivery of inhibitor therapeutics to the site of disease or injury.

Microparticles are advantageous biomaterial vehicles because they are injectable, have the capacity to deliver a large quantity therapeutic drugs due to the high surface area to volume ratio, can be directly injected into the diseased tissue, and require substantially less drug compared to systemic delivery [18]. For example, mice suffering with sickle cell anemia were treated with daily systemic injection of E-64 at a concentration of 5 mg/kg (~ 125 μg) [25], while our animal model of rotator cuff tear characterized in chapter 3 (Aim 1) would only require 4 μg of E-64 to achieve a 1:1 molar ratio with cathepsin L 7 days after injury. Additionally, our microparticle delivery platform would not require daily injections if microparticles are designed for sustained release of E-64.

Our laboratory has extensively used microparticles for localized therapeutic delivery. For example, our group has previously shown a significant increase in the recruitment of anti-inflammatory cells in the supraspinatus muscle following injection of SDF-1α loaded microparticles in our rat model of rotator cuff tear [19]. Furthermore, our group previously used microparticles for localized delivery in an animal model of osteoarthritis [20]. We injected TSG-6 loaded microparticles into the joint space of the knee in a rat model of osteoarthritis and found significantly reduced cartilage degeneration following injury compared to soluble TSG-6 injections [20]. Additionally, the Botchwey laboratory has previously injected poly(DL-lactic-co-glycolic acid) (PLGA) microparticles for sustained release of small molecule FTY720 [172]. FTY720 has been shown to recruit monocytes and stimulate wound healing [172]. They found that injection of FTY720-loaded PLGA microparticles into the supraspinatus muscle of a mouse model of rotator cuff tear resulted in decreased levels of supraspinatus muscle atrophy compared to unloaded PLGA microparticles [172]. Another group encapsulated

BMP-2 in alginate and PLGA microparticles to enhance bone regeneration [173]. They found significantly more new bone formation following BMP-2 loaded PLGA treatment compared to no treatment and BMP-2 release from a collagen–hydroxyapatite scaffold (accepted gold standard of treatment) [173]. Thus, localized delivery of therapeutic molecules via microparticle carrier has the potential to treat diseases and reduce severe side effects that have been seen in systemic delivery.

There are many methods to fabricate microparticles for localized treatment, but microfluidic devices are becoming increasingly popular due to their distinct advantages. Advantages of using a microfluidic device platform include: fabrication of uniformly sized microparticles in a wide range of sizes [156], the ability to convert the entire polymer solution into microparticles, and the ability to incorporate additional biomolecules into the microparticle network. Taken together, fabricating microparticles with a microfluidic device reduces material waste, has a reduced number of fabrication steps, and reduces waste of potentially expensive therapeutics used for microparticle release.

To fabricate microparticles with a microfluidic device two immiscible phases are used: the continuous phase and the discontinuous phases [26]. In a water-in-oil system, the continuous phase would consist of oil and the discontinuous phase would consist of the water soluble polymer solution. Microparticle size can be tuned by adjusting several parameters including continuous phase speed, discontinuous phase speed, and surfactant concentration. Previous work has shown that higher phase speeds cause increased shear stress on the microparticle droplet [26]. The increased shear stress causes more frequent discontinuous phase stream break-up and consequently generates smaller microparticles

[26]. When the microparticle droplet is smaller than the outlet, the force applied is negligible [26]. However, as the discontinuous phase is continuously injected via the syringe pump, the microparticle droplet will increase in size and the applied force will similarly increase [26]. The increased force on the microparticle droplet causes it to be pinched off from the tip of the needle [26]. Furthermore, microparticle size can be tuned by the amount of surfactant used in the system. It has previously been shown that particle size decreases with increasing amounts of surfactants [28]. Microfluidic devices that utilize immiscible phases to fabricate microparticles use surfactants to stabilize the shape of the microparticles and prevent coalescence of microparticles, which also ensures a smaller microparticle size [27].

E-64 (trans-Epoxysuccinyl-L-leucylamido(4-guanidino)butane) is a small molecule, broad inhibitor of the cysteine cathepsin family of proteases [39]. E-64 is the small molecule analog of the endogenous cysteine cathepsin inhibitor, cystatin C [38]. E-64 has been shown to irreversibly bind cathepsins L, S, and K [39,40]. A previous study tested daily systemic injections of E-64 in a mouse model of sickle cell anemia, which develops characteristic osteoporosis caused by chronic upregulation of cathepsin K [25]. They found that treatment with E-64 improved trabecular bone density and mechanical properties of femurs compared to mice with untreated sickle cell anemia [25]. At present, therapeutic use of E-64 has been limited to soluble injections due to the inability to quantify E-64 in solution, which would be required for *in vitro* testing with a biomaterial carrier.

Our laboratory and others have previously used poly(ethylene glycol) diacrylate (PEGDA) based microparticles for delivery of therapeutic drugs and proteins [19,20].

PEGDA is attractive polymer that is commonly used in biomaterial applications because it is hydrophilic and can be tailored to achieve controlled release over a variety of timescales through changing polymer network properties and drug loading [139]. Previously in our laboratory, we have covalently attached dithiothreitol (DTT) to PEGDA to increase the susceptibility of the resulting ester bond for hydrolytic degradation [142]. Previous work has demonstrated that microparticle degradation rate is proportional to DTT levels and inversely proportional to polymer weight percentage (wt%) of the microparticle network [143]. It has been shown that slower degradation can result in therapeutic release over a longer period of time or an increase in total therapeutic released over time [134,143]. Similarly, increased polymer weight percentage in the microparticle formulation creates a smaller mesh size, which can delay release of the loaded therapeutic and generate sustained release over time [134]. Lastly, it has been shown that loading larger amounts of therapeutic drugs into biomaterials can cause an increase in overall release [134].

Given the perceived gap in sustained release capability for cathepsin inhibitors, the first ***objective*** of this aim was to develop and characterize a microfluidic device to fabricate uniformly sized PEGDA microparticle carriers. We characterized microparticle size, degradation time, and ability to incorporate biomolecules. To characterize range of microparticle size that could be achieved with our novel microfluidic device, we varied several parameters including continuous phase speed, discontinuous phase speed, and surfactant concentration in the continuous phase. To characterize microparticle degradation, we varied polymer weight percent and amount of DTT incorporated into the network. To determine if our microfluidic device had the ability to incorporate additional

biomolecules into the polymer network, we added fluorescently tagged heparin (as a model biomolecule) to the discontinuous phase prior to microparticle fabrication. We ***hypothesized*** that microparticle size would be inversely proportional to the speed of both the continuous and discontinuous phases. Additionally, we hypothesized that 40% span-80 would yield significantly smaller microparticles compared to 20% span-80 with any given set parameters. Furthermore, we hypothesized that decreased polymer weight percentage and increased DTT concentration would result in faster degradation of microparticles over time. Decreased polymer weight percentage would require the fewest number of degradation events to achieve degradation [29] and the incorporation of increased amounts of DTT has been shown to increase the rate of hydrolytic degradation [143]. Lastly, we ***hypothesized*** that the addition of heparin into the discontinuous phase of our microfluidic device would result in incorporation of heparin into our PEGDA microparticles.

The second ***objective*** of this aim was to characterize release of E-64 from microparticles. E-64 is a broad, small molecule cathepsin inhibitor and was used as a model therapeutic for this aim. In order to understand how our microparticle system could tune E-64 release, we varied several parameters including: initial amount of E-64 loaded into the discontinuous phase, polymer weight percent, and amount of DTT incorporated into the network. Setting up a matrix of conditions to test the release of E-64 will allow us to choose a set of parameters to use in our rat model of rotator cuff tear in chapter 5 (Aim 3). We ***hypothesized*** that E-64 release over 14 days could be tuned based on the aforementioned parameters. Specifically, we hypothesized that increased polymer weight percent would cause delayed diffusion of E-64 from microparticles and result in a

significant decrease in total E-64 released over 14 days. We hypothesized that increased DTT concentration would result in faster diffusion of E-64 out of microparticles due to larger spacing between polymer chains and result in overall greater amount of E-64 released over 14 days. Lastly, we hypothesized that a greater initial loading of E-64 into the discontinuous phase would produce microparticles with a higher amount of E-64 and result in significantly more E-64 released over 14 days.

4.2 Materials and Methods

4.2.1 Poly(ethylene glycol) diacrylate (PEGDA) Synthesis and Characterization

A 1:8 molar ratio of 3.4 kDa poly(ethylene glycol) (Sigma) to acryloyl chloride (AcCl, Sigma) was reacted in dichloromethane (DCM) solution as described previously [142]. Next, triethylamine (TEA, Sigma) was used as a catalyst to yield linear PEGDA by its addition in a dropwise fashion into a solution composed of a 1:1 molar ratio of TEA to AcCl. To determine the degree of PEGDA functionalization (number of acrylate groups), we performed proton nuclear magnetic resonance (^{1}H NMR). PEGDA was reconstituted in deuterated H_2O (Sigma) at a concentration of 10 mg/mL and run on a Bruker Avance III spectrometer at 400 Hz and analyzed using iNMR software as described previously [20,153].

4.2.2 Microfluidic Device and Microparticle Sizing[2]

To construct the microfluidic device, a 30-gauge needle (BD) was bent at a 45° angle and was pierced through miniature ethylene-vinyl acetate (EVA) tubing (McMaster) such that the bent portion was parallel to the EVA tubing wall. We cut off the cap of a 1.7 mL microcentrifuge tube and using a razor blade cut out three areas to fit the EVA tubing and the 30-gauge needle. The device was sealed with epoxy resin (Sigma) to cover holes and prevent leaking. A schematic of our microfluidic device set up can be seen in the insert within Figure 4.1.

The continuous phase consisted of mineral oil (VWR) and span-80 (Sigma). The discontinuous phase consisted of PEGDA, DTT (Sigma), and L0290 photoinitiator (TCI). The L0290 photoinitiator was dissolved in phosphate buffered saline (PBS, Fisher) to a final concentration of 20 mg/mL. PEGDA and DTT were resuspended in L0290 photoinitiator and allowed to incubate at 37 °C for 30 minutes in the absence of light to allow for Michael Type addition crosslinking. Following this incubation, E-64 (Sigma) was added to the polymer solution and incubated at 37 °C in the absence of light for an additional 30 minutes. The polymer solution was loaded into a 1 mL syringe (Hamilton) and covered in foil to prevent light exposure and premature crosslinking.

The discontinuous phase was injected into the EVA tubing via 30-gauge needle. Both the continuous and discontinuous phases were injected into the microfluidic device

---

[2] This protocol was developed with the Xia laboratory and was based on previously published work: Choi SW, Cheong IW, Kim JH, Xia Y. Preparation of uniform microspheres using a simple fluidic device and their crystallization into close-packed lattices. Small. 2009 Feb 20;5(4):454-9.

via syringe pumps as can be seen in Figure 4.1. The EVA tubing was coiled under an ultraviolet (UV) lamp to allow the microparticles to crosslink, which is also labeled in Figure 4.1. To certify uniform crosslinking between trials, we ensured that the center of the coiled tubed registered a minimum intensity of 15 mW/cm^2. The EVA tubing emptied into a 50 mL conical tube for microparticle collection.

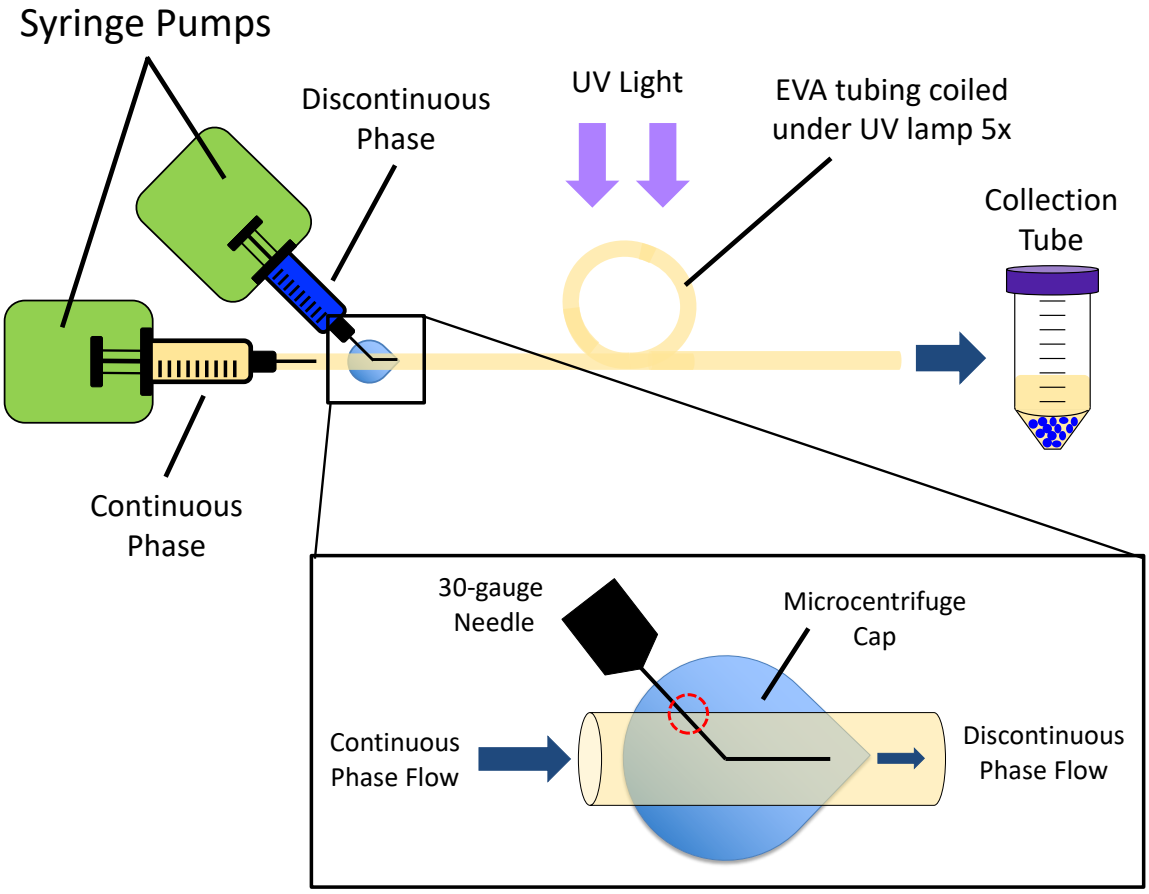

Figure 4.1: The benchtop set up of our novel microfluidic device platform. The discontinuous phase and continuous phase are injected into the microfluidic device via syringe pumps. The insert demonstrates how the microfluidic device is constructed. The 30-gauge needle is bent at 45 ° and inserted into the EVA tubing. The red dotted line indicates the puncture area that is sealed with epoxy resin to prevent leaking. The EVA tubing is coiled under the UV light source to ensure microparticle crosslinking and to reduce counter space. The EVA tubing empties into a 50 mL conical tube, where the microparticle are collected.

Once the discontinuous phase was spent, the collected microparticles were centrifuged at 2,000 xg for 5 minutes to force all microparticles to the bottom of the conical tube. The majority of the mineral oil and span-80 solution was removed with a serological pipette ensuring that the microparticle pellet was not disturbed. The microparticles were washed two times with pure mineral oil and gentle vortexing followed by centrifugation of 2,000 xg for 5 minutes. Lastly, microparticles were washed and resuspended in PBS.

To determine the range of microparticle size that could be achieved with our microfluidic device, several parameter ranges were tested. The continuous phase speed was varied from 100 – 500 μL/min, while the discontinuous speed was varied from 1 – 5 μL/min. Additionally, the amount of span-80 was tested at 20% and 40% of the discontinuous phase volume with all speed variables. Microparticles were imaged using light microscopy (Nikon TE2000) and sizing was determined using the measure plug in within ImageJ (NIH).

4.2.3 Fabrication of Microparticles with Fluorescently-Tagged Heparin

Heparin was functionalized with methacrylamide (Hep-MAm) in order to allow covalent crosslinking into the microparticle as described previously [37]. Briefly, 200 mg of heparin sodium salt from porcine intestinal mucosa (Millipore-Sigma) was resuspended in 10 mL of phosphate buffer (40 mg Na_2HPO_4 and 4.5 g NaH_2PO_4 in 100 mL dH_2O) under constant stirring with a stir bar and stir plate. After heparin dissolved into solution, 180 mg of sulfo-NHS (Millipore-Sigma) and 180 mg of APMam (Polysciences Inc.) were added to the heparin solution. After the sulfo-NHS and APMam

dissolved in solution, 150 mg EDC was added to the solution and the reaction was placed on ice under constant stirring. We allowed the reaction to proceed for 2 hours before adding another 150 mg of EDC to the heparin solution. After another 4 hours, the Hep-MAm was dialyzed (Spectrum Labs) for two days, freeze dried (Labconco), and stored at -20 °C until use.

Hep-MAm was fluorescently tagged with AlexaFluor633 (AF633, Invitrogen) in order to visualize glycosaminoglycan distribution within microparticles fabricated with our novel microfluidic device. Hep-MAm was dissolved in 0.1 M Na_2HPO_4 solution (pH = 6) at a10 mg/mL concentration and reacted with 10 mM EDC and 5.7 μM AF633 at room temperature for 90 minutes. Fluorescently tagged Hep-MAm (Hep-MAm-AF633) was subsequently dialyzed for two days, freeze dried, and stored at -20 °C using the same protocol as described above.

For microparticle fabrication with our novel microfluidic device PEGDA and DTT were first resuspended in L0290 photoinitiator and allowed to incubate at 37 °C for 30 minutes in the absence of light. Following this incubation, Hep-MAm-AF633 was added to the polymer solution and incubated at 37 °C in the absence of light for an additional 30 minutes. The microfluidic device was run as previously described in Section 4.3.1. PEGDA based Hep-MAm-AF633 microparticles were imaged using confocal microscopy (Zeiss 700).

4.2.4 Microparticle Degradation

To assess degradation of microparticles fabricated with our novel microfluidic device we tested the following formulations: 10 wt% 5 mM DTT, 10 wt% 10 mM DTT,

20 wt% 5 mM DTT, and 20 wt% 10 mM DTT. We placed the microparticles of each formulation (N=3) in 1.7 mL low-binding tubes at 37 °C under constant agitation. At each degradation test time point the microparticles were vortexed thoroughly to ensure adequate mixing and 20 μL of solution containing microparticles was taken and pipetted onto a microscope glass side and covered with coverslip to slow evaporation of water during imaging. The presence of microparticles was observed and captured using light microscopy (Nikon TE2000). The solution used for imaging was replaced with an equal volume of PBS at each time point.

4.2.5 Fluorogenic Substrate Assay: Z-FR-AMC and Cathepsin L

To assess inhibitory capacity for cathepsin L, recombinant cathepsin L (R&D Systems) was used with Z-FR-AMC Fluorogenic Peptide Substrate Assay (R&D Systems). Preparation of reagents was performed according to manufacturer guidelines. To assess percent inhibition the following was prepared in a 96 well plate: 100 μL of undiluted E-64 microparticle supernatant (N=3-4), 20 μL of Z-LR-AMC stock, and 100 μL of cathepsin L (concentration: 50 ng/mL) in reaction buffer. The positive control included 100 μL of PBS (the E-64 microparticle solution), 100 μL of cathepsin L in reaction buffer, and 20 μL Z-LR-AMC. The blank for the solution consisted of 100 μL reaction buffer (no cathepsin L), 100 μL PBS, and 20 μL Z-LR-AMC stock. The cathepsin L solution was added once all standard and sample wells were prepared because it is a continuous (non-terminal) assay. Per manufacturer guidelines, samples were incubated at room temperature for 1 hour prior to reading on a fluorescent plate reader at 380/460nm.

4.2.6 Fluorogenic Substrate Assay: DQ Gelatin and Cathepsin K

To assess inhibitory capacity for cathepsin K, recombinant cathepsin K (Enzo) was used with a DQ Gelatin Fluorogenic Substrate Assay (Thermo). Preparation of reagents was performed according to manufacturer guidelines. To assess percent inhibition the following was prepared in a 96 well plate: 100 μL of undiluted E-64 microparticle supernatant (N=3-4), 20 μL of DQ gelatin stock, and 100 μL of cathepsin K (concentration: 1.3 μg/mL) in reaction buffer. The positive control included 100 μL of phosphate buffer saline (the E-64 microparticle solution), 100 μL of cathepsin K diluted in reaction buffer, and 20 μL DQ gelatin. The blank for the solution consisted of 100 μL reaction buffer (no cathepsin K), 100 μL PBS, and 20 μL DQ gelatin stock. The cathepsin K solution was added once all standard and sample wells were prepared because it is a continuous (non-terminal) assay. Per manufacturer guidelines, samples were incubated at room temperature for 1 hour prior to reading on a fluorescent plate reader at 495/515 nm.

To determine E-64 release, a standard curve of known amounts of E-64 was tested concurrently with supernatant samples and analyzed by fitting a one-phase decay line (Prism). Previous work in the Platt laboratory has demonstrated that a minimum of 5 picomoles of cathepsin K per well is required to obtain an adequate signal on the DQ gelatin assay [132]. Thus, the E-64 standard curve tested varying molar ratios of E-64 to cathepsin K, including: 1:20, 1:10, 1:5, 1:1, 2:1, 5:1, 10:1, and 20:1. Samples calculated to be outside of the standard curve range when testing for inhibition were subsequently diluted and rerun to calculate release. For the purposes of testing the standard curve boundaries we also tested the following ratios of E-64 to Cathepsin K: 100:1, 200:1, 500:1, and 1,000:1.

4.2.7 Fluorogenic Substrate Assay: Inhibition and Interference Assay

To test the limits of the redesigned DQ gelatin Fluorogenic Substrate Assay, we tested the ability of each microparticle component and continuous phase component to individually inhibit cathepsin K. The microparticle components tested include PEGDA, DTT, and L0290. The amount of each component was calculated based on the makeup of the discontinuous phase used to make microparticles. Thus, we used the same amount of each component that would be present in solution if we could instantaneously degrade a single batch of microparticles. Additionally, we tested diluted amounts of mineral oil and span-80 to replicate poor washing. For the inhibition test, each component was treated identically to supernatant samples. The positive control included 100 μL of PBS, 100 μL of cathepsin K diluted in reaction buffer, and 20 μL DQ gelatin. The blank for the solution consisted of 100 μL reaction buffer (no cathepsin K), 100 μL PBS, and 20 μL DQ gelatin stock. The cathepsin K was added to each well at the same time because it is a continuous (non-terminal) assay. Per manufacturer guidelines, samples were incubated at room temperature for 1 hour prior to reading on a fluorescent plate reader at 495/515 nm.

To distinguish whether the tested components were in fact inhibiting cathepsin K or potentially interfering with the assay, we conducted an interference assay. For this particular test each well first added DQ gelatin and cathepsin K in reaction buffer to each well. We allowed the reaction to proceed for 30 minutes at room temperature protected from light. After imaging the plate (495/515 nm) to establish baseline, we added the components to their respective test wells and immediately read the plate again to determine interference. The positive control wells were given an equal amount of PBS at the same time components were added to test wells.

4.2.8 E-64 Bioactivity and Release from Microparticles

To assess release of E-64 from loaded microparticles, the microparticles were placed in 1.7 mL low-binding microcentrifuge tubes with a total volume of 0.5 mL on rotor at 37 °C. At Days 1, 2, 3, 5, 7, 10, and 14 the E-64 loaded microparticles were centrifuged and the supernatant was removed and frozen at -20 °C. An equal volume of PBS with calcium and magnesium ions replaced the supernatant volume at each time point. The supernatant bioactivity was tested with both cathepsin L and K as described in methods 4.4.2. Example calculations for E-64 release can be found in Appendix B.

4.2.9 Statistical Analysis

To assess microparticle size as a function of continuous phase speed, discontinuous phase speed, and span-80 content we used a non-parametric ANOVA test and the Kruskal-Wallis post-hoc test ($p \leq 0.05$) in GraphPad. For analysis of microfluidic device component inhibition on cathepsin K in the DQ gelatin fluorogenic substrate assay we performed a one-way ANOVA and Tukey's post-hoc test ($p \leq 0.05$) in GraphPad. For analysis of microfluidic device component interference with the DQ gelatin fluorogenic substrate assay we performed a two-way repeated measures ANOVA and Tukey's post-hoc test ($p \leq 0.05$) in GraphPad. For analysis of percent inhibition of unloaded microparticles vs E-64 loaded microparticles we performed two-way repeated measures ANOVA and Tukey's post-hoc test ($p \leq 0.05$) in GraphPad.

4.3 Results

4.3.1 PEGDA Characterization

The ^{1}H NMR analysis demonstrated that the batch of PEGDA used in this body of work was ~55% functionalized.

4.3.2 Microfluidic Device Size Characterization

A detailed schematic of the microfluidic device can be seen in Figure 4.1 and 4.2a. Analysis of microparticle size showed that our microfluidic device could synthesize PEGDA microparticles ranging from approximately 25 to 400 μm (Figure 4.2d and 4.2e). In alignment with our hypothesis, we saw that microparticle size was inversely proportional to both the continuous and discontinuous phase speeds (Figure 2d and 2e). Interestingly, 40% span-80 yielded significantly smaller microparticles compared to 20% span-80 at a single speed (Figure 2d). The parameters ultimately chosen for E-64 release studies (discontinuous phase speed: 3 μL/min, continuous phase speed: 500 μL/min, and 40% span-80) resulted in uniform size distribution of microparticles as seen in Figure 4.2b with an average size of 69.6 ± 16.7 μm and a polydispersity index of 0.25.

In terms of biomolecule incorporation, we added fluorescently labeled heparin (Hep-Mam-AF633) to the discontinuous phase prior to fabricating microparticles with our microfluidic device. We imaged the resulting microparticles with confocal microscopy. We detected fluorescently labeled heparin (Hep-Mam-AF633) within all microparticles fabricated with our novel microfluidic device as seen in Figure 4.2c.

4.3.3 Microparticle Degradation

Microparticles were tested for degradation periodically over 77 Days (11 weeks) as seen in Figure 4.3. We found that only the 10 wt% 10 mM microparticles had completely degraded by Day 77, while all other formulations (10 wt% 5 mM DTT, 20 wt% 5 mM DTT, and 20 wt% 10 mM DTT) had not.

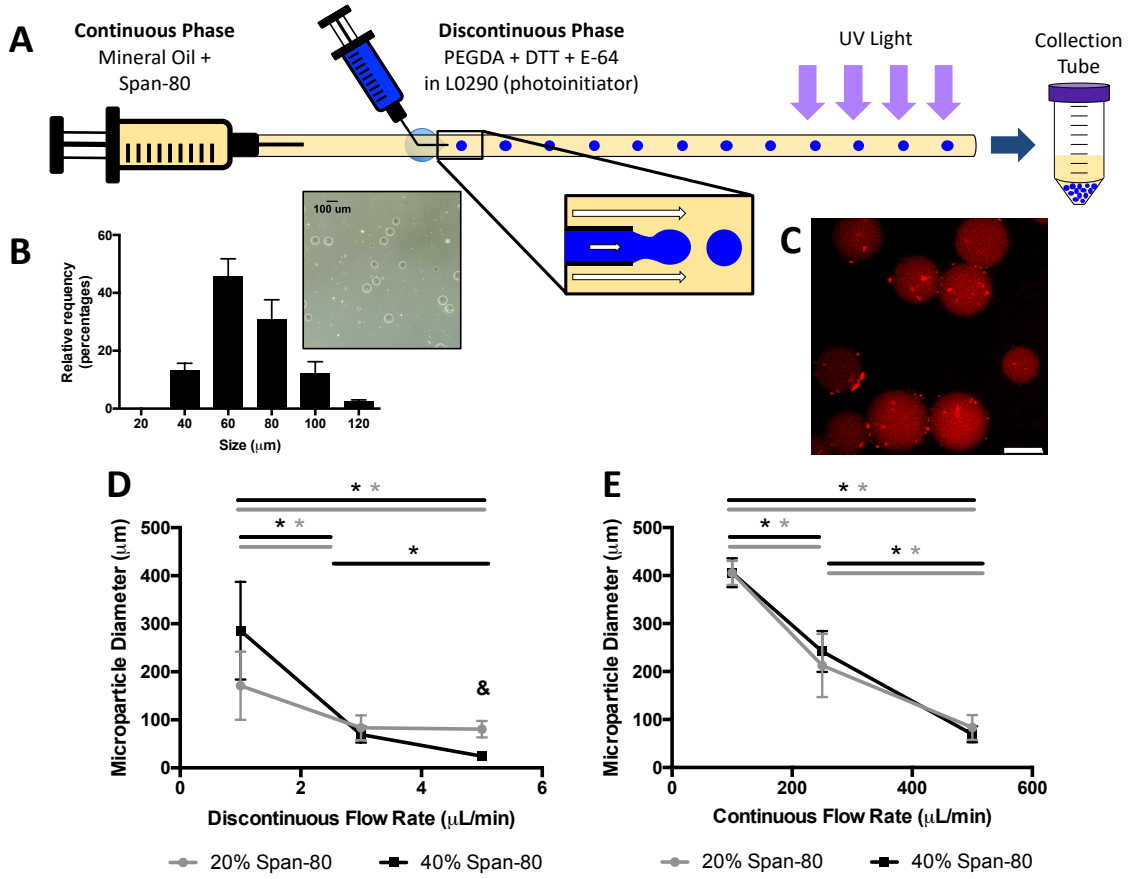

Figure 4.2: Microfluidic device schematic and characterization. (A) Schematic of our novel microfluidic device. (B) Histogram of microparticles synthesized with continuous phase speed of 500 μL/min and discontinuous phase speed of 3 μL/min with 40% span-80. Phase contrast image of PEGDA microparticles. Scale bar = 100 μm. N=3 microparticle batches. (C) PEGDA microparticles fabricated with fluorescently tagged heparin (AlexaFluor633-Hep-MAm). Scale bar = 100 μm. (D) Plot of microparticle diameter as a function of the discontinuous phase flow rate. The continuous flow rate was kept at 500 μL/min. N=3 microparticle batches. Error bars = standard deviation. (E) Plot of microparticle diameter as a function of the continuous phase flow rate with 20 and 40% span-80. The discontinuous flow rate was kept at 3 μL/min. N=3 microparticle batches. Error bars = standard deviation. *$p<0.05$ = significantly different microparticle size compared to other speed with the same span-80 concentration. &$p<0.05$ = significantly different microparticle size compared to other span-80 concentration at the same speed.

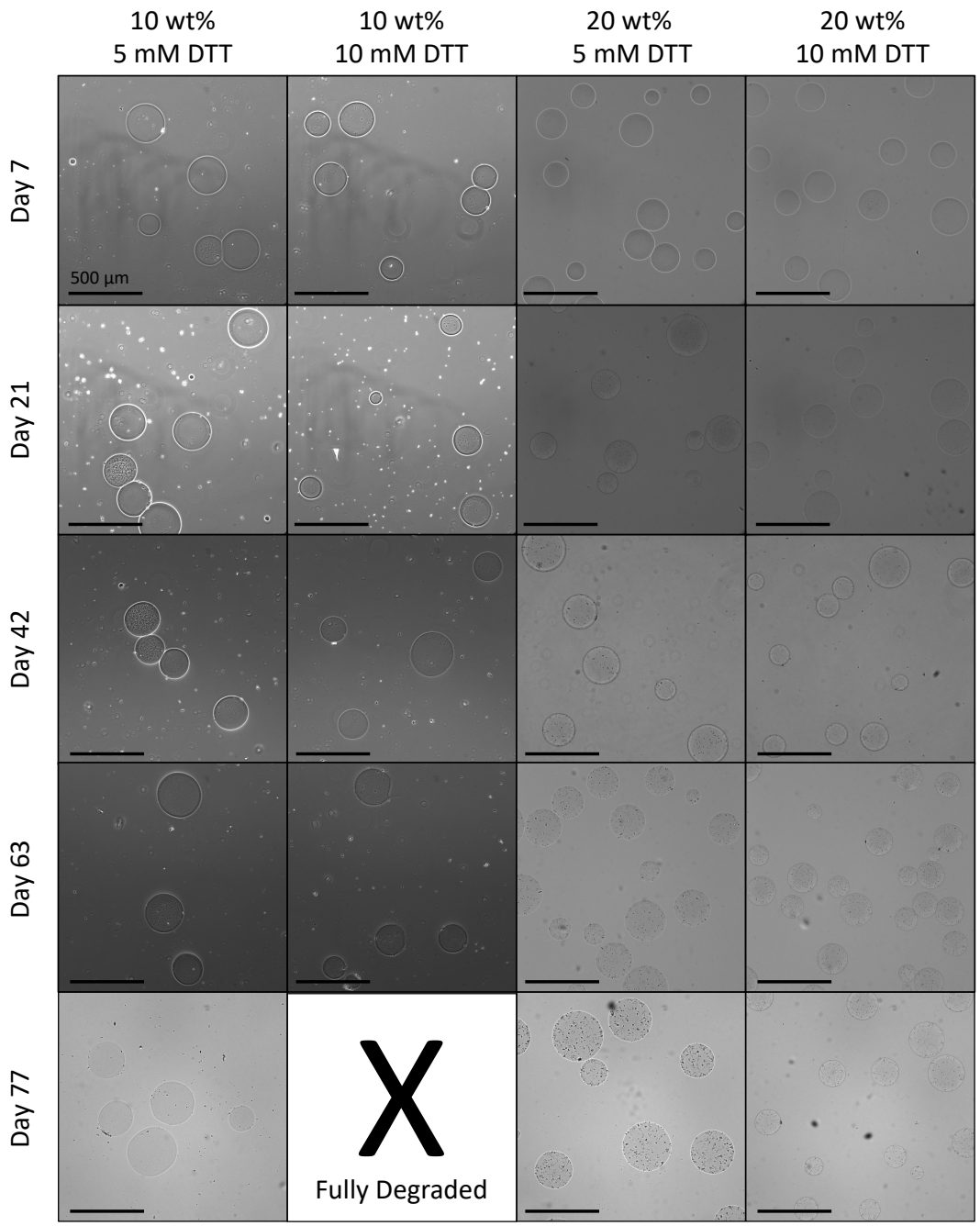

Figure 4.3: Microparticles fabricated with our novel microfluidic device can be made to be fully degradable. Variable parameters tested include polymer weight percent (wt%) and dithiothreitol (DTT) concentration (mM). We found 10 wt% 5 mM DTT, 20 wt% 5 mM DTT, and 20 wt% 10 mM DTT microparticles did not fully degrade by Day 77. We found 10 wt% 10 mM DTT fully degraded by Day 77. N= 3. Scale bar = 500 µm.

4.3.4 E-64 Standard Curve with Cathepsin K and Cathepsin L

We tested a standard curve of known amounts of E-64 on the DQ gelatin (cathepsin K) and Z-FR-AMC (cathepsin L) fluorogenic substrate assays. We found that cathepsin K and the DQ gelatin fluorogenic substrate assay generate an E-64 standard curve that can be fit to a one-phase decay trend line (Figure 4.4). Conversely, cathepsin L and the Z-FR-AMC fluorogenic substrate assay did not generate an E-64 standard curve that could be fit to a trend line (Figure 4.4). Thus, the DQ gelatin assay with cathepsin K was chosen to calculate E-64 release in subsequent experiments. While the entire standard curve shown below was used to find the one-phase decay equation, only samples with a fluorescent intensity reading at or above the standard curve value for 500 ng/mL were used to calculate release. Thus, if the cathepsin K activity signal was too high for a particular value, the sample was rerun at a higher dilution.

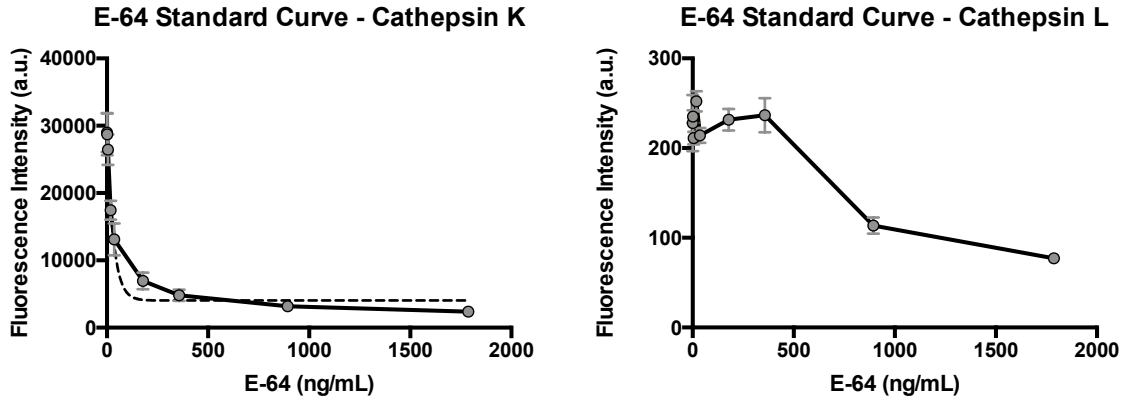

Figure 4.4: DQ gelatin and Z-FR-AMC fluorogenic substrate assays yield different E-64 standard curves. Cathepsin K and the DQ gelatin fluorogenic substrate assay generate an E-64 standard curve that can be fit to a one-phase decay trend line (dotted line). Cathepsin L and the Z-FR-AMC fluorogenic substrate assay did not yield an E-64 standard curve with an acceptable trend line. N=3-5. Error bars = standard deviation.

4.3.5 Inhibition and Interference Assays

We tested the capacity of our microfluidic device components to individually inhibit cathepsin K and interfere with the DQ gelatin fluorogenic substrate assay. The discontinuous phase components included: PEGDA, DTT, and L0290 photoinitiator. The continuous phase components included: span-80 and mineral oil. We found that the total amount of PEGDA in our system has a maximum potential inhibitory effect of 38.1% ± 0.07% compared to control. We found that the total amount of DTT in our system has a maximum potential inhibitory effect of 17.2% ± 1.13% compared to control. We found that the total amount of L0290 in our system has a maximum potential inhibitory effect of 11.7% ± 1.56% compared to control. We found diluted span-80 remaining in our system (due to poor washing) has a maximum potential inhibitory effect of 17.6% ± 0.57% compared to control. We found diluted mineral oil remaining in our system (due to poor washing) has a maximum potential inhibitory effect of 1.55% ± 1.34% compared to control. Overall, all microfluidic device components except diluted mineral oil significantly inhibit cathepsin K activity relative to positive control (Figure 4.5a).

We found that the addition of PEGDA to the DQ gelatin fluorogenic assay has the potential to decrease the fluorescent signal (interference) by 13.8% ± 0.28%. We found that the addition of DTT to the DQ gelatin fluorogenic assay has the potential to decrease the fluorescent signal by 13.3% ± 0.78%. We found that the addition of L0290 to the DQ gelatin fluorogenic assay has the potential to decrease the fluorescent signal by 14.7% ± 0.57%. We found that the addition of diluted span-80 to the DQ gelatin fluorogenic assay has the potential to decrease the fluorescent signal by 29.1% ± 2.33%. We found that the addition of diluted mineral oil to the DQ gelatin fluorogenic assay has the potential to

decrease the fluorescent signal by 10.5% ± 0.99%. Overall, the addition of any component of our microfluidic device platform will cause interference of the fluorescent signal (Figure 4.5b).

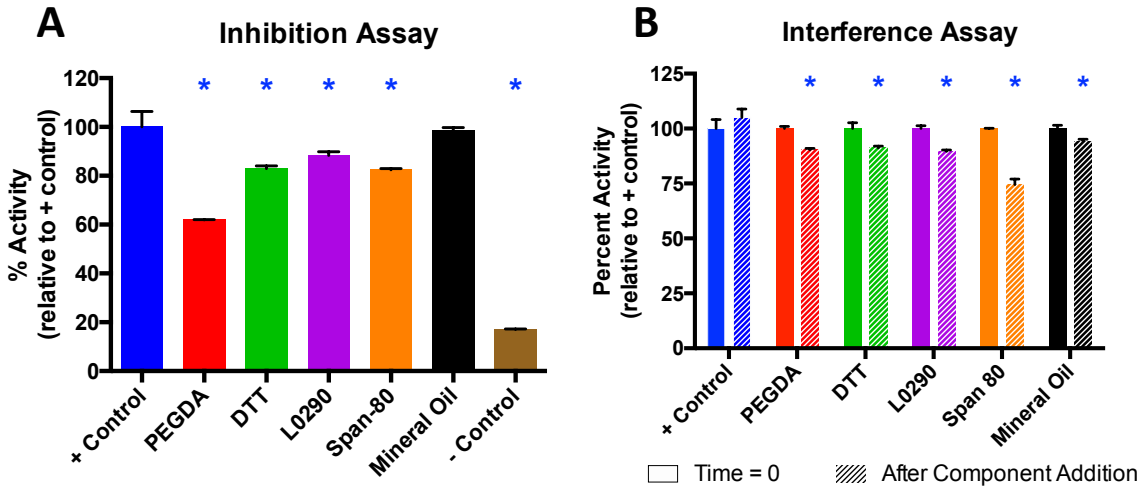

Figure 4.5: Components of microfluidic device have an effect on DQ gelatin assay fluorescent readings. (A) PEGDA, DTT, L0290, and diluted span-80 have a significant inhibitory effect on cathepsin K relative to the positive control (+ control) as indicated by the blue asterisk *p<0.05. (B) All components of our microfluidic device significantly interfere with the fluorescent signal in the DQ gelatin fluorogenic assay relative to the positive control (no inhibitor is present) indicated by the blue asterisk *p<0.05. N=3. Error bars = standard deviation.

4.3.6 Released E-64 from PEGDA Microparticles Inhibit Cathepsin K and Cathepsin L

E-64 loaded microparticles inhibited cathepsin L and cathepsin K significantly more than unloaded microparticles (Figure 4.6). Microparticles alone have virtually no inhibitory effect on active cathepsin L or cathepsin K proteases.

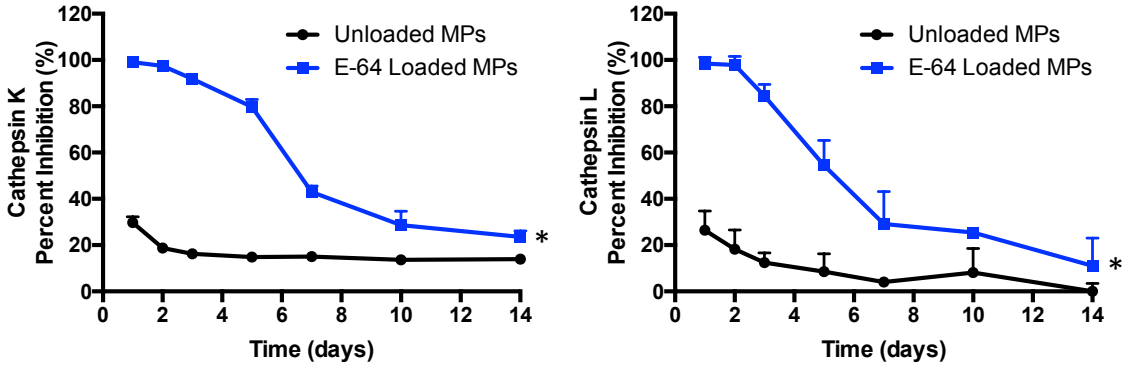

Figure 4.6: E-64 released from PEGDA microparticles fabricated with our microfluidic device remains bioactive over 14 days. (A) Plot of cathepsin K inhibition (DQ Gelatin Assay) treated with E-64 released from PEGDA microparticles and supernatant from unloaded microparticle control. (B) Plot of cathepsin L inhibition (Z-LR-AMC Fluorogenic Peptide Substrate Assay) treated with E-64 released from PEGDA microparticles and supernatant from unloaded microparticle control. N=3. *$p<0.05$.

4.3.7 Microfluidic Device Can Synthesize Tunable Release of E-64 from Microparticles

To assess what affects E-64 release kinetics from our loaded microparticles we varied polymer weight percent (10 wt% and 20 wt%), DTT concentration (5 mM and 10 mM), and initial E-64 loading amount (167 µg and 333 µg). We found that 20 wt% microparticles released greater amounts of E-64 compared to 10 wt% microparticles over 14 days (Figure 4.7c). We found that incorporation of 10 mM DTT resulted in greater E-64 release compared to 5 mM DTT in each polymer wt% group over 14 days (Figure 4.7d). Lastly, we found that greater initial loading concentration resulted in greater release of E-64 in the 20 wt% groups (Figure 4.7e). However, the 10 wt% group did not show any differences in E-64 release based on initial loading concentration (Figure 4.7e).

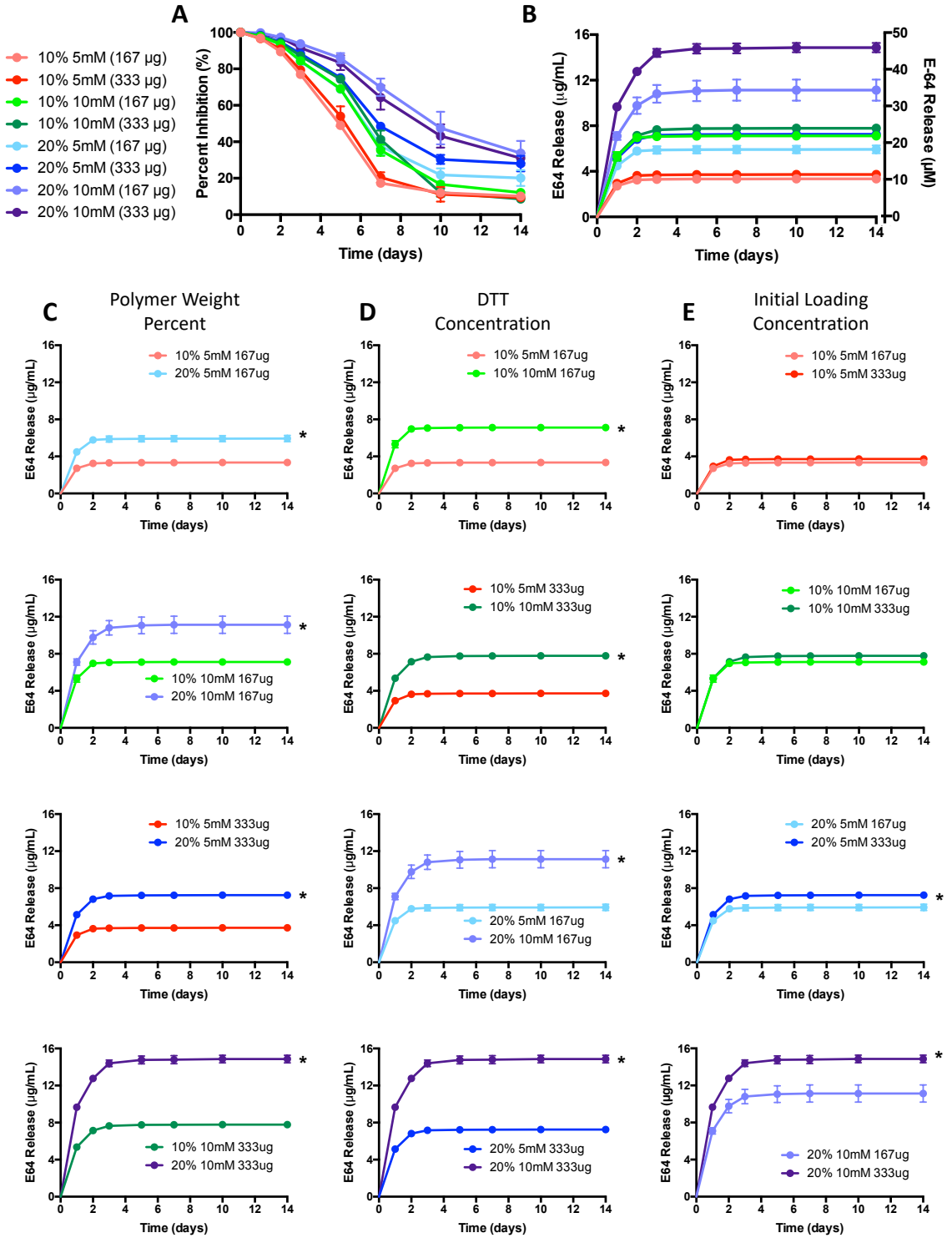

Figure 4.7: Microparticles fabricated with our microfluidic device can be tuned to alter release of E-64 by altering polymer weight percent, DTT concentration, and initial loading concentration. Microparticles were fabricated with a combination of 10 or 20 polymer weight percent (wt%), 5 or 10 mM DTT, and an initial loading of 167 or 333 µg E-64 as shown in the figure legend in the top left. All microparticles were

fabricated with 500 μL/min continuous phase and 3 μL/min discontinuous phase. (A) Percent inhibition of E-64 loaded microparticle supernatant at discrete time points. (B) E-64 release from E-64 loaded microparticles at discrete time points. Release quantified in μg/mL (left) and μM (right). (C) E-64 release as a function of polymer weight percentage. In this column of graphs, the DTT concentration and initial loading concentration are kept constant. (D) E-64 release as a function of DTT concentration. In this column of graphs, the polymer weight percent and initial loading concentration are kept constant. (E) E-64 release as a function of initial loading concentration. In this column of graphs, the polymer weight percentage and DTT concentration are kept constant.

4.4 Discussion

The goals of this work were to develop and characterize a novel microfluidic device that could load and release therapeutic molecules. This study outlines the development process of a novel microfluidic device platform. We characterized that our novel microfluidic device has the capability to synthesize uniformly sized microparticles in a variety of sizes, which broadens their applicability to for many fields and applications. Additionally, we demonstrated that we can load therapeutic molecules into the discontinuous phase for incorporation into the microparticle network for sustained release without any additional steps. Furthermore, we outlined the redevelopment of a currently available fluorogenic substrate assay for detection of small molecule release.

This work has contributed a novel microfluidic device platform that can synthesize uniformly sized microparticles in a variety of sizes (Figure 4.2). Our microfluidic device has the capacity to fabricate microparticles with a diameter between 25 and 400 μm (Figure 4.2d and 4.2e), which is wider than size ranges accomplished with other microfluidic devices [26,156]. We found that microparticle size was inversely proportional to both discontinuous and continuous flow rates, which aligns with our hypotheses. As the continuous phase speed is increased, there is an increase in shear

stress imposed on a microparticle droplet, which is directly responsible for the reduction in microparticle size [26]. Similarly, in order to synthesize a range of microparticle sizes dependent on the speed of the discontinuous phase, there must be a large difference in flow rate between the two phases in order to achieve a substantial sheer force on the microparticle droplet [26].

Our novel microfluidic device is similar to devices constructed in the Xia laboratory, which consist of poly(vinyl chloride) tubing, a syringe needle, and a glass capillary tube [26]. They have previously shown that microparticle size is inversely proportional to the continuous flow rate [26], which we also demonstrated in this work. However, they were not able to generate a wide variety of microparticle sizes by adjusting the discontinuous flow rate [26]. By their own admission, this was likely due to a relatively weak continuous phase net force in the system [26]. Essentially, the discontinuous and continuous flow rates were too similar and therefore could not generate a sufficient gradient of shear force on microparticle droplets [26]. However, in our novel microfluidic device platform, were able to generate a difference in speed of two orders of magnitude (3 μL/min vs. 500 μL/min) and fabricate microparticles between 24 μm and 285 μm by varying the discontinuous phase speed alone.

In addition to testing phase speed, we also tested surfactant concentration to modulate microparticle size. In our novel microfluidic device, there is a thermodynamic driving force towards homogenization of the system whereby all microparticles coalesce and minimize contact with the oil-based continuous phase [27]. To overcome this thermodynamic driving force, surfactants are added to stabilize microparticles. Without the addition of surfactants, when microparticle droplets come into close contact the

continuous phase between them will be depleted and allow the microparticle droplets to coalesce [27]. However, in the presence of surfactants on the two microparticle droplets, steric repulsion of the surfactant molecules will prevent the depletion of the continuous phase, which lengthens the time to continuous phase depletion and stabilizes both microparticles droplets against coalescence [27].

Previous groups that have investigated surfactants in the context of microfluidic devices have found that microparticle stability increases with increasing amounts of surfactants, which result in microparticle sizes of decreasing size [28,155]. However, eventually with increasingly greater amounts of surfactant will cause a microparticle size plateau, at which point the microparticle droplet can no longer associate with any extra surfactant molecules. The surfactant threshold varies depending on microparticle droplet size, the surfactant used, and the size of the microfluidic device [28]. In this work, we found that 20% and 40% span-80 produced similarly sized microparticles, which was the opposite of our initial hypothesis. Thus, 20% and 40% span-80 are likely above the threshold for our particular system. More investigative work would need to be performed to find the threshold of surfactant concentration for our novel microfluidic device platform.

We further characterized our novel microfluidic device beyond microparticle size range. We confirmed that our microfluidic device could fabricate microparticles capable of degradation (Figure 4.3). Specifically, we found that the 10 wt% 10 mM DTT microparticle formulation degraded prior to all other formulations, which aligns with our hypothesis that lower polymer weight percent and higher DTT concentration would result in the fastest degradation. Similarly, previous work has demonstrated that microparticle

degradation rate is proportional to DTT levels and inversely proportional to polymer weight percentage of the microparticle network [143]. This is due to a combination of factors. First, lower polymer weight percent creates a larger mesh size that allows greater swelling and thus more access to water and subsequent hydrolytic degradation. Similarly, the incorporation of DTT into the linear PEGDA network also causes a greater mesh size due to the increased distance between crosslinks. Furthermore, the incorporation of DTT into the PEGDA network increase the susceptibility of the resulting ester bond, which is the site of hydrolytic degradation [142]. Nevertheless, only a single formulation was able to fully degrade 77 days after fabrication. Thus, as designed our microparticles will remain at the site of injection longer than is necessary for therapeutic molecule release. Additionally, this suggests that degradation may not play a large factor in therapeutic molecule release. Thus, higher amounts of DTT can be incorporated into the microparticle network for faster degradation and potentially greater therapeutic molecule release. Previous work has demonstrated that release of loaded therapeutics can be modulated by the rate of hydrolytic degradation [134] and is therefore an important aspect to examine following changes to the microparticle polymer network.

In addition to fabricating degradable PEGDA microparticles, we demonstrated that our microfluidic device has the capacity to fabricate microparticles with additional biomolecules. Expressly, we were able to fabricate PEGDA microparticles with heparin, a negatively charged glycosaminoglycan (Figure 4.2c). We used heparin as a model glycosaminoglycan, but it has been extensively used in biomaterials for the purpose of protein sequestration, protein release, protein conformation protection, and maintenance of protein bioactivity [19,20,35–37,153]. Other glycosaminoglycans of interest that may

be compatible with this system include hyaluronic acid (HA). HA can bind CD44 a transmembrane glycoprotein found on mesenchymal stem cells (MSCs) [174], which have been widely investigated to treat a variety of diseases ranging from diabetes to osteoporosis [175]. Additionally, other groups have demonstrated that integrin-binding peptides can be incorporated into microparticles for delivery of islet cells for the purpose of alleviating the symptoms of diabetes [156]. Delivery of islet cells within a microparticle carrier may allow them to remain undetected by the immune system, which would prolong their presence and therapeutic efficacy [156]. Lastly, we demonstrated that fluorescent tags such as AlexaFluor633 are compatible with our microfluidic device platform despite the use of UV light, which could be useful for *in vivo* tracking protocols of therapeutic drugs or cell-based deliveries.

Initial trials of our microfluidic system for drug release included the addition of cystatin C into the discontinuous phase for incorporation into microparticles for *in vitro* release and eventual use in treating upregulated cathepsin proteases. However, we consistently detected very low release of cystatin C from our microparticles. Using fluorescently tagged cystatin C, we discovered that cystatin C predominately remained in the syringe after injection into the microfluidic device. Thus, cystatin C was not compatible with our microfluidic device and E-64, the small molecule analog of cystatin C was investigated for its potential use. The experimental outcomes with cystatin C are further described in Appendix A.

To determine if E-64 was compatible with our microfluidic device platform, we used the standard protocol for the DQ gelatin and Z-FR-AMC fluorogenic substrate assays. We verified that our microfluidic device could fabricate microparticles loaded

with E-64 based on the inhibitory effect of microparticle supernatant. Additionally, we were able to confirm that bioactive E-64 was released over 14 days (Figure 4.6). However, in order to quantify E-64 release, we were required to construct a standard curve with cathepsin and E-64 that could be fit with trend line. Using the same E-64 standard curve, we found that cathepsin L and cathepsin K interact with E-64 differently (Figure 4.4). Specifically, we found that cathepsin K interacts with E-64 such that a one-phase decay trend line could be fit and E-64 release from microparticles could be calculated. On the other hand, interaction with cathepsin L resulted in clustered values at lower E-64 concentrations and the inability to fit a trend line. This difference aligns with the literature that has shown that cathepsin L and cathepsin K have different dissociation constants with both their substrates and their inhibitors [11,108,176]. Thus, cathepsin K and the DQ gelatin fluorogenic substrate assay was chosen to quantify E-64 release from microparticles.

In addition to designing a novel microfluidic device, we also redesigned a currently available fluorogenic substrate assay for E-64 quantification in solution. E-64 is the small molecule analog of the endogenous cysteine cathepsin inhibitor [38] and has been shown to irreversibly bind cathepsins L, S, and K [39,40]. Previously, therapeutic use of E-64 had been limited to systemic, soluble injections of known amounts because E-64 is unable to be quantified by other standard methods [24,25]. For example, antibodies to E-64 do not exist and therefore an ELISA cannot be used. E-64 does not contain a ring structure and therefore cannot be detected using an absorbance reading on a plate reader [41]. Furthermore, E-64 cannot be detected on Bicinchoninic Acid assay (BCA) or Pierce Coomassie assay, which are to commonly used protein quantification

assays. Thus, the reinvention of the currently available DQ gelatin fluorogenic substrate assay allows our laboratory and others to more easily quantify E-64 release from biomaterial carriers.

Following the redevelopment of the currently available DQ gelatin fluorogenic substrate assay, we also examined the limitations of this new method. We found that microparticle components and fundamental materials required of our microfluidic device have the ability to obstruct our desired data measurements in large quantities. For example, PEGDA, a widely adopted polymer for biomaterial applications can inhibit cathepsin K upwards of 40% over control (Figure 4.5). However, this high level of inhibition was seen under conditions that mimicked complete and instantaneous degradation of our microparticles. Because our microparticles did not degrade within the time we were investigating E-64 release, the inhibition we detected was therefore due to E-64 and is not an artifact of the assay. However, this demonstrates that it is important to include unloaded microparticles as a control group. This will allow the user to distinguish the effect of the therapeutic inhibitor alone and the effect of the biomaterial carrier alone. Thus, an experiment that requires successive sample addition would require extra controls in order to obtain an accurate reading.

After developing a method to quantify E-64 release from our microparticles, we found that modifying polymer weight percentage, DTT concentration, and initial E-64 loading concentration (Figure 4.7) could tune overall E-64 release from microparticles. On average, increased polymer weight percent, DTT concentration, and initial loading resulted in the highest amount of E-64 released from microparticles fabricated with our microfluidic device. We had hypothesized that increased polymer weight would result in

a decrease in E-64 release due to a greater likelihood that E-64 would be unable to move as quickly through the polymer network and diffuse into solution, similar to previous findings [134]. However, we found that higher polymer weight percent resulted in greater amounts of E-64 released. While this was counterintuitive, this could be the result of how E-64 oriented itself with PEGDA in the discontinuous phase and during fabrication. E-64 could have caused interference with PEGDA crosslinking and resulted in a polymer network with a greater mesh size. Additionally, the higher polymer weight percent would likely prevent E-64 from coming into frequent contact with the syringe prior to introduction into the microfluidic device. This would result in less adsorption of E-64 to the syringe and therefore a greater amount of E-64 incorporated into microparticles. Similarly, lower polymer weight percent would increase the probability of E-64 adsorption to the syringe which could cause it to be removed from the discontinuous phase and ultimately result in lower E-64 release. Additionally, hypothesized that increased DTT concentration would result in greater amount of E-64 released over 14 days. We found that higher amounts of DTT did in fact result in greater amounts of E-64 release in both the 10 wt% and 20 wt% groups. The incorporation of higher amounts of DTT create a larger mesh size and it therefore is less interference of E-64 diffusion out of the microparticle. Lastly, we hypothesized that a greater initial loading of E-64 into the discontinuous phase would result in significantly more E-64 released over 14 days, similar to previous literature [134]. However, only the 20 wt% 10 mM group released more E-64 with a greater initial loading. The other groups did not demonstrate significant differences in E-64 release relative to initial loading. This could be due to E-64 adsorption to the syringe as mentioned previously.

Other work in the field has used injectable hydrogels to deliver small molecule matrix metalloproteinase inhibitor ß-cyclodextrin, which had been conjugated to hyaluronic acid [177]. They found that conjugation of the small molecule inhibitor resulted in sustained release over 21 days [177]. This system is different from the one described in this chapter in several ways. First, this group tested the release of ß-cyclodextrin from a hydrogel instead of microparticles. The surface area to volume ratio is different between hydrogels and microparticles and thus it is not surprising that the results are different. Secondly, they conjugated ß-cyclodextrin to the polymer network and we used entrapment. Release of ß-cyclodextrin was dependent on the introduction of hyaluronidase, while our method was exclusively hydrolytically degradable. Thus, the release kinetics of each system are inherently different.

Another group investigated co-release of small molecule anti-convulsant, adenosine, with protease inhibitor thylenediamine tetraacetic acid (EDTA) from protease-degradable silk films [178]. EDTA has been shown to inhibit calcium dependent cysteine proteinase and some matrix metalloproteinases [178]. They demonstrated that percent release of small dyes from silk films increases with increasing concentrations of proteinase type XIV [178]. EDTA were encapsulated in the silk films and achieved 100% release over 5 days regardless of proteinase type XIV presence, which indicates that its release is dictated by diffusion alone [178]. In the presence of proteinase type XIV, adenosine release without co-release of EDTA results in 100% release over 4 days, while the addition of EDTA co-release achieves 100% release over 8 days in the presence of proteinase type XIV [178]. Relative to our system, we achieved sustained release of a small molecule inhibitor over a longer period of time (5 vs. 14 days). Ultimately, this

system differs from our platform in several ways and cannot be directly compared. They encapsulated EDTA in a natural silk film, which is sensitive to protease-mediated degradation while we encapsulated E-64 in a hydrolytically degradable synthetic PEG-based microparticles.

4.5 Conclusion

In conclusion, we have created a novel microfluidic device platform that can synthesize uniformly sized PEGDA-based microparticles in a wide range of sizes. Advantages of our fabrication system include reduced material waste due to monodispersed size distribution and ability to tune hydrolytic degradation based on initial polymer formulation. In addition, this work outlined the redevelopment of the DQ Gelatin Fluorogenic Substrate Assay for better assessment of E-64 released from biomaterial carriers. Together, the technologies developed in this chapter allow small molecule, broad cathepsin inhibitor E-64 to be released in a sustained manner for localized inhibition, causing a reduction in off-target effects, and decrease the amount of E-64 needed for therapeutic efficacy compared to systemic delivery. Together, the work in this chapter allowed us to synthesize an injectable therapeutic treatment that can be used to probe the proteolytic network in our rat model of rotator cuff tear in chapter 5 (Aim 3). The 20 wt% 10 mM DTT 333 μg was the formulation that best matched the required level of E-64 release over one week required based on zymogram quantification in chapter 3 (Aim 1).

CHAPTER 5 THE EFFECT OF SUSTAINED RELEASE OF E-64 ON RELATIVE AMOUNTS OF ACTIVE PROTEASES FOUND WITHIN TENDON FOLLOWING FULL-THICKNESS ROTATOR CUFF TEAR IN A RAT MODEL

5.1 Introduction

Half of all shoulder injuries involve partial or full-thickness tear of one or more tendons of the rotator cuff [60]. Studies estimate that 34% of the population has a partial or full-thickness tendon tear in at least one shoulder [1]. Additionally, the risk of rotator cuff tear increases with age [1]. Patients living with a rotator cuff tendon tear experience pain, arm weakness, and limited mobility of the shoulder joint. Following rotator cuff tear, all tissues of the joint are affected. Specifically, the torn tendon becomes disorganized and loses collagen content [64]. The associated muscle experiences mechanical unloading and consequently becomes atrophied and develops fatty deposits between muscle fibers, which reduce muscle strength [70,179]. Lastly, the tendon tear disrupts the force balance of the shoulder joint and the articular cartilage of the glenohumeral joint is at an increased risk of developing osteoarthritis [5].

Surgical reattachment is often recommended for full-thickness tears and partial tears that have traversed 50% or more of the tendon [180,181]. To perform surgical re-attachment, a bone tunnel is formed in the humeral head with a drill and the tendon is anchored to the humeral head with a suture. Surgical reattachment of the torn tendon primarily reestablishes the force balance of the rotator cuff but does not reverse degeneration present at the time of treatment. Surgically reattached tendons have

documented re-tear rates ranging from 30-94% [6,7]. One study found that the most common mode of reattachment failure (19 of 22 total) was the tendon pulling away from intact sutures on the humeral head [79]. Thus, investigation into preventing or reducing tendon degeneration could improve surgical reattachment outcomes.

While degenerative damage seen after rotator cuff tear has been extensively documented, the biochemical processes that contribute to this extracellular matrix (ECM) degeneration are not fully known. As mentioned in previous chapters, families of proteases are responsible for a variety of homeostatic functions. Specifically, cathepsins and matrix metalloproteinases (MMPs) are responsible for extracellular matrix remodeling, bone resorption, and intracellular protein turnover [11,118,182]. Upregulated cathepsins and MMPs have been observed in a variety of degenerative diseases including tendinopathy, muscle atrophy, osteoarthritis [10,14,15,38,104,110,122–126,183]. Resident cells of the rotator cuff tissues (tendon, muscle, cartilage, and synovium) have been shown to release cathepsin and MMP proteases, which could contribute to the resulting degenerative damage [63,67,68,110,131,158,171]. An acute tear in one or more of the rotator cuff tendons causes an inflammatory response, which recruits neutrophils and macrophages to the site of injury [66]. Neutrophils and macrophages at the site of injury secrete proteases for the purpose of clearing debris, wound healing, and tissue remodeling [67–69]. Prolonged protease upregulation could be detrimental to tendon health and lead to degeneration. Thus, developing a treatment to inhibit upregulated proteases could preserve tendon tissue, aim in tendon healing, and also reveal information about how proteases contribute to tissue degeneration after rotator cuff tear.

In chapter 3 (Aim 1) of this work we used a rat model of rotator cuff tear to assess degenerative damage in joint tissues and characterize active proteases (both cathepsin and MMP families) spatially and temporally between the onset of injury and the manifestation of tissue degeneration. In tendon, we found significantly more active cathepsin L 1 week after injury and significantly more MMP-2 at 1 and 3 weeks after injury. Additionally, we detected significant cellular infiltration of inflammatory cells (macrophages and neutrophils) and significant degenerative changes in tendon 1 week after injury. This suggested that prolonged upregulation of proteases, possibly secreted by infiltrating inflammatory cells, could play a role in the degeneration of the supraspinatus tendon after rotator cuff tear. Overall, chapter 3 (Aim 1) provided target times for therapeutic intervention and a timeframe to probe for degenerative changes in each tissue. Thus, we used tendon as a model tissue in this study to investigate protease inhibitor treatment to decrease active cathepsin levels following an inflammatory injury (rotator cuff tear).

Several clinical trials have investigated systemic delivery of cathepsin inhibitors as therapeutic treatments to reduce or halt tissue degeneration [16]. Drawbacks of systemic delivery include non-specific inhibition of proteases (which can normal interrupt homeostatic functions) and high levels of therapeutic drugs required to achieve detectable effect in the diseased tissue (which will only receive a small fraction of the initial dose) [18]. Presently, all clinical trials utilizing cathepsin protease inhibitors have been abandoned due to severe side effects including headache, gastrointestinal disturbance, lung fibrosis, and skin lesions [16]. An alternative strategy to systemic delivery is employing the use of a biomaterial vehicle, such as that developed in chapter 4

(Aim 2) of this thesis, for localized delivery of inhibitor therapeutics to the site of disease or injury.

The ***objective*** of this aim was to understand how the proteolytic network the tendon tissue responds to local release of a cathepsin inhibitor (E-64) within the tendon 1 week after injury. The ***hypothesis*** of this aim is that sustained release of E-64 *in vivo* from PEG-based microparticles in the supraspinatus tendon will result in significantly less active cathepsin proteases after rotator cuff tear compared to injury only, soluble E-64 treatment, and unloaded microparticle treatment. Previous work has shown that active cathepsin proteases can cleave and activate MMPs [31] and chapter 3 (Aim 1) of this thesis demonstrated that cathepsins and MMPs were simultaneously active and upregulated in tendon after rotator cuff tear. Thus, we hypothesize that decreased levels of active cathepsin proteases will also result in significantly less active MMP proteases.

5.2 Materials and Methods

5.2.1 Fabrication of Microparticles for Tendon Injection Practice

The PEGDA used to fabricate microparticles in this chapter was from the same batch used in chapter 4. See section 4.2.1 for detailed methods on PEGDA synthesis and characterization. Additionally, see section 4.2.2 for detailed methods on the construction of the microfluidic device. For this particular method, DTT was not added into the discontinuous phase.

Following fabrication of nondegradable 20 weight percent (wt%) PEGDA microparticles, they were subsequently stained with aniline blue dye (5 mg/mL) and gently vortexed. The microparticles were centrifuged at 2,000 xg for 5 minutes and

excess aniline dye was removed with a serological pipette. The microparticles were repeatedly washed with phosphate buffered saline (PBS, Fisher) until the solution was clear, but the microparticles remained blue. In order to load the greatest number of microparticles into the syringe for injection, the microparticles were centrifuged down and excess volume was removed prior to syringe loading. Microparticles (volume: 10 μL) were taken up in 0.3 mL insulin syringes (BD) for injection.

5.2.2 Tendon Injection Practice

Rats maintained by the Physiological Research Laboratory (PRL) were obtained to practice tendon injections. Practice rats were similar in age and weight relative to previous studies [30]. Rats were euthanized with CO_2 prior to inducing the rotator cuff tear injury. Rotator cuff injury was induced using a previously established method in chapter 3 (Aim 1) [19,30,88], which can be found in section 3.2.1. After transection of the deltoid muscle to visualize the rotator cuff tendons, we used curved forceps under the supraspinatus tendon to elevate the tendon for better visualization and stabilize the tendon for better injection handling. We injected our nondegradable, 20 wt% aniline blue stained PEGDA microparticles into and along the tendon, such that the angle of the needle was nearly parallel to the tendon. Additionally, the use of curved forceps prevents the tendon from immediate retraction after transection and allowed for visual verification of aniline blue loaded microparticle within tendon. After injection, the supraspinatus and infraspinatus tendons were transected. The same procedure was done on the contralateral side prior to tissue isolation for histology. Macroscopic images of the supraspinatus tendon after aniline blue loaded PEGDA microparticle injection were taken with a DinoXcope camera (Dino-Lite Digital Microscope).

5.2.3 Tendon Injection Histology

The left and right supraspinatus muscles were isolated with their respective tendons. The muscles were fixed with 4% paraformaldehyde for 45 minutes at room temperature and washed with PBS for 10 minutes. The muscles were subsequently incubated in increasingly concentrated sucrose solutions with optical cutting temperature compound (OCT). The muscles were first incubated in 0% sucrose base solution (100 mL 10x PBS, 100 mL OCT, 800 mL) for 30 minutes under vacuum. The muscles were incubated in 10% and 20% sucrose solutions for 30 minutes each under vacuum. Muscles were transferred to histology molds and covered with 100% OCT compound overnight under vacuum. The following day, muscles in their histology molds were frozen down. First, a metal beaker was filled with 2-methylbutane and placed into a Styrofoam cooler filled with ethanol. Dry ice was added to the ethanol and the entire system was allowed to equilibrize for at least 30 minutes. The histology molds were placed inside the metal beaker and allowed to float until the topmost layer of OCT turned white. The histology molds were subsequently submerged in the 2-methylbutane for an additional 5 minutes and stored at -80 °C overnight. Supraspinatus tendon/muscle was cross sectioned in 10 μm slices using a cryostat (CryoStar NX70, Thermo Fisher) and stained with hematoxylin and eosin (H&E) (Richard Allan Scientific). Tissue sections were imaged using light microscopy (Nikon TE2000).

5.2.4 Fabrication of Microparticles with Fluorescently-Tagged E-64

The PEGDA used to fabricate microparticles in this chapter was from the same batch used in chapter 4. See section 4.2.1 for detailed methods on PEGDA synthesis and

characterization. Please refer to section 4.2.2 for detailed methods on the construction of the microfluidic device. For this particular method, we fabricated 20 wt% 10 mM microparticles loaded with 333 μg of fluorescently tagged E-64, which is outlined in section 4.2.2. Lastly, microparticles were loaded into syringes described in section 5.2.1.

E-64 was fluorescently tagged with IRDye 800 CW Protein Labeling Kit (Licor). A vial of E-64 (1 mg, Millipore-Sigma) was resuspended at a final concentration of 40 mg/mL and well mixed over low heat. In a low-binding tube 25 μm of E-64, 5 μm of potassium phosphate buffer, and 20 μm of dye was added and incubated at room temperature protected from light for 2 hours. This reaction was performed at a 1:10 molar ratio of dye to E-64 to ensure that any detected dye was bound to a molecule of E-64. Because the dye molecule is larger than E-64, separating free dye would not be possible. Following incubation, E-64 was sterile filtered (0.22 μm filter, Costar) and stored at -20 °C until use.

To allow for synthesis of sterile microparticles, after the microfluidic device was created on the bench top, it was run with 70% ethanol from both ends for a minimum of 15 minutes in a biosafety cabinet. All microparticle components were sterile filtered (0.22 μm filter, Costar) at 10,000 xg for 3 minutes, while mineral oil was sterile filtered and span-80 was autoclaved. Microparticles were washed and resuspended in sterile PBS and loaded into syringes (reference section 5.2.1) in the biosafety cabinet to ensure sterility.

5.2.5 In vivo Release of Tagged E-64

Rotator cuff injury was induced using a previously established method in chapter 3 (Aim 1) [19,30,88], which can be found in section 3.2.1. Tendons were injected as previously described in section 5.2.2. [184]

Following rotator cuff injury, both rat shoulders were shaved for better depth penetration on the near infrared microscope. Fluorescence measurements were taken at Days 0 (immediately after wound closure), 1, 3, 5, 7, 14, and 21 and the animals were allowed to recover after each time point. Near infrared (NIR) images of the supraspinatus tendon were captured using the Dixon laboratory custom NIR imaging system [184–186]. The NIR system consists of an EMCCD camera (Evolve eXcelon, Photometrics), a stereo-microscope (Olympus), and a xenon arc lamp (Sutter Instrument Company). Also, the stero-microscope is equipped with NIR band pass excitation and long pass emission filters. Fluorescence images were captured at 0.63x magnification at various time points with fixed camera exposure time of 250 ms for soluble tagged E-64 and 2,000 ms for tagged E-64 loaded microparticles using the MicroManager software. Using a custom MATLAB (Mathworks) code, the region of interest (ROI) for each image was determined by isolating the 5% most intense pixels. The pixels within the ROI were subsequently averaged to obtain the mean fluorescence intensity. Data points were fitted to a mono-exponential function (Origin software): $f(t) = y_0 + A * \exp(-t/\tau)$, where y_0 is the offset, t is time, A is normalized fluorescence at $t = 0$, and τ is time constant. Due to the large difference in exposure time between the soluble and microparticle groups, relative background was subtracted prior to creating the heat maps.

5.2.6 Fabrication of Microparticles for Surgical Procedure

The PEGDA used to fabricate microparticles in this chapter was from the same batch used in chapter 4. See section 4.2.1 for detailed methods on PEGDA synthesis and characterization. Please refer to section 4.2.2 for detailed methods on the construction of the microfluidic device. For this particular method, we fabricated 20 wt% 10 mM microparticles loaded with 333 μg of E-64, which is outlined in section 4.2.2. Lastly, microparticles were loaded into syringes described in section 5.2.1.

5.2.7 Surgical Procedure and Outcome Measure Time Points

Rotator cuff injury was induced using a previously established method in chapter 3 (Aim 1) [19,30,88], which can be found in section 3.2.1. Refer to section 5.2.2 for details on tendon injection protocol.

The treatments for this study included: E-64 loaded microparticles, soluble E-64 injection, and unloaded microparticles. Soluble E-64 injection was equal to expected E-64 release from loaded microparticles over 1 week based on *in vitro* release quantification outlined in Chapter 4 (Aim 2). All treatments were compared to injury only (historical data) [30]. A single time point (1 week) was chosen for this study based on previous data from Chapter 3 (Aim 1) that demonstrated significantly more active cathepsin L and MMP-2 proteases in injured tendon at 1 week [30].

5.2.8 Multiplex Gelatin Zymography

Refer to section 3.2.5 for details on supraspinatus tendon isolation and multiplex gelatin zymography methods.

5.3 Results

5.3.1 Tendon Injection Practice

Initially we aimed to inject our aniline blue loaded PEGDA microparticles into the entire length of the supraspinatus tendon. However, after several dissections, we learned that the supraspinatus tendon anatomy is not perfectly conserved between animals. Specifically, we found the supraspinatus tendon could be so deep that it was flat against the scapula or more shallow and in the middle of the supraspinatus muscle. There is no way to determine the supraspinatus tendon anatomy prior to dissection. Thus, due to the variable anatomy of the supraspinatus tendon within the muscle, it is incredibly difficult to consistently inject into the length of the tendon.

Consequently, we instead aimed to inject and therefore treat the proximal third of the tendon, which is visible during the surgical procedure, which can be seen in Figure 5.1a. To verify that microparticles can be repeatedly injected into the proximal third of the tendon during the rotator cuff tear surgery, we used aniline blue loaded PEGDA microparticles in our practice rats. Figure 5.1a shows the intact supraspinatus tendon after injection with aniline blue loaded PEGDA microparticles, but before transection. Figure 5.1b shows the supraspinatus tendon after aniline blue loaded PEGDA microparticle injection and transection. The supraspinatus tendon and muscle after dissection is captured in Figure 5.1c.

After aniline blue loaded PEGDA microparticle injection and subsequent isolation of the supraspinatus muscle (attached to the supraspinatus tendon), we prepared the tissue for cryosection. We performed an H&E stain on cross sections of our supraspinatus

tendon/muscle at various depths, seen in Figure 5.1d. The H&E stain allowed us to distinguish regions of the supraspinatus tendon/muscle. As can be seen in Figure 5.1, regions 1 and 2 are purely tendon tissue, while regions 3 and 4 contain both tendon and muscle tissue. Interestingly, the aniline blue loaded PEGDA microparticles took up the hematoxylin stain therefore could be visualized and quantified. In total, we found that 93% of all sections contained at least 1 microparticle. Furthermore, we found that regions 1 and 2 had an average of 5.2 ± 2.6 microparticles/section, while regions 3 and 4 had an average of 10.1 ± 6.8 microparticles/section.

Table 5.1: Tendon Injection Practice Microparticle Quantification

Percentage Of Histological Sections That Contained At Least 1 Microparticle	93 %
Average Number Of Microparticles In Sections 1 And 2 (Tendon Only Regions)	5.2 ± 2.6 microparticles/section
Average Number Of Microparticles In Sections 3 And 4 (Tendon And Muscle Regions)	10.1 ± 6.8 microparticles/section

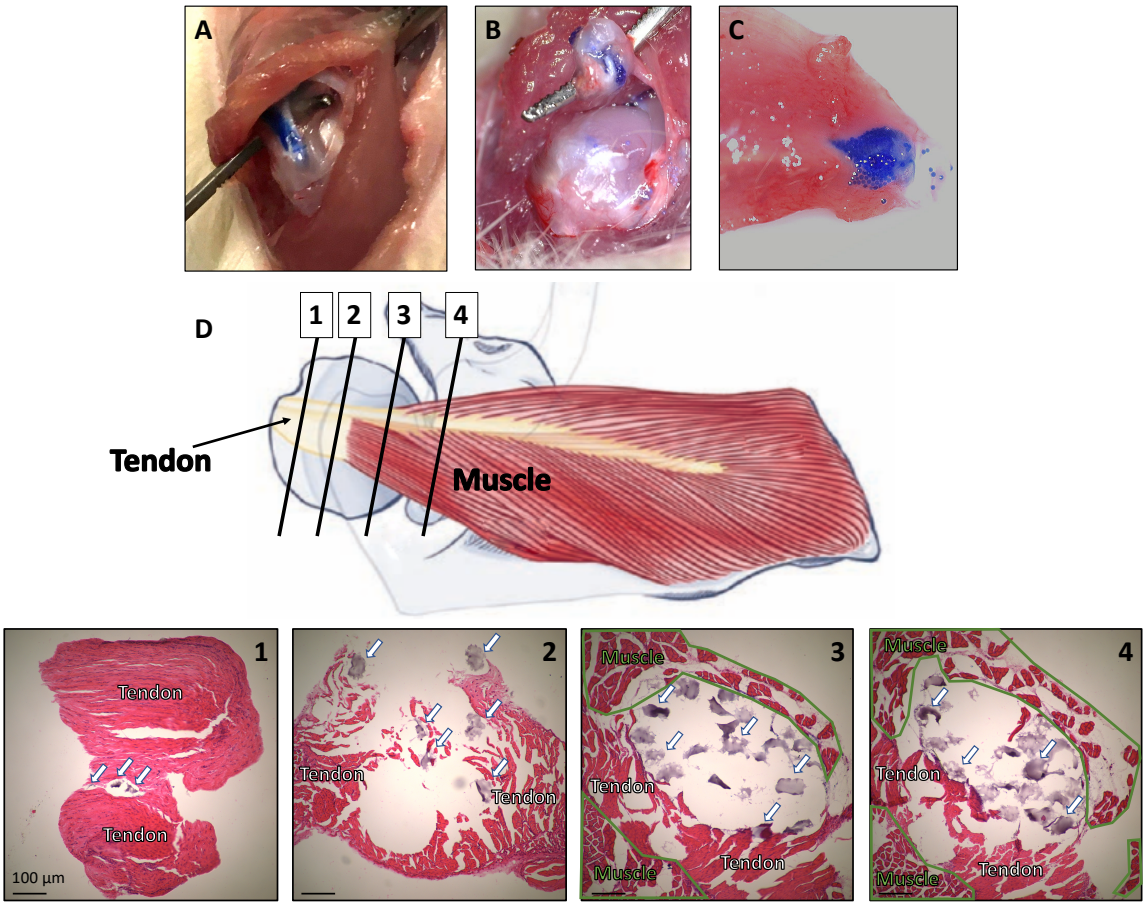

Figure 5.1: Aniline blue loaded PEGDA microparticles were successfully injected into the medial third of the supraspinatus tendon. (A) Macroscopic image of the supraspinatus tendon after aniline blue loaded PEGDA microparticle injection, but before transection. (B) Macroscopic image of the supraspinatus tendon after aniline blue loaded PEGDA microparticle injection and transection. (C) Macroscopic image of dissected supraspinatus tendon/muscle after aniline blue loaded PEGDA microparticle injection. (D) Schematic of supraspinatus tendon anatomy within supraspinatus muscle (adapted from Miranda, et al. *American Journal of Roentgenology*. 2019). The numbers on the schematic correspond to the histological sections of the supraspinatus tendon/muscle stained with H&E beneath. Scale bar = 100 µm. N=8 supraspinatus tendon/muscles analyzed. N=15 sections per supraspinatus tendon/muscle were imaged and quantified.

5.3.2 In vivo Release of Tagged E-64

Soluble injection of tagged E-64 could not be detected within the rotator cuff after Day 1, which can be seen in the representative heat map in Figure 5.2a and the quantification in Figure 5.2d. Conversely, signal from tagged E-64 injected in microparticles could be detected in all animals at Day 21 (Figure 5.2e). However, there was very large variability between animals, which is demonstrated by the two representative heat maps in Figure 5.2b and 5.2c. Additionally, three animals injected with tagged E-64 microparticles (rats 1, 2, and 5) demonstrated high detectable levels after a period of low detection which can be seen in Figure 5.2e. Two-way ANOVA analysis showed that there was a significant difference between tagged E-64 injected in soluble form versus in loaded microparticles ($p = 0.0387$). Specifically, we were able to detect tagged E-64 at the site of injection significantly longer when injected via microparticles compared to soluble injection. Additionally, there was significantly higher detection of tagged E-64 in loaded microparticles compared to soluble tagged E-64 at Day 3.

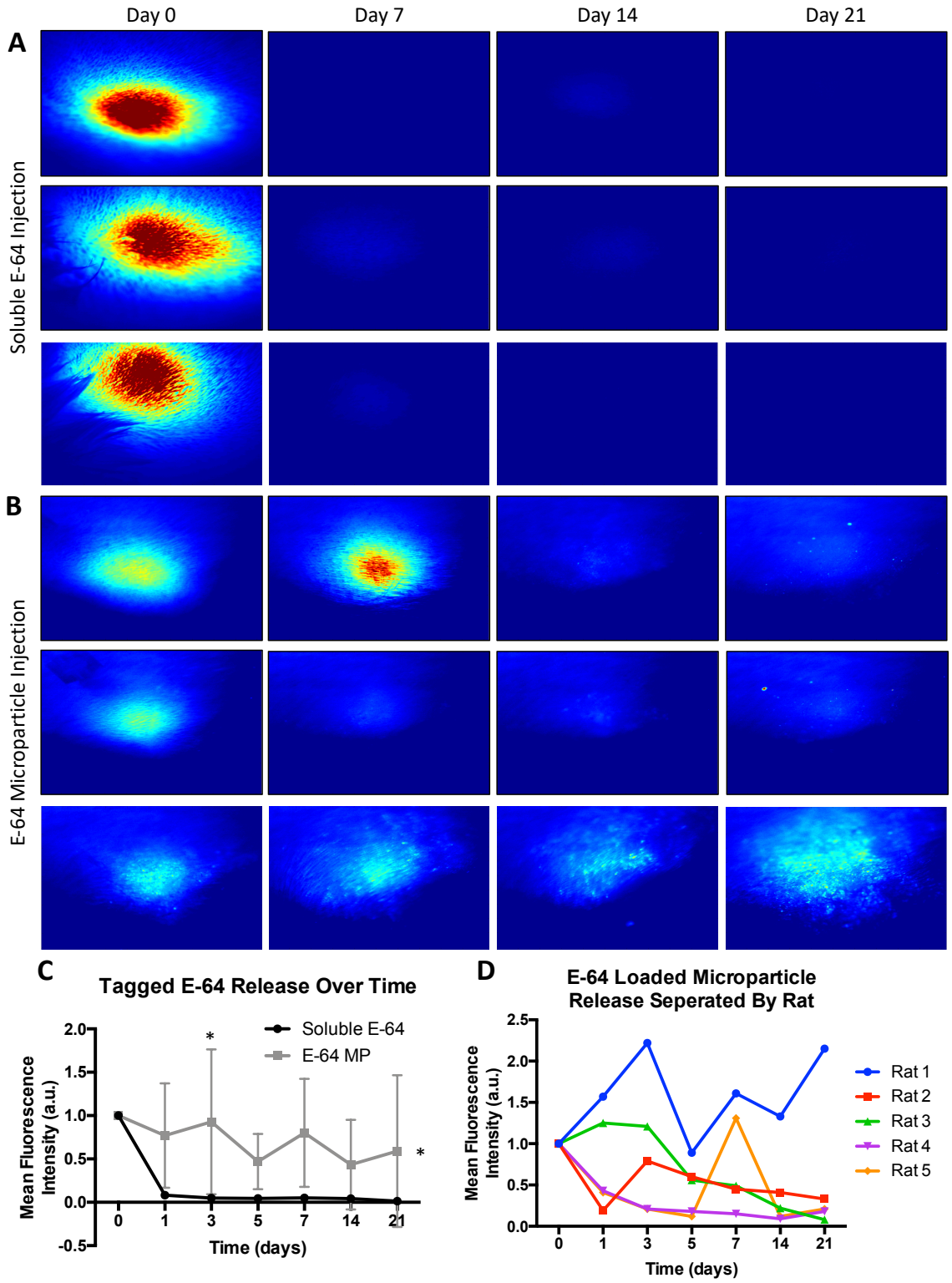

Figure 5.2: Tagged E-64 loaded in microparticles remains in the rotator cuff significantly longer than soluble tagged E-64. (A) Representative images of detected tagged soluble E-64 in the rotator cuff over time. (B) Representative images of detected tagged E-64 loaded microparticles in the rotator cuff over time. (C) Quantification of

tagged E-64 detection in rats injected with soluble tagged E-64 or tagged E-64 loaded microparticles. (D) Detection of tagged E-64 microparticle injection variability between rats. N=5. *p<0.05.

5.3.3 Cathepsin Multiplex Gelatin Zymography of Supraspinatus Tendon

Active cathepsin L was detected in pH4 and pH6 cathepsin zymograms between 37 and 25 kDa (Figure 5.3a-f) 1 week after injury in all tendons (including injured and uninjured contralateral control tendons). Densitometric analysis revealed significantly more active cathepsin L in injured supraspinatus tendon with E-64 microparticle treatment compared to uninjured contralateral control (Figure 5.3a and 5.3d). Densitometric analysis revealed significantly more active cathepsin L in injured supraspinatus tendon with soluble E-64 treatment compared to uninjured contralateral control (Figure 5.3b and 5.3d). Densitometric analysis revealed significantly more active cathepsin L in injured supraspinatus tendon with unloaded microparticle treatment compared to uninjured contralateral control (Figure 5.3c and 5.3d). Furthermore, we found that treatment with E-64 loaded microparticles yielded a 6 fold increase in active cathepsin L levels relative to uninjured contralateral control (Figure 5.3e). Similarly, we found that soluble E-64 treatment resulted in a 2.6 fold increase in active cathepsin L levels relative to uninjured contralateral control (Figure 5.3e). The unloaded microparticle group was included as a biomaterial control to isolate the contribution of microparticles alone to changes in relative levels of active cathepsin L. Injury and treatment with unloaded microparticles resulted in a 3 fold increase in active cathepsin L levels relative to uninjured contralateral control (Figure 5.3e). Additionally, we found proteases at high molecular weights in both cathepsin pH 4 and pH6 zymograms. However, bands with a molecular weight higher than 75 kDa were not analyzed due to

the inability to correctly identify the protease associated with these bands. For completeness, we included historical densitometric data of active cathepsin L following injury alone (no treatment), which was discussed in chapter 3 (Aim 1). We did not find any significant changes in active cathepsin L levels following any treatment relative to historically injury alone data (Figure 5.3d and 5.3e).

Cathepsin zymograms at pH 6 did not detect any active cathepsin K at the expected molecular weight of 75 kDa (Figure 5.4). However, active cathepsins at high molecular weights were detected (Figure 5.4). Their identity could not be determined without additional analysis with western blot.

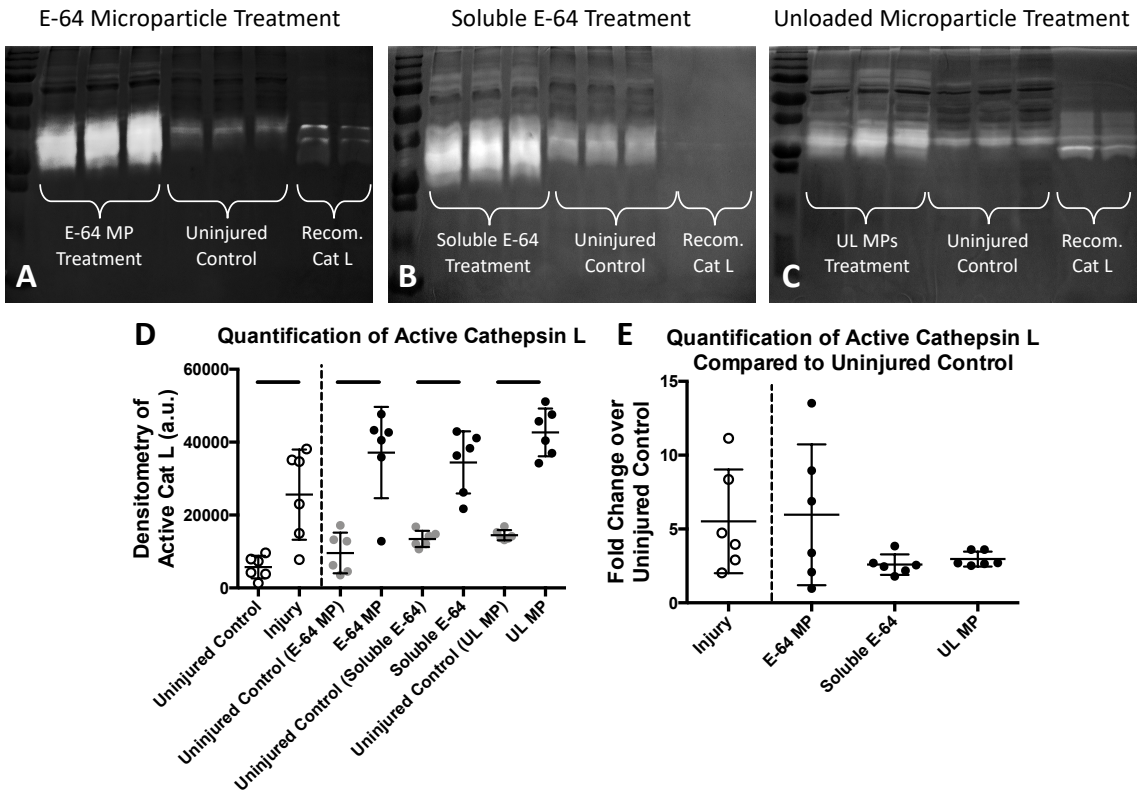

Figure 5.3: Cathepsin multiplex gelatin zymography shows significant increase in active cathepsin L proteases after injury regardless of treatment. (A) Cathepsin pH4 zymogram of tendons treated with E-64 loaded microparticles (E-64 MP). (B) Cathepsin pH4 zymogram of tendons treated with soluble E-64. (C) Cathepsin pH4 zymogram of tendons treated with unloaded microparticles (UL MP). (D) Densitometric quantification of active cathepsin L following all treatments. (E) Densitometric quantification of active cathepsin L following all treatments normalized to respective uninjured contralateral controls. Recombinant cathepsin L was used as zymography control. N=6. *$p<0.05$. Error bars = standard deviation.

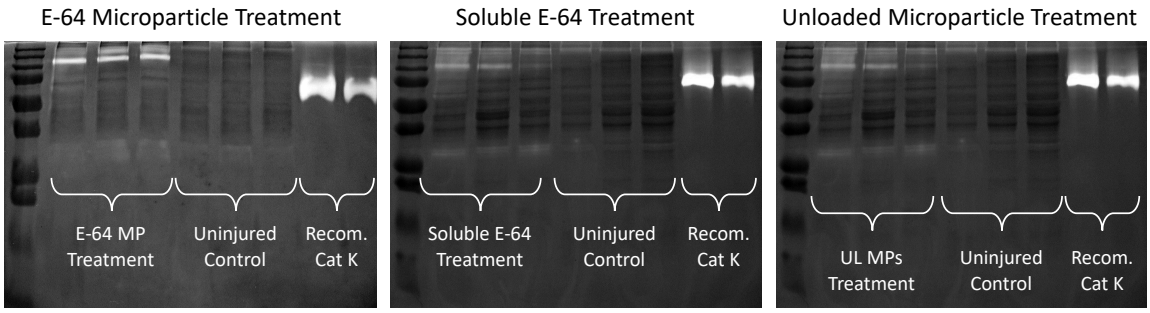

Figure 5.4: Cathepsin multiplex gelatin zymography shows no active cathepsin K after injury regardless of treatment. (A) Cathepsin pH6 zymogram of tendons treated with E-64 loaded microparticles (E-64 MP). (B) Cathepsin pH6 zymogram of tendons treated with soluble E-64. (C) Cathepsin pH6 zymogram of tendons treated with unloaded microparticles (UL MP). Recombinant cathepsin K was used as zymography control. N=6.

5.3.4 MMP Multiplex Gelatin Zymography of Supraspinatus Tendon

Pro- and mature MMP-2 were detected in MMP zymograms (Figure 5.5a-c) between 50 and 75 kDa 1 week after injury in all tendons (including injured with treatment tendons and uninjured contralateral control tendons). Densitometric analysis revealed significantly more active MMP-2 in injured supraspinatus tendon with E-64 microparticle treatment compared to uninjured contralateral control (Figure 5.5a and 5.2d). Densitometric analysis revealed significantly more active MMP-2 in injured supraspinatus tendon with soluble E-64 treatment compared to uninjured contralateral control (Figure 5.5b and 5.5d). Densitometric analysis revealed significantly more active MMP-2 in injured supraspinatus tendon with unloaded microparticle treatment compared to uninjured contralateral control (Figure 5.5c and 5.5d). Furthermore, we found that treatment with E-64 loaded microparticles yielded an 8 fold increase in active MMP-2 levels relative to uninjured contralateral control (Figure 5.5e). Similarly, we found that soluble E-64 treatment resulted in a 5.5 fold increase in active MMP-2 levels relative to uninjured contralateral control (Figure 5.5e). The unloaded microparticle group was included as a biomaterial control to isolate the contribution of microparticles alone to

changes in relative levels of active MMP-2. Injury and treatment with unloaded microparticles resulted in a 13 fold increase in active MMP-2 levels relative to uninjured contralateral control (Figure 5.5e). Bands with a molecular weight higher than 75 kDa were not analyzed due to the inability to correctly identify the protease associated with these bands. Additionally, we found active proteases at low molecular weights (~37 kDa) in all MMP zymograms. For completeness, we included historical densitometric data of active MMP-2 following injury alone (no treatment), which was discussed in chapter 3 (Aim 1). We did not find any significant changes in active MMP-2 levels following any treatment relative to historically injury alone data (Figure 5.5d and 5.5e).

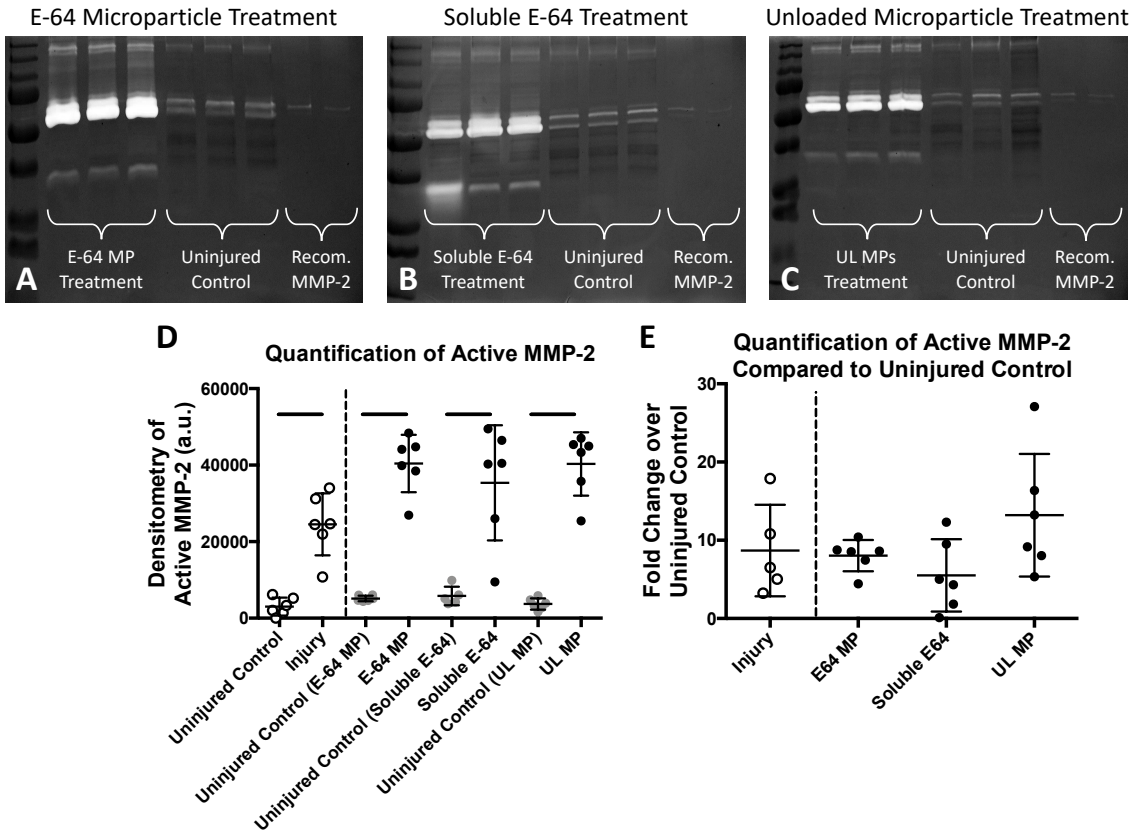

Figure 5.5: MMP multiplex gelatin zymography shows significant increase in active MMP-2 proteases after injury regardless of treatment. (A) MMP zymogram of tendons treated with E-64 loaded microparticles (E-64 MP). (B) MMP zymogram of tendons treated with soluble E-64. (C) MMP zymogram of tendons treated with unloaded microparticles (UL MP). (D) Densitometric quantification of active MMP-2 following all treatments. (E) Densitometric quantification of active MMP-2 following all treatments normalized to respective uninjured contralateral controls. Recombinant MMP-2 used as control. N=6. *$p<0.05$. Error bars = standard deviation.

5.4 Discussion

Following the identification of active proteases in supraspinatus tendon after rotator cuff tear in chapter 3 (Aim 1) and developing a microfluidic device platform for the fabrication of microparticles to locally deliver protease inhibitor, E-64, chapter 4 (Aim 2) we began the work to test our treatment in our rat model of rotator cuff tear in this study. First, we found that we could consistently inject microparticles into the proximal third of the supraspinatus tendon (Figure 5.1). Second, with the use of near

infrared imaging, we found that soluble injection of tagged E-64 cleared the supraspinatus tendon area after 1 day following injection, while we were able to detect tagged E-64 loaded in microparticles out to day 21. Third, we found that treatment with E-64 loaded microparticles did not cause a significant decrease in active cathepsin L in supraspinatus tendon 1 week after injury and treatment. Additionally, active cathepsin L levels following treatment with soluble E-64 and unloaded microparticles was not significantly different from treatment with E-64 loaded microparticles.

In the process of practicing tendon injection, we found that injection into the length of the supraspinatus tendon is technically difficult due to differences in tendon anatomy between animals. While examining other work that has targeted rotator cuff tendons for injection-based therapies, we found the employed methods of these groups described various injection protocols including injection into the subacromial space, the supraspinatus muscle, or simply into the rotator cuff repair site [42–45]. While the objective of all of these studies was to treat rotator cuff tendons, injection into adjacent tissues suggests that these groups also found that consistent injection into the length of tendon was technically challenging. Thus, we were required to modify our surgical approach in order to test how the injection of E-64 loaded microparticles influenced the regulation of active proteases exclusively in supraspinatus tendon following rotator cuff tear.

Hence, we modified out strategy and found we could consistently inject into the proximal third of the supraspinatus tendon. Thus, we decided to inject, treat, and analyze only the proximal third of the supraspinatus tendon after rotator cuff tear. As can be seen in Figure 5.1a, the aniline blue microparticles are located within the proximal third of the

tendon after injection and remain there following transection (Figure 5.1b) and isolation (Figure 5.1c). Overall, we found that 93% of the sections from the proximal third portion of the injected supraspinatus tendon contained at least 1 microparticle. Therefore, we confirmed that our modified approach was sufficient to test our hypothesis that areas of the injured supraspinatus tendon that received sustained E-64 treatment via microparticle delivery would subsequently demonstrate a significant decrease in active cathepsin levels.

We tested the *in vivo* release of tagged E-64 following injection into the supraspinatus tendon in soluble form or loaded into microparticles. We found that tagged E-64 injected in soluble form was unable to be detected after 1 day, while tagged E-64 loaded into microparticles could be detected up to 21 days after injection. These results demonstrated that soluble injection of tagged E-64 is cleared from the rotator cuff area soon after injection and therefore cannot have a prolonged effect on injured tissue. However, injection of tagged E-64 loaded in microparticles was detected for 3 weeks after injection into the supraspinatus tendon. This prolonged residence in the rotator cuff would be necessary for localized, sustained release of E-64 to inhibit upregulated proteases following injury.

However, as can be seen in Figure 5.2e there was very large variability between animals. This wide variability could have been caused by various factors. NIR imaging is limited by tissue depth, such that the accuracy of tagged E-64 detection decreased with increased tissue depth. The supraspinatus tendon is located beneath the trapezius, deltoid, and supraspinatus muscles [70,187,188]. While the trapezius and deltoid muscles were considered sufficiently thin by our laboratory having limited knowledge of the NIR

system, subsequent tissue dissection revealed to Dixon laboratory collaborators that this platform was not compatible with our rat model of rotator cuff tear. Essentially, released tagged E-64 migrating towards the surface of the skin will result in a much higher signal compared to equal quantities of tagged E-64 in the much deeper supraspinatus tendon. This limitation is likely the leading cause for the high variability of tagged E-64 detected in our rat model of rotator cuff tear. Even if perfect supraspinatus tendon injection was achieved, microparticles could still have the opportunity and means to migrate away from the injection site during subsequent movement by the animals over 3 weeks.

In particular, rats 3 and 4 demonstrated steady decay of tagged E-64 detection, while rats 1, 2, and 5 demonstrated an increase in tagged E-64 detection after an initial decrease in signal. This could be possible if rats 3 and 4 had microparticles that moved towards the surface of the skin and released E-64 in a more expected manner. However, microparticles injected into rats 1, 2, and 5 could have remained at the injection site, beneath several layers of muscle and the increase in tagged E-64 detection was the result of several waves of E-64 release reaching the surface of the skin. Previously, NIR imaging has been used to image lymphatics in the knee, which are located beneath the skin and therefore are not limited by tissue depth and are easily imaged [184]. While NIR imaging is very sensitive and can detect low levels of tagged protein, it is limited by tissue depth [185]. Previous work with tissue phantoms in the Dixon laboratory have documented that their NIR imaging platform cannot accurately detect signal located deeper than 6 mm away from imaging source [185]. An alternative imaging platform that has been used by other groups is the *In Vivo* Imaging System (IVIS). IVIS imaging has been previously used to demonstrate exponential decay of tagged VEGF and BMP-2

proteins from biomaterial carriers [22,189]. While IVIS is not limited by tissue depth in small animals including rats and mice, it requires substantially larger quantities of tagged protein for detection [19]. Thus, groups have the option of injecting tagged proteins at a significantly higher dosage than therapeutically necessary in order to achieve IVIS detection, but it is possible that the therapeutic dosage and the detectable dosage would have different *in vivo* release profiles. Thus, as used previously neither imaging platform is compatible with our system. An alternative recommendation in order to accurately capture tagged E-64 in vivo release from soluble injection or microparticle injection includes performing several terminal procedures. Specifically, we would induce injury and inject tagged E-64 treatments as before, but instead of performing a longitudinal study, we would euthanize rats at pre-determined time points. Euthanizing the rats would allow us to remove the deltoid and trapezius muscles in order image the supraspinatus muscle without being limited by NIR depth penetration.

In these studies, we tested E-64 in a soluble form and loaded in a microparticle vehicle to inhibit active cathepsin proteases. As a control, we also tested unloaded microparticles. In contrast to our hypothesis, all groups resulted in significantly more active cathepsin L relative to their uninjured contralateral controls regardless of treatment (Figure 5.3g). Additionally, no treatment resulted in significantly less active cathepsin L relative to untreated injury alone (historical data). Although these results are unexpected, the proteolytic network is incredibly complex and there are several inherent limitations of our zymography analysis. Previously, it was generally accepted that E-64 inhibits cathepsin proteases via covalently binding to the cathepsin active site [40]. However, more recently it has been shown that E-64 can disassociate from cathepsins during the

zymography process, which could allow an inhibited cathepsin to be reactivated in the zymogram, leading to a "false positive" level of activity [39]. Additionally, zymography alone does allow us to identify the high molecular weight bands seen in our zymograms to include in our quantification. Lastly, zymography analysis of the tendon requires breakdown of extracellular matrix proteins and lysis of tenocytes and any other cells associated, thus does not allow us to determine if active cathepsin L is upregulated intracellularly or extracellularly. The main purpose of our E-64 treatments was to inhibit active cathepsin proteases in the extracellular space to reduce tendon degeneration. The dosage of E-64 delivered is not enough to trigger endocytosis of E-64 [190], therefore intracellular cathepsin L would be unaffected by our therapeutic treatment, but would be quantified in our zymograms similarly to extracellular cathepsin L and potentially mask the effects of our E-64 treatment. Thus, if detected cathepsin L is predominately located intracellularly, our treatment could still result in a decrease in tendon degeneration despite no detectable differences in active cathepsin levels compared to injury alone.

While zymography analysis is important in understanding how E-64 may be affecting upregulated cathepsins, extensive further analysis is required to fully understand the potential effects of our E-64 loaded microparticle treatment in our rat model rotator cuff tear. Zymography can identify active proteases, but western blot analysis has the capacity to identify the total amount of proteases regardless of activity, which would include inactive procathepsins. A series of western blots could identify changes in cathepsin levels, which may not be detected with zymography. Additionally, performing western blots would allow us to identify the high molecular weight bands seen in our

zymograms to include in our quantification and thus, more accurately quantify levels of active cathepsins between treatments.

As mentioned previously, zymography does not distinguish intracellular versus extracellular cathepsins. Thus, we can perform *in situ* zymography [162] or immunohistochemistry with DQ gelatin [38] on histological tendon sections to garner a better understanding of where cathepsin proteases are upregulated to gain a better understanding of how our E-64 treatment may have influenced proteases after injury. Additionally, zymography does not provide any information on the source of the active proteases (resident tenocytes versus infiltrating inflammatory cells). Thus, performing *in situ* zymography [162] or immunohistochemistry with DQ gelatin [38] would provide more information on the source of the active proteases, which may be useful in developing tailored therapies in the future. Additionally, in parallel, the histological tendon sections could also be used to assess tendon degeneration following treatment. Should there be a decrease in supraspinatus tendon degeneration, it would indicate that a sufficient amount of extracellular cathepsin proteases were inhibited by our E-64 treatment, which was unable to be detected by zymography. Histological analysis of tendon including hematoxylin and eosin staining and second harmonic generation would allow us to observe any morphological changes in tendon structure and collagen alignment [30].

Previous examination of supraspinatus tendon after rotator cuff tear injury demonstrated significant upregulation of MMP-2 in addition to cathepsin L with significant tendon degeneration 1 week after injury (chapter 3, Aim 1) [30]. In the absence of regulation, the destructive nature of MMPs would completely degrade the

extracellular matrix proteins that constitute tendon. MMP-1 activity has been shown to be significantly greater in human supraspinatus tendon following rupture [122] and MMP-1 and -3 have been shown to be upregulated within synovial fluid following rotator cuff tendon tear in humans [123]. Furthermore, MMP expression can be readily increased in response to stimuli such as inflammatory cytokines [130] and can be secreted by inflammatory cells such as macrophages [67]. While E-64 is purely a cathepsin inhibitor, previous work has demonstrated that cathepsins have the capacity to cleave and activate MMPs [31]. Thus, investigating MMP-2 activity provide information on how these two families of proteases interact following rotator cuff tear. Similar to cathepsin zymograms, the MMP zymograms showed significantly more active MMP-2 in all groups relative to their uninjured contralateral controls regardless of treatment (Figure 5.5d). Despite evidence that cathepsins can cleave MMPs, because cathepsin proteases were similarly upregulated regardless of the E-64 treatment, we are unable to draw any conclusions about cross-activity between these two families of proteases.

There were a variety of potential confounding factors in this study that likely contributed to the lack of evidence of cathepsin inhibition *in vivo*. While the tendon injection practice images demonstrate that we could consistently inject our microparticles into the tendon of a euthanized rat, the zymography analysis was performed on rats that had been given an injection and allowed to recover and survive for 1 week after injury. It is possible the E-64 loaded microparticles did not remain in the tendon in every rat for the entire 1 week after injury and treatment. This is further supported by the large variability seen in the *in vivo* release of tagged E-64 (Figure 5.2) and suggests that the high variability between animals treated with E-64 loaded microparticles could be due to

microparticle migration differences. To mitigate this confounding factor, we could add immobilization of the injured forelimb for the duration of the 1 week study. Previous work has demonstrated increased tendon healing following massive rotator cuff tear and immobilization with either botulinum toxin A (Botox) injections or cast immobilization [44].

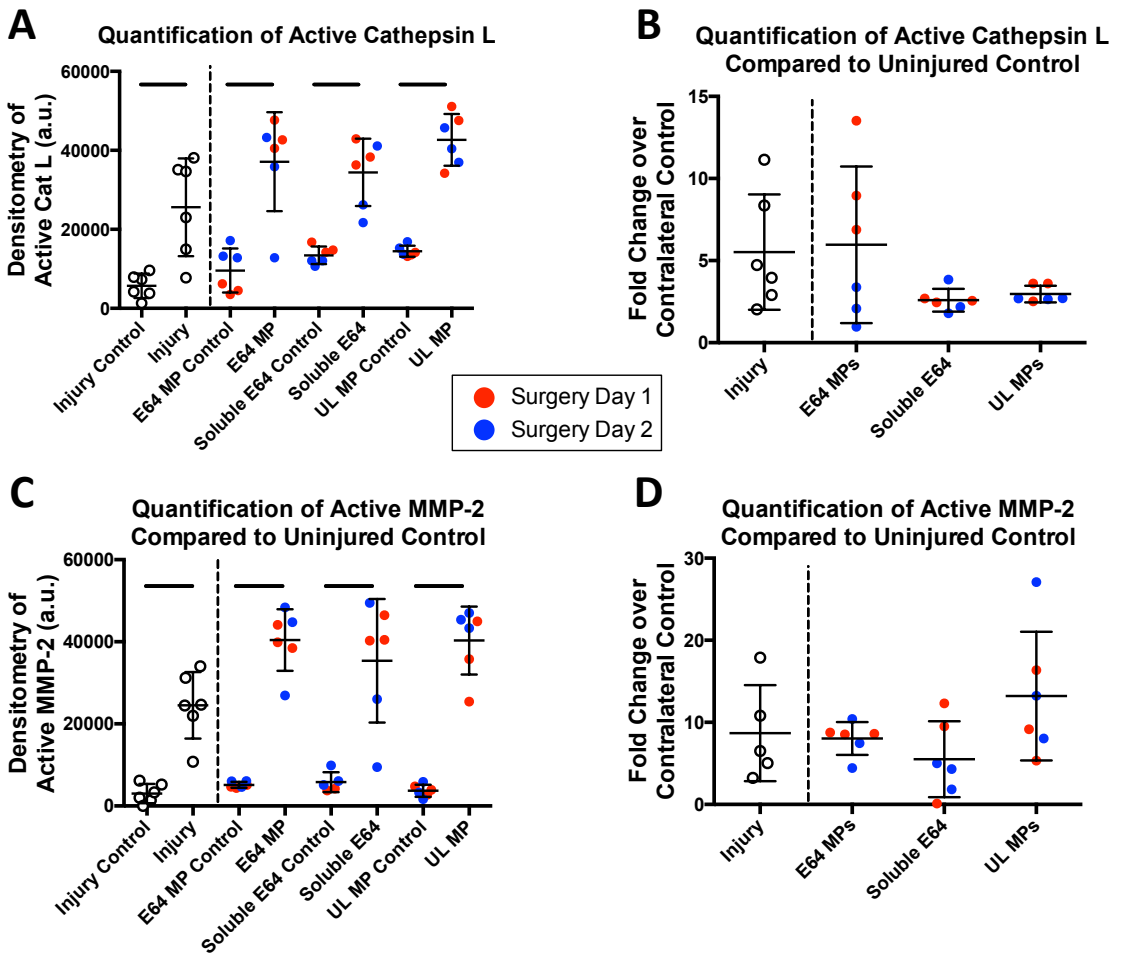

Figure 5.6: Quantification of active protease divided by date of surgery suggests it may be a contributing factor to variability.

Additionally, Figure 5.6 demonstrates that the rats themselves could be an additional source of variation. As can be seen in Figure 5.6a, in rats treated with E-64 loaded microparticles, their respective uninjured contralateral control tendons show a

clear divide between the first and second surgery date despite the fact that the animals were delivered together and not treated differently. Interestingly, in this set of studies we see a general increase in the amount of active cathepsin L found in uninjured contralateral control tendons compared to our historical data (injury alone) seen in Figure 5.6a. The differences between uninjured contralateral control tendons injected with E-64 loaded microparticles is further exacerbated in Figure 5.6b when active cathepsin L levels in injured tendon were normalized. Interestingly, we did not see similar division in the rats treated with soluble E-64 or unloaded microparticles, which likely contributed to the low variability seen in Figure 5.6b.

Furthermore, a potential limitation of this final study is the E-64 dosage. The amount of injected E-64 used in this final study (both in soluble and loaded microparticle form) was based on the amount of active cathepsin proteases found in the supraspinatus tendon 1 week after rotator cuff tear in chapter 3 (Aim 1). However, we do not know the relative amounts of active proteases between injury and 1 week. As shown in chapter 4 (Aim 2), the majority of release occurs within 5 days, thus it is possible that there was an insufficient dose of E-64 by the 1 week time point that would yield significant inhibition of cathepsin proteases.

Lastly, our injection protocol could be further improved by adding ultrasound imaging to our injection protocol. The Soslowsky laboratory has previously used ultrasound imaging to perform dry needling procedures on rat supraspinatus tendons without performing an open surgery [191]. The use of ultrasound imaging could be used to guarantee injection in the length of supraspinatus tendon for treatment throughout the tendon tissue. Additionally, the ultrasound imaging protocol could also be used for

precise injection and treatment into the most proximal portion of the supraspinatus muscle. It has been shown that the supraspinatus muscle undergoes degenerative changes asymmetrically, such that the muscle closest to the tendon and humeral head insertion will develop degenerative changes first and propagate to the more medial portions over time [192]. Lastly, the addition of ultrasound imaging would allow for repeated injections into the supraspinatus tendon or muscle because we would not be required to re-open up the animal.

5.5 Conclusion

This work is the first step in investigating protease contribution to joint tissue degeneration after rotator cuff tear. We established that we could consistently inject microparticles into the proximal third of the supraspinatus tendon in our rat model of rotator cuff tear and found that *in vivo* release of E-64 from microparticles is highly variable, which can affect the efficacy of our localized treatment. While our treatment with E-64 loaded microparticles did not yield reduced levels of active proteases, additional work is warranted to better determine the cellular source of active proteases and the localization of proteases (intra vs. extracellular) to improve the efficacy of our microparticle delivery treatment. After further refinement of this animal model, such a system could be used to probe the role of protease inhibition in both tendon degeneration, as well as, more broadly, acute inflammation in musculoskeletal tissues.

CHAPTER 6 CONCLUSIONS AND RECOMMENDATIONS

6.1 Summary

Rotator cuff tears account for half of all shoulder injuries [60]. It is estimated that 34% of the population has a partial or full-thickness tear [1]. The risk of rotator cuff tear increases with age, such that over 50% of people over 60 years old have a partial or full-thickness rotator cuff tear in at least one shoulder [1]. Patients suffering from a rotator cuff tendon tear experience pain, arm weakness, and limited mobility of the shoulder joint. If left untreated, a partial tear will likely propagate to a full-thickness tendon tear [61], while an untreated full-thickness tendon tear will eventually cause degeneration of the associated muscle, articular cartilage, and underlying subchondral bone of the shoulder [47].

Currently available treatment strategies for patients that have suffered a rotator cuff tendon tear include regimented nonsteroidal anti-inflammatory drugs (NSAIDs), physical therapy, and eventually surgical reattachment of the torn tendon. However, surgical reattachment of torn rotator cuff tendons does not reverse degeneration present at the time of surgery. Furthermore, instance of tendon re-tear following surgical reattachment has been found to correlate to muscle degeneration (muscle atrophy and fatty infiltration) at the time of surgery [76–78] and there are documented re-tear rates ranging from 30-94% [6,7]. Additionally, it has been shown previously in humans that the most common mode of reattachment failure is the reattached rotator cuff tendon pulling away from intact sutures on the humeral head [79]. Thus, degeneration of both

rotator cuff tendons and muscles may be contributing factors to surgical reattachment failure (tendon retear).

While resulting degeneration caused by a torn rotator cuff tendon is clear, the exact biochemical processes that cause this degeneration is unknown. A possible cause for the extensive joint tissue degeneration observed following rotator cuff tear is the prolonged activation of proteases. Proteases are specialized enzymes whose primary function is to degrade proteins. Of particular interest are cysteine cathepsins and matrix metalloproteinases (MMPs), which play a role in many facets of homeostasis within the human body including extracellular matrix remodeling, bone resorption, and intracellular protein turnover [9–11]. However, these two families of proteases have also been observed to be upregulated in a variety of degenerative diseases in orthopaedics, including atrophy of the tibialis anterior muscle [12], osteoarthritis of the knee [13], and tendinopathy [14,15]. Upregulated proteases have been implicated in a variety of musculoskeletal diseases, which makes protease inhibitors an appealing potential treatment.

Several protease inhibitors have been tested in human clinical trials to treat dysregulated cathepsins and MMPs, but all have been abandoned due to serious off-target effects including headache, gastrointestinal disturbance, lung fibrosis, and skin lesions [16,17]. Thus far, clinical trials have utilized systemic delivery of protease inhibitors, which act upon all encountered proteases equally, regardless of its role in normal homeostasis or disease progression. An alternative strategy to systemic delivery is employing the use of a biomaterial vehicle for localized delivery of inhibitor therapeutics to the site of disease or injury. Limiting treatment to the diseased or injured tissue would

provide necessary treatment without deleterious side effects. Microparticles are a frequently used biomaterial vehicle for therapeutic drug or protein delivery [134] because they can be injected directly into the tissue of choice.

The goal of this dissertation work was to understand how proteases contribute to joint tissue degeneration (tendon, muscle, and cartilage) after rotator cuff tear. Understanding the spatial and temporal distribution of upregulated proteases after rotator cuff tear can best inform therapeutic treatments to prevent degeneration, which would result in improved surgical outcomes after rotator cuff tear re-attachment surgery. First, using a rat model of rotator cuff tear that has been shown to replicate degenerative damage seen in humans [23], we investigated active proteases in each joint tissue (tendon, muscle, and cartilage) over time. Second, we designed a novel microfluidic device to fabricate uniformly sized microparticles that can be loaded with protease inhibitors for subsequent use *in vivo*. Also, we reinvented a currently available fluorogenic substrate assay for the detection of E-64 (a broad, small molecule cathepsin inhibitor), which was our desired therapeutic. Lastly, we tested our E-64 loaded microparticles system on supraspinatus tendon tissue in our rat model of rotator cuff tear as a test bed to elucidate the effect of sustained release of a broad cathepsin inhibitor on active proteases.

In chapter 3 of this dissertation, we used a rat model of massive rotator cuff tear injury to identify active, upregulated proteases in joint tissues (supraspinatus tendon, supraspinatus muscle, and humeral head cartilage) over time. Overall, we found that the temporal profiles of cathepsins and MMPs were regulated differently. Specifically, cathepsins were more active in the first week in all three tissues, while MMP-2 was

upregulated in supraspinatus tendon at 1 and 3 weeks, upregulated in supraspinatus muscle only at 3 weeks, and never significantly upregulated in humeral head cartilage. Additionally, we found that significant protease upregulation did not necessarily coincide with manifestation of visible tissue damage. While all three joint tissues had significant upregulation of proteases 1 week after injury, only the supraspinatus tendon had developed degenerative changes at that time point. We did not identify significant degeneration in the supraspinatus muscle or humeral head cartilage until 3 and 12 weeks after injury respectively. Overall, we demonstrated that our rat model of massive rotator cuff tear could mimic degenerative changes seen in humans in all three joint tissues, which could be used as a test bed for therapeutic treatments that aim to reduce and manage joint tissue degeneration prior to surgical reattachment of torn rotator cuff tendons. Additionally, characterization of the spatial and temporal profiles of cathepsin and MMP proteases provided a baseline to test protease inhibitor therapies in our rat model of massive rotator cuff tear.

In chapter 4 of this dissertation we developed and characterized a novel microfluidic device. We determined that our microfluidic device could fabricate uniformly sized microparticles in a variety of sizes ranging from 25 to 400 μm. Additionally, our microfluidic device platform could covalently incorporate biomolecules such as heparin into microparticles. Crosslinkers such as DTT could also be added to our fabricated microparticles to allow for hydrolytic degradation. Furthermore, we redeveloped a currently available fluorogenic substrate assay for quantification of E-64 in solution. Additionally, we found that microparticle components can have varying effects on cathepsin K inhibition and interference with fluorescent readings. We found that E-64

loaded into the discontinuous phase of our novel microfluidic device was incorporated into the resulting microparticles and retained the ability to inhibit cathepsins K and L over at least 14 days. In addition, we found that we could vary E-64 release by varying polymer weight percentage (wt%), DTT concentration, and initial loading of E-64. Specifically, we found that microparticles with higher polymer weight percentage and DTT concentration released more E-64 over time. Interestingly, only one formulation demonstrated higher E-64 release with greater initial loading of E-64 in the discontinuous phase. In sum, we found that 20 wt% microparticles with 10 mM DTT and an initial loading of 333 μm released the greatest amount of E-64 over 14 days. Therefore, we chose this formulation for our subsequent studies.

In chapter 5 of this dissertation we tested our E-64 loaded microparticles in our rat model of massive rotator cuff tear. We found that the anatomy of the supraspinatus tendon in rats is complex and variable between animals. Thus, we were unable to perform consistent injection into the length of the supraspinatus tendon in our rat model of rotator cuff tear. However, we found we could consistently inject microparticles into the proximal third of the supraspinatus tendon, which we visualized with H&E staining and light microscopy. Additionally, we tested the *in vivo* release of tagged E-64 in soluble form and loaded into microparticles. We found that tagged E-64 injected in soluble form was unable to be detected after 1 day, while tagged E-64 loaded into microparticles could be detected out to 21 days after injection. While tagged E-64 was detectable significantly longer when loaded into microparticles, there was very large variation between rats. Finally, we tested our E-64 loaded microparticles in our rat model of massive rotator cuff tear. We also tested soluble E-64 and unloaded microparticles as controls. Overall, we

found there was significantly more active cathepsin L and MMP-2 proteases compared to uninjured contralateral controls regardless of treatment. Additionally, we found no significant differences in active protease levels (cathepsin L or MMP-2) following treatment compared to injury alone (historical data).

6.2 Conclusions

The work outlined in this dissertation first identified specific protease targets within joint tissues over time. This information provided a baseline to develop a plan for more tailored treatment in our rat model of rotator cuff tear. Second, this thesis work provided two new technological advancements to subsequently be used to treat dysregulated proteases *in vivo*. Our novel microfluidic device allows us to fabricate suitably sized microparticles loaded with therapeutic molecules in a high throughput way. Additionally, we reinvented a currently available fluorogenic substrate assay that allows E-64 (whose uses had been previously limited by detection methods) to be investigated as a potential therapeutic treatment. The culmination of this thesis work allowed us to test a localized protease-inhibitor based treatment to treat upregulated proteases in supraspinatus tendon in an established rat model of rotator cuff tear. The contribution of this body of work provides a therapeutic strategy to improve the current gold standard of treatment following rotator cuff tear. Reduced joint tissue degeneration prior to surgical reattachment would ultimately result in fewer instances of re-tear and overall improved surgical outcomes.

The objective of chapter 3 was to assess degenerative damage in joint tissues following rotator cuff tear in a rat animal model and characterize active proteases (both

cathepsin and MMP families) spatially and temporally between the onset of injury and the manifestation of tissue degeneration. We found significantly more active cathepsin L in supraspinatus tendon at 1 week after injury and significantly more active MMP-2 at 1 and 3 weeks after injury. Additionally, we found significantly more cathepsin L in supraspinatus muscle at 1 and 3 weeks after injury, while we found significantly more active MMP-2 at 3 weeks. Lastly, humeral head cartilage demonstrated significantly more active cathepsin L and K at 1 week after injury. In addition to observing protease in joint tissues over time, our rat model of massive rotator cuff tear also developed significant degeneration in each joint tissue. After 1 week, the supraspinatus tendon had observable changes in collagen structure and alignment. The supraspinatus muscle developed significant fibrous tissue between muscle fibers [19] after 3 weeks, which is indicative of substantial degeneration. Degeneration of humeral head cartilage was identified via the development of localized loss of cartilage (focal defects) in 4 out of 8 animals. Interestingly, we also found that focal defects did not develop within the same region of the humeral head unlike what has been seen previously in a rat model of osteoarthritis of the knee [165]. This suggests that areas of cartilage degeneration are influenced by usage and activities specific to the individual.

Additionally, we found neutrophils and macrophages had infiltrated the supraspinatus tendon by 1 week following injury. However, the cellular source of proteases has yet to be fully identified and are likely a combination of several tissue-resident cells, as well as cells recruited due to injury, as proteases released in one area can diffuse throughout the joint. Resident cells of the joint tissues, including tendon, muscle, cartilage, and synovium have all shown to be capable of producing proteases

[63,110,131,158,171]. In addition to joint tissue cells, recruited inflammatory cells, such as macrophages and neutrophils, have the capacity to release proteases [67,68]. Investigation of the cellular source of these proteases would provide information for more targeted therapeutic intervention.

The validation of an animal model of massive rotator cuff tear that recapitulates characteristic joint tissue degeneration seen in humans would be exceedingly valuable to test therapeutic treatments that could preserve joint tissue health and improve success rates of rotator cuff tendon reattachment surgeries. A more comprehensive understanding of biochemical changes to joint tissue over time following rotator cuff tear will better inform ideal intervention times and treatments for each tissue. These results demonstrate concomitant degeneration in a number of rotator cuff tissues after traumatic injury and suggest that early intervention addressing multiple tissues simultaneously may be required to prevent joint degeneration after rotator cuff tear.

The objective of chapter 4 was to develop a novel microfluidic device to fabricate uniformly sized PEGDA microparticles and characterize release of E-64 *in vitro* over time using different fabrication parameters in our microfluidic device system. Our novel microfluidic device has the capacity to fabricate uniformly sized microparticles ranging from 25 to 400 μm, which is wider than size ranges accomplished with other microfluidic devices [26,156] and therefore can be useful for a larger number of applications. Additionally, we found that we could incorporate DTT into the microparticle network to fabricate hydrolytically degradable microparticles, which is relevant to many biomedical applications that do not want biomaterial carriers to remain in the body for longer than necessary for treatment. Also, we demonstrated that our novel microfluidic device

platform could also incorporate biomolecules such as heparin into the microparticle network, which has been used for a variety of applications including protein sequestration, protein release, protein conformation protection, and maintenance of protein bioactivity [19,20,35–37,153].

Additionally, we demonstrated that we could load therapeutic molecules into the discontinuous phase for incorporation into the microparticle network for sustained release without any additional steps. Specifically, we were able to load and release small molecule, broad cathepsin inhibitor E-64 directly into the discontinuous phase for subsequent microparticle release. Furthermore, we found that we could tune E-64 release by varying polymer weight percent (10 wt% and 20 wt%), DTT concentration (5 and 10 mM), and initial loading concentration (167 μg and 333 μm). On average, increased polymer weight percent, DTT concentration, and initial loading resulted in the highest amount of E-64 released from microparticles fabricated with our microfluidic device. We had hypothesized that increased polymer weight would result in a decrease in E-64 release due to a greater likelihood that E-64 would be unable to move as quickly through the polymer network and diffuse into solution, similar to previous findings [134]. However, we found that higher polymer weight percent resulted in greater amounts of E-64 released. Additionally, hypothesized that increased DTT concentration would result in greater amount of E-64 released over 14 days. We found that higher amounts of DTT did in fact result in greater amounts of E-64 release in both the 10 wt% and 20 wt% groups. The incorporation of higher amounts of DTT create a larger mesh size and it therefore is less interference of E-64 diffusion out of the microparticle. Lastly, we hypothesized that a greater initial loading of E-64 into the discontinuous phase would result in significantly

more E-64 released over 14 days. Interestingly, contrary to previous literature [134], higher amounts of E-64 loading did not result in greater amounts of E-64 release except for the 20 wt% 10 mM group. The other groups did not demonstrate significant differences in E-64 release relative to initial loading. Overall, we found that the 20 wt% 10 mM 333 μm initial E-64 loading resulted in the greatest amount of E-64 release over 14 days, which was subsequently used for *in vivo* testing in chapter 5 because it was sufficient E-64 release to achieve a 1:1 molar ratio with cathepsin L levels quantified in chapter 3. Thus, our novel microfluidic device platform has practical applications in a variety of fields including drug delivery and tissue engineering.

In addition to designing a novel microfluidic device, we also redesigned a currently available fluorogenic substrate assay for E-64 quantification in solution. E-64 is the small molecule analog of the endogenous cysteine cathepsin inhibitor [38] and has been shown to irreversibly bind cathepsins L, S, and K [39,40]. Previously, therapeutic use of E-64 had been limited to systemic, soluble injections of known amounts because E-64 is unable to be quantified by other standard methods [24,25]. For example, antibodies to E-64 do not exist and therefore an ELISA cannot be used. E-64 does not contain a ring structure and therefore cannot be detected using an absorbance reading on a plate reader [41]. Furthermore, E-64 cannot be detected on Bicinchoninic Acid assay (BCA) or Pierce Coomassie assay, which are to commonly used protein quantification assays. Thus, the reinvention of the currently available DQ gelatin fluorogenic substrate assay allows our laboratory and others to more easily quantify E-64 release from biomaterial carriers.

The objective of Aim 3 was to investigate how the proteolytic network responds to local cathepsin inhibition within the tendon 1 week after injury. Using a near infrared dye, we tagged E-64 for the purposes of assessing *in vivo* release over time. Specifically, we injected tagged E-64 in soluble form and tagged E-64 loaded microparticles into the supraspinatus tendon in our rat model of rotator cuff tear. We were unable to detect tagged E-64 that had been injected in soluble form after 1 day. This indicates that it had been cleared from the area in that time. Conversely, we were able to detect tagged E-64 that had been injected in loaded microparticles over 21 days. This indicated that the injected microparticles had persisted in the rotator cuff area to allow for sustained detection of E-64 over 21 days. However, the release curves from animals injected with tagged E-64 loaded microparticles was highly variable, which suggests that each animal was not experiencing similar treatment.

This wide variability could have been caused by various factors. NIR imaging is limited by tissue depth, such that the accuracy of tagged E-64 detection decreased with increased tissue depth. The supraspinatus tendon is located beneath the trapezius, deltoid, and supraspinatus muscles [70,187,188]. While the trapezius and deltoid muscles were considered sufficiently thin by our laboratory having limited knowledge of the NIR system, subsequent tissue dissection revealed to Dixon laboratory collaborators that this platform was not compatible with our rat model of rotator cuff tear. Essentially, released tagged E-64 migrating towards the surface of the skin will result in a much higher signal compared to equal quantities of tagged E-64 in the much deeper supraspinatus tendon. This limitation is likely the leading cause for the high variability of tagged E-64 detected in our rat model of rotator cuff tear. Even if perfect supraspinatus tendon injection was

achieved, microparticles could still have the opportunity and means to migrate away from the injection site during subsequent movement by the animals over 3 weeks.

Furthermore, we assessed active cathepsin levels following massive rotator cuff tear injury and treatment with E-64 loaded microparticles, soluble E-64, or unloaded microparticles in our rat model using multiplex gelatin zymography. All treatment groups resulted in significantly more active cathepsin L and MMP-2 relative to their uninjured contralateral controls regardless of treatment. Additionally, no treatment resulted in significantly less active cathepsin L relative to untreated injury alone (historical data). However, there are inherent limitations to multiplex gelatin zymography and additional analysis is warranted to fully understand the effect of our E-64 treatment in our rat model of rotator cuff tear. Previously, it was generally accepted that E-64 inhibition of cathepsin proteases via covalent binding to the cathepsin active site [40]. However, more recently it has been shown that E-64 can disassociate from cathepsins during the zymography process, which could allow an inhibited cathepsin to be reactivated in the zymogram, leading to a "false positive" level of activity [39].

The purpose of our E-64 treatment was to inhibit extracellular cathepsin proteases to reduce collagen digestion and reduce tendon degeneration. The zymography process requires the complete breakdown of extracellular matrix proteins and lysis of tenocytes and any other associated cells and consequently cannot distinguish intracellular or extracellular active proteases. The dosage of our E-64 treatment (both in soluble and microparticle form) were below levels required to trigger endocytosis of E-64 [190] and therefore intracellular cathepsin proteases would be unaffected. However, preservation of tendon structure in the presence of high levels of active cathepsin proteases would

indicate that the amount of extracellular cathepsin proteases was reduced and our treatment served its purpose. Thus, performing histology and immunohistochemistry would be required to better determine the location of the upregulated active proteases. Overall, the proteolytic network is incredibly complex and further analysis would be required to draw any concrete conclusions about the effect of sustained release of E-64 the preservation of supraspinatus tendon after injury and its effect on the proteolytic network of our rat model of massive rotator cuff tear.

Lastly, the zymography analysis was performed on rats that had been given an injection and allowed to recover and survive for 1 week after injury. It is possible the E-64 loaded microparticles did not remain in the tendon in every rat for the entire 1 week after injury and treatment. This is further supported by the large variability seen in the *in vivo* release of tagged E-64 and suggests that the high variability between animals treated with E-64 loaded microparticles could be due to differences in microparticle localization over time.

6.3 Future Directions

The research in this dissertation contributes foundational knowledge to develop therapeutic strategies to halt joint tissue degeneration after rotator cuff tear and potentially improve surgical outcomes following tendon re-attachment surgery. The results of Aim 1 (chapter 3) verified that our rat model of massive rotator cuff tear could mimic late-stage degeneration seen in humans including collagen disorganization in tendon, significant atrophy and fibrous infiltration in muscle, and osteoarthritic changes to humeral head cartilage. Additionally, this work provided foundational knowledge of

the temporal and spatial regulation of two important families of proteases after rotator cuff tear. This information allows for the development of targeted treatments that treat specific proteases at the location and time that they are detrimental to tissue health and integrity. There are many diseases that could benefit from a better understanding of the temporal and spatial regulation of dysregulated proteases for targeted therapeutic intervention. Cathepsins have been implicated in several diseases including arthritis, osteoporosis, atherosclerosis, obesity, tendinopathy and cancer [14,16,39,69,109]. Similarly, prolonged upregulation of active MMPs have been implicated in several diseases including cancer, nephritis, fibrosis, tendinopathy, osteoarthritis, muscle atrophy [110,122–126,193]. We have demonstrated that there is potentially crosstalk between the cathepsin and MMP families of proteases and previous work has shown that cathepsins have the ability to cleave and activate proMMPs [31]. Thus, it will be important to investigate combination inhibitory treatments that would treat both cathepsins and MMPs. Specifically in the supraspinatus tendon of our rat model of rotator cuff tear, an ideal treatment would involve sustained release of cathepsin inhibitors over at least one week and sustained release of MMP inhibitors over at least 3 weeks. With our novel microfluidic device platform, we can synthesize two different types of microparticles for a combination treatment to target upregulated cathepsin and MMP proteases in our rat model of rotator cuff tear.

In chapter 4 (Aim 2) of this dissertation work we developed a novel microfluidic device and outlined the redevelopment of a fluorogenic substrate assay for the detection of E-64. We demonstrated that our novel microfluidic device platform can fabricate uniformly sized microparticles with a diameter between 25 and 400 μm, which is wider

than size ranges accomplished with other microfluidic devices [26,156]. Additionally, we showed that we could incorporate DTT into our microparticle network to allow for hydrolytic degradation of the PEGDA network, in order to prevent a negative response such as foreign body giant cells and fibrous encapsulation, which may otherwise hinder mobility of the shoulder joint [194]. Furthermore, we showed that our novel microfluidic device has the ability to incorporate additional biomolecules directly into the microparticle network without additional steps. We used heparin as a model biomolecule, but heparin has been used been extensively used in biomaterials for the purpose of protein sequestration, protein release, protein conformation protection, and maintenance of protein bioactivity [19,20,35–37,153]. Most important to this dissertation work and essential for chapter 5 (Aim 3) was the verification that small molecule broad cathepsin inhibitor E-64 could be pre-loaded into the discontinuous phase of our novel microfluidic device and be incorporated into resulting microparticles. We confirmed that E-64 was loaded into microparticles and remained bioactive over at least 14 days. We also demonstrated that we could tune E-64 release based on polymer weight percentage, DTT concentration, and initial loading.

To expand potential uses of our novel microfluidic device system, we will investigate the upper limits of DTT incorporation into our PEGDA-based microparticles. We will do this by testing increasing amounts of DTT in our discontinuous phase until microparticles can no longer be formed by our microfluidic device. We will subsequently perform a degradation study to determine how quickly our PEG-based microparticles degrade relative to DTT concentration. Lastly, we will investigate how microparticles with higher amounts of DTT incorporation and therefore faster degradation modulate E-

64 release. The advantage of having a broader range of microparticle degradability is that it provides another lever for modification that similarly broadens potential uses of our microfluidic device.

Overall, our novel microfluidic device platform has practical applications in a variety of fields including drug delivery and tissue engineering. Additionally, the microfluidic device platform can be modified for increasingly complex microparticle fabrication. For example, heparin microparticles can be fabricated and loaded into the discontinuous phase with PEGDA polymer for encapsulation to create a core-shell microparticle, which our laboratory has done previously with older methods [37]. An advantage of using the microfluidic device system is more uniform fabrication of microparticles and faster time to completion. Other groups have also made increasingly complex microfluidic devices. One group used a microfluidic device to fabricate microparticles with a hollow core and demonstrated pH dependent release of two different cancer drugs [195]. Additionally, another group has created a microfluidic device in series to fabricate triple emulsions, whereby three microparticles can be encapsulated within one larger particle for a sustained of therapeutic drugs or simultaneous delivery of multiple therapeutic drugs [196].

Our novel microfluidic device is not limited to cathepsin inhibition via E-64 release. This platform can also be applied to treat other diseases characterized by dysregulated cathepsins including rheumatoid arthritis, osteoarthritis of the knee, and osteoporosis of the spine [13,16,131]. However, the tunability of E-64 release would be specific to this particular design and may not necessarily match trends with other therapeutic molecules. The addition of any additional biomolecules could cause a

significant difference in degradation time and release profile. For example, based on our work in chapter 3 (Aim 1) we are also interested in investigating the compatibility of broad MMP inhibitor, TIMP-3 with our novel microfluidic device system. We would not expect negatively charged heparin containing microparticles loaded with positively charged, broad MMP inhibitor TIMP-3 to be identical to trends seen with E-64 because the microparticle design is different and TIMP-3 is a protein, not a small molecule. Furthermore, the release profiles will also be affected by electrostatic interactions between negatively charged heparin and positively charged TIMP-3 (isoelectric point ~ 9.04) [197]. E-64 did not have an electrostatic attraction to any microparticle component in this work studies. Essentially, our work with E-64 provides a guideline of test parameters that may have an effect on therapeutic release. This would provide a starting point for others who are interested in utilizing our novel microfluidic device platform for drug delivery.

Additionally, potential uses of our novel microfluidic device can be expanded to include the use of other biomolecules, crosslinkers, or even encapsulated cells for other therapeutic purposes. Other biomolecules of interest that can be included into our microparticle network include the integrin binding recognition sequences RGD and GFOGER [21,140]. The addition of these integrin binding peptides would expand the use of our novel microfluidic device to include the ability to fabricate microparticles with encapsulated cells. Of particular interest to our laboratory is the encapsulation and delivery of mesenchymal stem cells (MSCs) for *in vivo* delivery. MSCs have been shown to have the ability to modulate inflammation by secretion of various paracrine factors (their secretome) [198]. Additionally, the Garcia laboratory has previously shown that

they could encapsulate human islet cells in PEG-based microparticles containing RGD peptides and fabricated with a microfluidic device [156]. Moreover, our novel microfluidic device should have the capacity to covalently incorporate both therapeutic proteins and protease degradable crosslinkers for on-demand treatment of dysregulated proteases. The Garcia laboratory has previously shown that they can covalently incorporate VPM (protease-sensitive crosslinker) in a PEG-based microparticle fabricated with a microfluidic device [199].

Overall, the main advantages of our novel microfluidic system are the ability to customize the resulting microparticles, reduced number of steps (which saves fabrication time), and all components added to the discontinuous phase will be incorporated into microparticles (which reduces material waste). Our novel microfluidic device has the potential to fabricate uniformly sized microparticles of various sizes, incorporate biomolecules and crosslinkers, load and release therapeutic molecules, encapsulate cells for therapeutic use, is economically priced, and easy to construct and use, which would make it widely available to those who wish to use it.

In addition to developing a novel microfluidic device platform, we also outlined the redevelopment of a currently available fluorogenic substrate assay to detect and quantify E-64 in solution. E-64 is an inexpensive, broad cathepsin inhibitor and its therapeutic use had previously been limited to soluble injections due to the inability to quantify E-64 release *in* vitro from biomaterial carriers. Presently, with the redevelopment of the DQ gelatin fluorogenic substrate assay, E-64 use can be broadened to include its use with biomaterial vehicles. Furthermore, our methods of how we identified and developed the DQ gelatin fluorogenic substrate assay as opposed to the Z-

FR-AMC fluorogenic substrate assays demonstrates a potential workflow to help others develop assays for therapeutic molecules that are also limited by *in vitro* detection and quantification. Overall, we demonstrated that not all assays and proteases respond equally and biomaterial carriers may interfere with the detection method. Thus, it is vital that others who are interested in using similar methods perform these same assessments.

Finally, in chapter 5 (Aim 3) of this dissertation work we used the supraspinatus tendon as a model tissue to probe the proteolytic network in our rat model of massive rotator cuff tear. We were able to consistently inject microparticles in the proximal third of the supraspinatus tendon. However, our protocol could be further improved by adding ultrasound imaging to our injection protocol. The Soslowsky laboratory has previously used ultrasound imaging to perform dry needling procedures on rat supraspinatus tendons without performing an open surgery [191]. The use of ultrasound imaging could be used to guarantee injection in the length of supraspinatus tendon for treatment throughout the tendon tissue. Additionally, the ultrasound imaging protocol could also be used for precise injection and treatment into the most proximal portion of the supraspinatus muscle. It has been shown that the supraspinatus muscle undergoes degenerative changes asymmetrically, such that the muscle closest to the tendon and humeral head insertion will develop degenerative changes first and propagate to the more medial portions over time [192]. Lastly, the addition of ultrasound imaging would allow for repeated injections into the supraspinatus tendon or muscle because we would not be required to re-open up the animal.

We found treatment with E-64 in soluble form and loaded into microparticles did not cause a significant decrease in active cathepsin L or MMP-2 levels compared to

injury alone. However, our rat model of massive rotator cuff tear is still a valuable platform to explore the proteolytic network. Ideally, we could develop a combination treatment of inhibitor loaded microparticles in order to treat each joint tissue (supraspinatus tendon, supraspinatus muscle, and humeral head cartilage) with cathepsin and/or MMP inhibitors as dictated by Aim 1 with microparticles fabricated using our novel microfluidic device outlined in Aim 2. This study would determine if localized sustained release of protease inhibitors could reduce joint tissue degeneration after rotator cuff tear, which could be used as therapeutic treatment to ultimately improve surgical reattachment outcomes. Furthermore, this large study would provide more information on the role that proteases play in joint tissue degeneration following rotator cuff tear.

Additionally, our animal model can be used to probe the complexities of the proteolytic network. Previous work has found that treatment with E-64 resulted in a significant decrease in active cathepsin L levels in cancer cells but paradoxically elevated levels of cathepsin S [38]. This highlights the fact that the proteolytic network is incredibly complex and cannot be expected to adhere to deductive reasoning and must be probed and investigated in order to develop therapies with desirable outcomes, such has joint tissue preservation. Furthermore, our rat model of massive rotator cuff tear is also a model of acute inflammation. To better understand the protease contribution between resident cells and infiltrating inflammatory cells, we could also incorporate treatment with clodronate liposomes, which deplete macrophages and neutrophils [172,199]. Following clodronate liposome treatment, the only source of proteases should be resident cells. Thus, we hypothesize that clodronate liposome treatment will cause a decrease in upregulated protease amounts (cathepsins and MMPs) due to the elimination of a

protease source. However, based on the documented complexity of the proteolytic network, it would need to be tested.

Our rat model could also be used to study the effectiveness of our inhibitor-loaded microparticle treatments prior to surgical reattachment, which would more closely mimic the human condition. Specifically, we would induce massive rotator cuff tear injury in our rat model and simultaneously deliver localized inhibitor treatment. After sufficient time to allow significant degeneration to occur (relative to injury with no treatment), we would perform the reattachment surgery. This would allow us to assess the efficacy of our inhibitor treatment to prevent joint tissue degeneration prior to surgical reattachment and determine if the localized inhibitor treatment improved surgical outcomes.

Furthermore, the methods outlined in this dissertation can be used to develop animal models with other diseases characterized by dysregulated proteases including cancer, osteoporosis, and osteoarthritis. For example, the Guldberg laboratory developed a medial meniscal transection (MMT) rat model to induce osteoarthritic changes to knee cartilage after 3 weeks. This model has demonstrated consistent defects in the medial third of cartilage in a rat model of osteoarthritis[161]. Additionally, mouse models of osteoarthritis have demonstrated osteoarthritic severity in the knees to correlate to cathepsin K concentration [158]. Additionally, MMP-2, -9, and -13 have been shown to be more active in osteoarthritic cartilage compared to healthy cartilage in both humans and rats [124,125]. In this example, following investigation of active proteases temporally via multiplex gelatin zymography, we could use our novel microfluidic device to fabricate microparticles to sustain inhibition of upregulated proteases within knee cartilage.

APPENDIX A: TROUBLESHOOTING CYSTATIN C RELEASE FROM NOVEL MICROFLUIDIC DEVICE

A.1. Cystatin C Release From Novel Microfluidic Device

Introduction: Cystatin C is the endogenous inhibitor of the cysteine cathepsin family of proteases [11]. It is produced by almost every nucleated cell in the body for the purposes of inhibiting upregulated extracellular proteases [109]. Thus, we initially investigated cystatin C release from our novel microfluidic device for subsequent use in Aim 3 of this work.

Methods: The microfluidic device was fabricated as described previously in Chapter 4.2. The discontinuous phase consisted of PEGDA, DTT, and L0290 photoinitiator (TCI). The L0290 photoinitiator was dissolved in phosphate buffered saline (PBS) to a final concentration of 20 mg/mL. PEGDA and DTT were resuspended in L0290 photoinitiator and allowed to incubate at 37 °C for 30 minutes in the absence of light to allow for Michael Type addition crosslinking. Following this incubation, heparin was added to the polymer solution and incubated for 30 minutes at 37 °C. Subsequently, 500 µg of Cystatin C (BBI) was added to the polymer solution and incubated at 37 °C in the absence of light for an additional 30 minutes. The polymer solution was loaded into a 1 mL syringe (Hamilton) and covered in foil to prevent light exposure and premature crosslinking. Resulting microparticles were washed, placed in 1.7 mL lowing binding tubes, and put on rotor at 37 °C. To determine cystatin C release, microparticles were centrifuged and supernatant was collected and stored at -20 °C. The supernatant was

replaced with an equal volume of ammonium bicarbonate buffer. Supernatant samples were tested for cystatin C release using ELISA (R&D Systems).

Results: After 10 days of release, we calculated that 12.6 ± 2.1 ng/mL of cystatin C had been released, which was 2.5% of what was originally loaded into the discontinuous phase.

Discussion: Cystatin C is able to be loaded into microparticles fabricated with our novel microfluidic device platform. However, based on the zymography results in Aim 1, to achieve a molar ratio of 1:1 with cathepsin L in supraspinatus tendon 150 μg (150,000 ng) of cystatin C is required to be released from our microparticles over 7 days. Thus, our system was unable to release relevant levels of cystatin C.

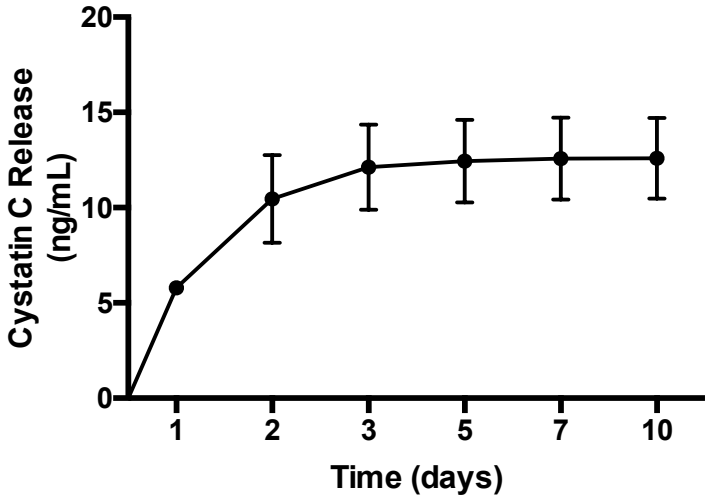

Figure A.1: Cystatin C was released from microparticles fabricated with our novel microfluidic device. Cumulative release of cystatin C equaled 12.6 ± 2.1 ng/mL, which is approximately 2.5% of the initial 500 μm loaded into the discontinuous phase. N=3.

A.2. Compare Cystatin C Release From Injected Hydrogel And Novel Microfluidic Device

Methods: The microfluidic device was fabricated as described above in Appendix A.1. The microfluidic device was allowed to run until half of the polymer solution was remaining in the discontinuous phase syringe. The syringe containing the discontinuous phase was injected into 50 μm hydrogel molds and crosslinked under UV light for 10 minutes. Resulting microparticles were washed, placed in 1.7 mL lowing binding tubes, and put on rotor at 37 °C. Resulting hydrogels were placed in 1.7 mL lowing binding tubes, and put on rotor at 37 °C. To determine cystatin C release from microparticles, they were centrifuged and supernatant was collected and stored at -20 °C. To determine cystatin C release from hydrogels, the supernatant was collected and stored at -20 °C. The supernatant was replaced with an equal volume of ammonium bicarbonate buffer all 1.7

mL low binding tubes. Supernatant samples were tested for cystatin C release using ELISA (R&D Systems).

Results: After 5 days of release, we calculated that microparticles had released 0.00393 ± 0.00375 ng/mL of cystatin C, while hydrogels released 0.130 ± 0.226 ng/mL of cystatin C.

Discussion: The lack of cystatin C from hydrogels indicated to us that the majority of cystatin C added to the discontinuous phase was not entering the microfluidic device, which would explain why resulting microparticles released very little cystatin C. This suggested that cystatin C was remaining inside the syringe.

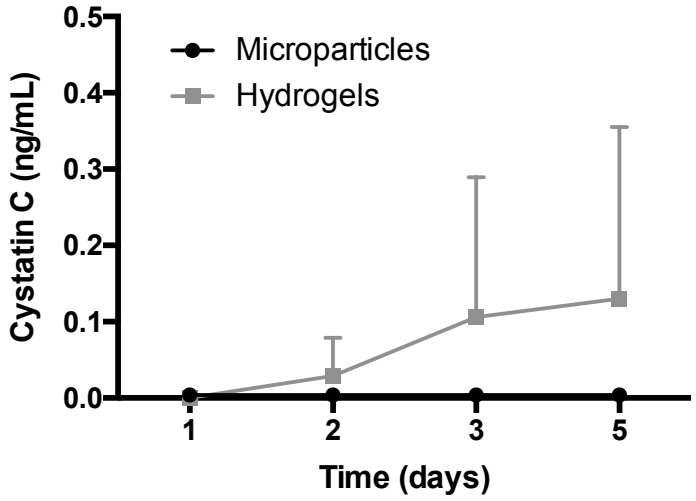

Figure A.2: Very low levels of cystatin C was released from hydrogels injected into molds with the syringe used in our novel microfluidic device platform. Cumulative release of cystatin C from our microparticles equaled 0.00393 ± 0.00375 ng/mL. Cumulative release of cystatin C from hydrogels equaled 0.130 ± 0.226 ng/mL. N=3/group.

A.3. Cystatin C Location Test

Methods: Cystatin C was fluorescently tagged with AlexaFluor633 (AF633, Invitrogen). Cystatin C was dissolved in 0.1 M Na_2HPO_4 solution (pH = 6) at a 10 mg/mL concentration and reacted with 10 mM EDC and 5.7 μM AF633 at room temperature for 90 minutes. Fluorescently tagged cystatin C was subsequently dialyzed for two days, freeze dried, and stored at -20 °C until use. The microfluidic device was fabricated and run as described above in Appendix A.2. Resulting microparticles and hydrogels were placed on a 96 well plate to determine if tagged cystatin C was incorporated into the network. Additionally, we tested the components of the microfluidic device and untagged cystatin C in order to distinguish any autofluorescence.

Results: All components tested demonstrated basal levels of fluorescence except the PBS that was used to rinse the syringe used in the discontinuous phase.

Discussion: This study demonstrated that cystatin C did in fact remain in the syringe used for the discontinuous phase of our microfluidic device. Thus, cystatin C was not compatible with our system. A limitation of this study is that it is possible the fluorescent tag is responsible for adsorption to the syringe. To answer this question in future studies, we could the same study with unbound AF633 dye.

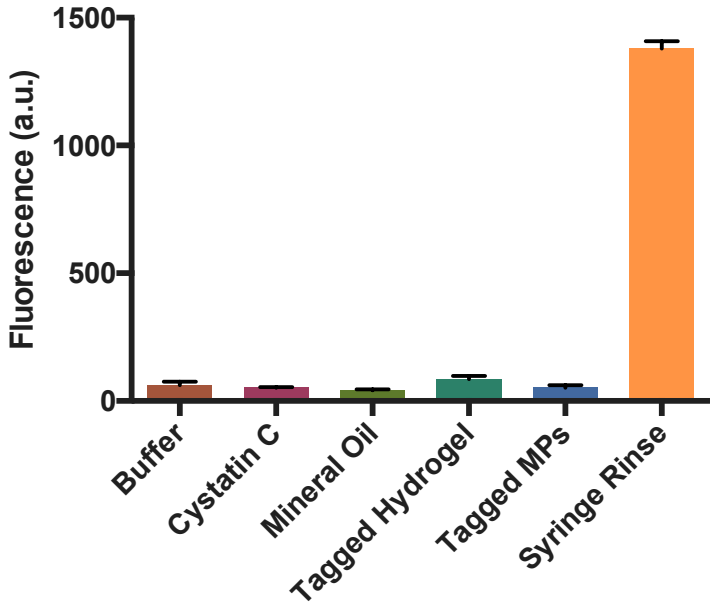

Figure A.3: Tagged cystatin C predominately remained inside the syringe used to inject the discontinuous phase of the microfluidic device platform. Detectable amounts of cystatin C was not incorporated into resulting microparticles or hydrogels. Cystatin C, ammonium bicarbonate buffer, and mineral oil do not auto-fluoresce. N=3.

APPENDIX B: EXAMPLE CALCULATION OF E-64 RELEASE WITH DQ GELATIN FLUOROGENIC SUBSTRATE ASSAY AND E-64 STANDARD CURVE

Methods: First, the DQ gelatin assay is run with undiluted supernatant samples with an E-64 standard curve (refer to section 4.2.6 for details). The supernatant samples that have a fluorescent intensity reading at or above the standard curve value at 500 ng/mL were used to calculate release immediately. Samples that had a fluorescent intensity below the standard curve value at 500 ng/mL were diluted and re-run. Next, we subtracted the blank from the standard curve values and supernatant sample values. All the data is compiled and input into GraphPad as shown in Figure B.1a. The standard curve values are then analyzed in GraphPad. Specifically, we hit Analyze → XY analyses → non-linear regression (curve fit) → exponential → one-phase decay. The results tab will show the values for Y0 (Y value when X is zero), P (plateau, the Y value at infinite time), and K (the rate constant) shown in Figure B.1b. These values are required for the one-phase decay equation shown in Figure B.1c. After determining how much E-64 was in the supernatant sample based on the curve fit, multiply any samples by their respective dilution factor. Be sure to keep in mind that supernatant samples that were re-run have their own E-64 standard curve. Using cumulative release, plot the E-64 release curve similar to the one shown in Figure B.1d.

A

		X	Group A		
		E-64 (ng/mL)	Cathepsin K Activity (with E-64 Std Curve)		
		X	A:Y1	A:Y2	A:Y3
1	Title	0.0	23870.5	30591	30250
2	Title	1.8	23243.0	29895	29507
3	Title	4.5	22453.0	27265	26844
4	Title	17.9	19926.0	17143	16908
5	Title	35.7	17253.0	12721	12394
6	Title	178.7	8406.0	6279	6208
7	Title	357.4	6270.0	4708	4667
8	Title	893.5	4303.0	3181	3022
9	Title	1787.1	3434.0	2306	2269

B

	Nonlin fit	A
		Cathepsin K Activity (with E-64 Std Curve)
		Y
1	One phase decay	
2	Best-fit values	
3	Y0	28238
4	Plateau	4531
5	K	0.02719

C

$$Y = (Y0 - P) * \exp(-K*X) + P$$

D

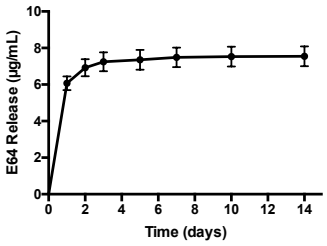

Figure B.1: Example Calculation of E-64 Release with DQ Gelatin Fluorogenic Substrate Assay and E-64 Standard Curve. (A) Screenshot of XY plot of Cathepsin K activity from E-64 standard curve (B) Screenshot of one-phase decay analysis (C) One-phase decay equation (D) Example cumulative release plot of E-64 loaded microparticles.

REFERENCES

1. Sher JS, Uribe JW, Posada A, Murphy BJ, Zlatkin MB, John MD, et al. Diagnosis of rotator cuff tears. J Bone Joint Surg Am. 1995;77(1):10–5.
2. Yadav H, Nho S, Romeo A, MacGillivray JD. Rotator cuff tears: Pathology and repair. Knee Surgery, Sport Traumatol Arthrosc. 2009;17(4):409–21.
3. Goutallier D, Postel JM, Bernageau J, Lavau L VM. Fatty muscle degeneration in cuff ruptures. Pre- and postoperative evaluation by CT scan. Clin Orthop Relat Res. 1994;304:78–83.
4. Kramer EJ, Bodendorfer BM, Laron D, Wong J, Kim HT, Liu X, et al. Evaluation of cartilage degeneration in a rat model of rotator cuff tear arthropathy. J Shoulder Elb Surg. 2013;22(12):1702–9.
5. Neer, C S; Craig, E V; Fukuda H. Cuff-tear arthropathy. J Bone Jt Surg. 1983;65(9):1232–44.
6. Galatz LM, Ball CM, Teefey SA, Middleton WD, Yamaguchi K. The Outcome and Repair Integrity of Completely Arthroscopically Repaired Large and Massive Rotator Cuff Tears. J Bone Jt Surg - Ser A. 2004;86(2):219–24.
7. Harryman D, Mack L, Wang K, Jackins S, Richardson M, Matsen F, et al. Correlation of Functional Results With Integrity of the Cuff. J Bone Jt Surg A. 2007;982–9.
8. Nozaki T, Tasaki A, Horiuchi S, Ochi J, Starkey J, Hara T, et al. Predicting retear after repair of full-thickness rotator cuff tear: Two-point dixon MR imaging quantification of fatty muscle degeneration-initial experience with 1-year follow-up. Radiology. 2016;280(2):500–9.
9. Brew K, Nagase H. The tissue inhibitors of metalloproteinases (TIMPs): An ancient family with structural and functional diversity. Biochim Biophys Acta. 2010;1803(1):55–71.
10. Kozawa E, Cheng XW, Urakawa H, Arai E, Yamada Y, Kitamura S, et al. Increased expression and activation of cathepsin K in human osteoarthritic cartilage and synovial tissues. J Orthop Res. 2016;34(1):127–34.
11. Turk V, Stoka V, Vasiljeva O, Renko M, Sun T, Turk B, et al. Cysteine cathepsins: From structure, function and regulation to new frontiers. BBA - Proteins Proteomics. 2012;1824:68–88.
12. Morris CA, Morris LD, Kennedy AR, Lee Sweeney H. Attenuation of skeletal muscle atrophy via protease inhibition. J Appl Physiol. 2005;99:1719–27.
13. Mort JS, Beaudry F, Th Eroux K, Emmott AA, Richard H, Fisher WD, et al. Early cathepsin K degradation of type II collagen in vitro and in vivo in articular cartilage. Osteoarthr Cartil. 2016;
14. Seto SP, Parks AN, Qiu Y, Soslowsky LJ, Karas S, Platt MO, et al. Cathepsins in Rotator Cuff Tendinopathy: Identification in Human Chronic Tears and Temporal Induction in a Rat Model. Ann Biomed Eng. 2015;43(9):2036–46.
15. Parks AN, McFaline-Figueroa J, Coogan A, Poe-Yamagata E, Guldberg RE, Platt MO, et al. Supraspinatus tendon overuse results in degenerative changes to tendon insertion region and adjacent humeral cartilage in a rat model. J Orthop Res. 2016;1–9.
16. Winer A, Adams S, Mignatti P. Matrix metalloproteinase inhibitors in cancer

therapy: Turning past failures in future successess. Expert Opin Investig Drugs. 2009;18(5):585–600.
17. Winer A, Adams S, Mignatti P. Matrix metalloproteinase inhibitors in cancer therapy: Turning past failures into future successes. Mol Cancer Ther. 2018;17(6):1147–55.
18. Yeo Y, Svensson C, Wen H, Jung H, Li X. Clinical and Commercial Translation of Drug Delivery Systems Drug Delivery Approaches in Addressing Clinical Pharmacology-Related Issues: Opportunities and Challenges.
19. Tellier L, Krieger J, Sellick A, Coogan A, Falis A, Rinker T, et al. Localized SDF-1 Delivery Increases Pro-Healing Bone Marrow-Derived Cells in the Supraspinatus Muscle Following Severe Rotator Cuff Injury. Regen Eng Transl Med. 2018;
20. Science B, Tellier LE, Treviño EA, Brimeyer AL, Reece DS, Willett NJ, et al. Intra-Articular TSG-6 Delivery from Heparin-based Microparticles Reduces Cartilage Damage in a Rat Model of Osteoarthritis.
21. Phelps EA, Enemchukwu NO, Fiore VF, Sy JC, Murthy N, Sulchek TA, et al. Maleimide cross-linked bioactive PEG hydrogel exhibits improved reaction kinetics and cross-linking for cell encapsulation and in situ delivery. Adv Mater. 2012;24(1):64–70.
22. Foster GA, Headen DM, González-García C, Salmerón-Sánchez M, Shirwan H, García AJ. Protease-degradable microgels for protein delivery for vascularization. Vol. 113, Biomaterials. 2017. p. 170–5.
23. Liu X, Manzano G, Kim HT, Feeley BT. A rat model of massive rotator cuff tears. J Orthop Res. 2011;29(4):588–95.
24. Ikemoto M, Nikawa T, Takeda I, Watanabe C, Kitano T, Baldwin KM, et al. Space shuttle flight (STS-90) enhances degradation of rat myosin heavy chain in association with activation of ubiquitin-proteasome pathway. FASEB J. 2001;
25. Selma J. The Role of Sphingolipid Metabolism in Sickle Bone Disease and Bone Stem Cells. Georgia Institute of Technology/Emory University; 2019.
26. Choi SW, Cheong IW, Kim JH, Xia Y. Preparation of uniform microspheres using a simple fluidic device and their crystallization into close-packed lattices. Small. 2009;5(4):454–9.
27. Baret JC. Surfactants in droplet-based microfluidics. Lab Chip. 2012;12(3):422–33.
28. Wang K, Lu YC, Xu JH, Luo GS. Determination of Dynamic Interfacial Tension and Its Effect on Droplet Formation in the T-Shaped Microdispersion Process.
29. Lin C-C, Anseth KS. PEG Hydrogels for the Controlled Release of Biomolecules in Regenerative Medicine. Expert Rev. 2009;26(3):631–43.
30. Trevino EA, McFaline-Figueroa J, Guldberg RE, Platt MO, Temenoff JS. Full-thickness rotator cuff tear in rat results in distinct temporal expression of multiple proteases in tendon muscle and cartilage.pdf. J Orthop Res. 2018;1–13.
31. Christensen J, Shastri VP. Matrix-metalloproteinase-9 is cleaved and activated by cathepsin K. BMC Res Notes. 2015;8(1):322.
32. Kumar A, Bhatnagar S, Kumar A. Matrix metalloproteinase inhibitor batimastat alleviates pathology and improves skeletal muscle function in dystrophin-deficient mdx mice. Am J Pathol. 2010;177(1):248–60.

33. Janusz MJ, Hookfin EB, Heitmeyer SA, Woessner JF, Freemont AJ, Hoyland JA, et al. Moderation of iodoacetate-induced experimental osteoarthritis in rats by matrix metalloproteinase inhibitors. Osteoarthr Cartil. 2001;9(8):751–60.
34. Vo N V., Hartman RA, Yurube T, Jacobs LJ, Sowa GA, Kang JD. Expression and regulation of metalloproteinases and their inhibitors in intervertebral disc aging and degeneration. Spine J. 2013;13(3):331–41.
35. Tellier LE, Miller T, Mcdevitt TC, Temenoff JS. Hydrolysis and sulfation pattern effects on release of bioactive bone morphogenetic protein-2 from heparin-based microparticles. J Mater Chem B. 2015;3(3):8001–9.
36. Peng Y, Tellier LE, Temenoff JS. Heparin-based hydrogels with tunable sulfation & degradation for anti-inflammatory small molecule delivery. Biomater Sci. 2016;4:1371.
37. Rinker TE, Philbrick BD, Temenoff JS, Coulter : W H, Author AB. Core-Shell Microparticles for Protein Sequestration and Controlled Release of a Protein-Laden Core HHS Public Access Author manuscript. Acta Biomater. 2017;56:91–101.
38. Wilder CL, Walton C, Watson V, Stewart FAA, Johnson J, Peyton SR, et al. Differential cathepsin responses to inhibitor-induced feedback: E-64 and cystatin C elevate active cathepsin S and suppress active cathepsin L in breast cancer cells. Int J Biochem Cell Biol. 2016;79:198–208.
39. Shockey WA, Kieslich CA, Wilder CL, Watson V, Platt MO, Coulter WH. Dynamic Model of Protease State and Inhibitor Trafficking to Predict Protease Activity in Breast Cancer Cells. Cell Mol Bioeng. 12.
40. Matsumoto K, Mizoue K, Kitamura K, Tse WC, Huber CP, Ishida T. Structural basis of inhibition of cysteine proteases by E-64 and its derivatives. Biopolym - Pept Sci Sect. 1999;51(1):99–107.
41. Wetlaufer DB. Ultraviolet Spectra of Proteins and Amino Acids. Adv Protein Chem. 1963;17(C):303–90.
42. Yoon JP, Chung SW, Jung JW, Lee YS, Kim K Il, Park GY, et al. Is a Local Administration of Parathyroid Hormone Effective to Tendon-to-Bone Healing in a Rat Rotator Cuff Repair Model? J Orthop Res. 2020;38(1):82–91.
43. Dolkart O, Chechik O, Zarfati Y, Brosh T, Alhajajra F, Maman E. A single dose of platelet-rich plasma improves the organization and strength of a surgically repaired rotator cuff tendon in rats. Arch Orthop Trauma Surg. 2014;134(9):1271–7.
44. Gilotra MN, Shorofsky MJ, Stein JA, Murthi AM. Healing of rotator cuff tendons using botulinum toxin A and immobilization in a rat model. BMC Musculoskelet Disord. 2016;17(1):1–8.
45. Maman E, Yehuda C, Pritsch T, Morag G, Brosh T, Sharfman Z, et al. Detrimental Effect of Repeated and Single Subacromial Corticosteroid Injections on the Intact and Injured Rotator Cuff. Am J Sports Med. 2016;44(1):177–82.
46. Llusa M, Meri A, Ruano D, Surgeons. AA of O. Surgical atlas of the musculoskeletal system. Rosemont, IL: American Academy of Orthopaedic Surgeons; 2008.
47. Huegel J, Williams AA, Soslowsky LJ. Rotator Cuff Biology and Biomechanics: a Review of Normal and Pathological Conditions. Curr Rheumatol Rep. 2015 Jan 5;17(1):476.

48. Dykyj D, Jules KT. The clinical anatomy of tendons. J Am Podiatr Med Assoc. 1991 Jul 1;81(7):358–65.
49. Tkocz C, Kühn K. The Formation of Triple-Helical Collagen Molecules from α1 or α2 Polypeptide Chains. Eur J Biochem. 2005;7(4):454–62.
50. Kastelic J, Galeski A, Baer E. The Multicomposite Structure of Tendon. Connect Tissue Res. 1978;6(1):11–23.
51. Raspanti M, Manelli A, Franchi M, Ruggeri A. The 3D Structure of Crimps in the Rat Achilles Tendon.
52. James R, Kesturu G, Balian G, Chhabra AB. Tendon: Biology, Biomechanics, Repair, Growth Factors, and Evolving Treatment Options. J Hand Surg Am. 2008;33(1):102–12.
53. Kannus P. Structure of the tendon connective tissue. Scand J Med Sci Sport. 2000 Dec 1;10(6):312–20.
54. Shahjahan M. Skeletal muscle development in vertebrate animals. Asian J Med Biol Res. 2015;1(2):139–48.
55. Celli T, Rovesta C, Marongiu MC, Manzieri S. Transplantation of teres maior muscle for infraspinatus muscle in irreparable rotator cuff tears.
56. Melis B, Defranco MJ, Lädermann A, Barthelemy R, Walch G. The teres minor muscle in rotator cuff tendon tears.
57. Hsu JE, Reuther KE, Sarver JJ, Lee CS, Thomas SJ, Glaser DL, et al. Restoration of anterior-posterior rotator cuff force balance improves shoulder function in a rat model of chronic massive tears. J Orthop Res. 2011 Jul 1;29(7):1028–33.
58. Fox AJS, Bedi A, Rodeo SA. The Basic Science of Articular Cartilage: Structure, Composition, and Function. 2009;
59. Ulrich-Vinther M, Maloney MD, Schwarz EM, Rosier R, O'Keefe RJ. Articular Cartilage Biology. JAAOS - J Am Acad Orthop Surg. 2003;11(6).
60. Murrell AC, Walton JR. Diagnosis of rotator cuff tears. Lancet. 2001;357(9258):769–70.
61. Rothrauff BB, Pauyo T, Debski RE, Rodosky MW, Tuan R, Musahl V. The Rotator Cuff Organ: Integrating Developmental Biology, Tissue Engineering, and Surgical Considerations to Treat Chronic Massive Rotator Cuff Tears. Tissue Eng Part B Rev. 2017;23(4):318–35.
62. Maeda E, Fleischmann C, Mein CA, Shelton JC, Bader DL, Lee DA. Functional analysis of tenocytes gene expression in tendon fascicles subjected to cyclic tensile strain Functional analysis of tenocytes gene expression in tendon fascicles. Connect Tissue Res. 2010;51:434–44.
63. Arnoczky SP, Lavagnino M, Egerbacher M. The mechanobiological aetiopathogenesis of tendinopathy: is it the over-stimulation or the under-stimulation of tendon cells? Int J Exp Pathol. 2007 Aug;88:217–26.
64. Magnusson SP, Langberg H, Kjaer M. The pathogenesis of tendinopathy: Balancing the response to loading. Nat Rev Rheumatol. 2010;6(5):262–8.
65. Reuther KE, Thomas SJ, Sarver JJ, Tucker JJ, Lee C-S, Gray CF, et al. Effect of return to overuse activity following an isolated supraspinatus tendon tear on adjacent intact tendons and glenoid cartilage in a rat model. J Orthop Res. 2013 May 1;31(5):710–5.
66. Thomopoulos S, Parks WC, Rifkin DB, Derwin KA. Mechanisms of tendon injury

and repair. J Orthop Res. 2015;33(6):832–9.
67. Punturieri A, Filippov S, Allen E, Caras I, Murray R, Reddy V, et al. Regulation of Elastinolytic Cysteine Proteinase Activity in Normal and Cathepsin K–deficient Human Macrophages. J Exp Med. 2000;196(6):789–99.
68. Starkey PM, Barrett AJ, Burleigh MC. The degradation of articular collagen by neutrophil proteinases. Biochim Biophys Acta - Enzymol. 1977 Aug 11;483(2):386–97.
69. Wilder CL, Park K-Y, Keegan PM, Platt MO, Coulter WH. Manipulating substrate and pH in zymography protocols selectively distinguishes cathepsins K, L, S, and V activity in cells and tissues. Arch Biochem Biophys. 2011;516:52–7.
70. Thomazeau H, Rolland Y, Lucas C, Duval J-M, Langlais F. Atrophy of the supraspinatus belly Assessment by MRI in 55 patients with rotator cuff pathology. 2009;
71. Gerber C, Meyer DC, Schneeberger AG, Hoppeler H, Von Rechenberg B. Effect of tendon release and delayed repair on the structure of the muscles of the rotator cuff: An experimental study in sheep. J Bone Jt Surg - Ser A. 2004;86(9):1973–82.
72. Fabis J, Danilewicz M, Omulecka A. Rabbit supraspinatus tendon detachment: Effects of size and time after tenotomy on morphometric changes in the muscle. Acta Orthop Scand. 2001;72(3):282–6.
73. Hsu HC, Luo ZP, Stone JJ, Huang TH, An KN. Correlation between rotator cuff tear and glenohumeral degeneration. Acta Orthop Scand. 2003;74(1):89–94.
74. Dakin SG, Martinez FO, Yapp C, Wells G, Oppermann U, Dean BJF, et al. Inflammation activation and resolution in human tendon disease. Sci Transl Med. 2015;7(311):1–13.
75. Colvin AC, Egorova N, Harrison AK, Moskowitz A, Flatow EL. National Trends in Rotator Cuff Repair. J Bone Jt Surg. 2012;94:227–33.
76. Oh JH, Kim SH, Ji HM, Jo KH, Bin SW, Gong HS. Prognostic Factors Affecting Anatomic Outcome of Rotator Cuff Repair and Correlation With Functional Outcome. Arthrosc - J Arthrosc Relat Surg. 2009;25(1):30–9.
77. Le BTN, Wu XL, Lam PH, Murrell GAC. Factors Predicting Rotator Cuff Re-Tear: An Analysis of 1000 Consecutive Rotator Cuff Repairs. J Shoulder Elb Surg. 2013;22(10).
78. Barry JJ, Lansdown DA, Cheung S, Feeley BT, Ma CB. The relationship between tear severity, fatty infiltration, and muscle atrophy in the supraspinatus. J Shoulder Elb Surg. 2013;21(1128).
79. Cummins CA, Murrell GAC. Mode of failure for rotator cuff repair with suture anchors identified at revision surgery. J Shoulder Elb Surg. 2003;12(2):128–33.
80. Ditsios K, Agathangelidis F, Boutsiadis A, Karataglis D, Papadopoulos P. Long Head of the Biceps Pathology Combined with Rotator Cuff Tears. Orthopedics. 2012;2012.
81. Thomas SJ, Reuther KE, Tucker JJ, Sarver JJ, Yannascoli SM, Caro AC, et al. Biceps detachment decreases joint damage in a rotator cuff tear rat model. Clin Orthop Relat Res. 2014;472(8):2404–12.
82. Gladstone JN, Bishop JY, Lo IKY, Flatow EL. Fatty Infiltration and Atrophy of the Rotator Cuff Do Not Improve After Rotator Cuff Repair and. Sport Med. 2007;719–28.

83. Miller RM, Popchak A, Vyas D, Tashman S, Irrgang JJ, Musahl V, et al. Effects of exercise therapy for the treatment of symptomatic full-thickness supraspinatus tears on in vivo glenohumeral kinematics. J Shoulder Elb Surg. 2016;25(4):641–9.
84. Keener JD, Galatz LM, Teefey SA, Middleton WD, Steger-May K, Stobbs-Cucchi G, et al. A Prospective Evaluation of Survivorship of Asymptomatic Degenerative Rotator Cuff Tears. J Bone Jt Surg. 2015;97:89–98.
85. Moosmayer S, Tariq R, Stiris M, Smith H-J. The Natural History of Asymptomatic Rotator Cuff Tears: A Three-Year Follow-up of Fifty Cases. J Bone Jt Surg. 2013;95:1249–55.
86. Soslowsky LJ, Thomopoulos S, Tun S, Flanagan CL, Keefer CC, Mastaw J, et al. Overuse activity injures the supraspinatus tendon in an animal model: A histologic and biomechanical study. J Shoulder Elb Surg. 2000;9(2):79–84.
87. Reuther KE, Sarver JJ, Schultz SM, Lee CS, Sehgal CM, Glaser DL, et al. Glenoid cartilage mechanical properties decrease after rotator cuff tears in a rat model. J Orthop Res. 2012;30(9):1435–9.
88. Liu X, Laron D, Natsuhara K, Manzano G, Kim HT, Feeley BT, et al. A mouse model of massive rotator cuff tears. J Bone Jt Surg - Ser A. 2012;94(7):e41.
89. Samagh SP, Kramer EJ, Melkus G, Laron D, Bodendorfer BM, Natsuhara K, et al. MRI quantification of fatty infiltration and muscle atrophy in a mouse model of rotator cuff tears. J Orthop Res. 2013 Mar;31(3):421–6.
90. Frey E, Regenfelder F, Sussmann P, Zumstein M, Gerber C, Born W, et al. Adipogenic and myogenic gene expression in rotator cuff muscle of the sheep after tendon tear. J Orthop Res. 2009;27(4):504–9.
91. Gerber C, Meyer DC, Flü ck M, Benn MC, von Rechenberg B, Wieser K. Anabolic Steroids Reduce Muscle Degeneration Associated With Rotator Cuff Tendon Release in Sheep. Am J Sports Med. 2015;43(10):2393–400.
92. Friel NA, McNickle AG, Defranco MJ, Wang F, Shewman EF, Verma NN, et al. Effect of highly purified capsaicin on articular cartilage and rotator cuff tendon healing: An in vivo rabbit study. J Orthop Res. 2015;33(12):1854–60.
93. Gupta R, Lee TQ. Contributions of the different rabbit models to our understanding of rotator cuff pathology. J Shoulder Elb Surg. 2007;16(5 SUPPL.):149–57.
94. Soslowsky LJ, Carpenter JE, Debano CM, Banerji I, Moalli MR. Development and use of an animal model for investigations on rotator cuff disease. J Shoulder. 1996;5(5):383–92.
95. Reuther KE, Thomas SJ, Tucker JJ, Sarver JJ, Gray CF, Evans EB, et al. Returning to overuse activity following a combined supraspinatus and infraspinatus tear leads to shoulder joint damage. ASME 2013 Summer Bioeng Conf SBC 2013. 2013;1 B:1818–24.
96. Galatz LM, Rothermich SY, Zaegel M, Silva MJ, Havlioglu N, Thomopoulos S. Delayed repair of tendon to bone injuries leads to decreased biomechanical properties and bone loss. J Orthop Res. 2005;23(6):1441–7.
97. Lebaschi AH, Deng XH, Camp CL, Zong J, Cong GT, Carballo CB, et al. Biomechanical, Histologic, and Molecular Evaluation of Tendon Healing in a New Murine Model of Rotator Cuff Repair. J Arthrosc Relat Surg. 2018;34(4):1173–83.
98. Joshi SK, Liu X, Samagh SP, Lovett DH, Bodine SC, Kim HT, et al. MTOR

regulates fatty infiltration through SREBP-1 and PPAR-gamma after a combined massive rotator cuff tear and suprascapular nerve injury in rats. J Orthop Res. 2013;31(5):724–30.
99. Lake SP, Ansorge HL, Soslowsky LJ. Animal models of tendinopathy Animal models of tendinopathy. Disabil Rehabil. 2009;30:1530–41.
100. Gimbel JA, Van Kleunen JP, Mehta S, Perry SM, Williams GR, Soslowsky LJ. Supraspinatus tendon organizational and mechanical properties in a chronic rotator cuff tear animal model. J Biomech. 2004;37(5):739–49.
101. Perry SM, Getz CL, Soslowsky LJ. After rotator cuff tears, the remaining (intact) tendons are mechanically altered. J Shoulder Elb Surg. 2009;18:52–7.
102. Codman E, Akerson IB. The Pathology Associated With Rupture Of The Supraspinatus Tendon. Ann Surg. 1931;93(1):348–59.
103. Melis B, Defranco MJ, Chuinard C, Walch G. Natural History of Fatty Infiltration and Atrophy of the Supraspinatus Muscle in Rotator Cuff Tears. Clin Orthop Relat Res. 2010;468:1498–505.
104. Garnero P, Borel O, Byrjalsen I, Ferreras M, Drakeţ FH, Mcqueneyţ MS, et al. The Collagenolytic Activity of Cathepsin K Is Unique among Mammalian Proteinases. J Biol Chem. 1998;273(48):32347–52.
105. Yasuda Y, Li Z, Greenbaum D, Bogyo M, Weber E, Brö D. Cathepsin V, a Novel and Potent Elastolytic Activity Expressed in Activated Macrophages. J Biol Chem. 2004;279(35):36761–70.
106. Berglund ME, Hart DA, Reno C, Wiig M. Growth factor and protease expression during different phases of healing after rabbit deep flexor tendon repair. J Orthop Res. 2011;29(6):886–92.
107. Oliva F, Grasso A, Barisani D, Maffulli N. Gene Expression Analysis In Calcific Tendinopathy Of The Rotator Cuff. Eur Cells Mater. 2011;21:548–57.
108. Maciewicz RA, Etherington DJ. A comparison of four cathepsins (B, L, N and S) with collagenolytic activity from rabbit spleen. Biochem J. 1988;256(2):433–40.
109. Manu O. Platt WAS. Endothelial cells and cathepsins: Biochemical and biomechanical regulation. Biochimie. 2015;314–23.
110. Deval C, Mordier S, Obled C, Bechet D, Combaret L, Attaix D, et al. Identification of cathepsin L as a differentially expressed message associated with skeletal muscle wasting. Biochem J. 2001;360:143–50.
111. Han J, Chan BMC, Kim SO, Ha S-D, Martins A, Khazaie K. Membrane in Macrophages-Containing Vesicles to the Plasma α TNF-Cathepsin B Is Involved in the Trafficking of. J Immunol. 2008;181:690–7.
112. Mcqueney MS, Amegadzie BY, D 'alessio K, Hanning CR, Mclaughlin MM, Mcnulty D, et al. Autocatalytic Activation of Human Cathepsin K. J Biol Chem. 1997;272(21):13955–60.
113. Hall A, Ekiel I, Mason RW, Kasprzykowski F, Grubb A, Abrahamson M. Structural Basis for Different Inhibitory Specificities of Human Cystatins C and D. Biochemistry. 1998;37:4071–9.
114. Warfel AH, Zucker-Franklin D, Frangione B, Ghiso J. Constitutive Secretion Of Cystatin C (Y-Trace) By Monocytes And Macrophages And Its Downregulation After Stimulation. Br Defin Rep. 1987;166:1912–7.
115. Tsai CH, Yang SF, Huang FM, Chang YC. The upregulation of cystatin C in

human gingival fibroblasts stimulated with cyclosporine A. J Periodontal Res. 2009;44(4):459–64.
116. Page-Mccaw A, Ewald AJ, Werb Z. Matrix metalloproteinases and the regulation of tissue remodelling. Nat Rev | Mol CELL Biol. 2007;8:221–33.
117. Nagase H, Woessner JF. Matrix Metalloproteinases. J Biol Chem. 1999;274(31):21491–4.
118. Fanjul-Fernández M, Folgueras AR, Cabrera S, López-Otín C. Matrix metalloproteinases: Evolution, gene regulation and functional analysis in mouse models. BBA - Mol Cell Res. 2009;1803:3–19.
119. Chakraborti S, Mandal M, Das S, Mandal A, Chakraborti T. Regulation of matrix metalloproteinases: An overview. Mol Cell Biochem. 2003;253:269–85.
120. Overall CM. Molecular determinants of metalloproteinase substrate specificity: matrix metalloproteinase substrate binding domains, modules, and exosites. Mol Biol. 2002;22:51–86.
121. Stracke JO, Hutton M, Stewart M, Pendas AM, Smith B, Lopez-Otin C, et al. Biochemical Characterization of the Catalytic Domain of Human Matrix Metalloproteinase 19: Evidence For A Role As A Potent Basement Membrane Degrading Enzyme. J Biol Chem. 2000;275(20):14809–16.
122. Riley GP, Curry V, Degroot J, Van El B, Verzijl N, Hazleman BL, et al. Matrix metalloproteinase activities and their relationship with collagen remodelling in tendon pathology. Matrix Biol. 2002;21:185–95.
123. Yoshihara Y, Hamada K, Nakajima T, Fujikawa K, Fukuda H. Biochemical markers in the synovial fluid of glenohumeral joints from patients with rotator cuff tear. J Orthop Res Off Publ Orthop Res Soc. 2001;19(4):573–9.
124. Jackson MT, Moradi B, Smith MM, Jackson CJ, Little CB. Activation of Matrix Metalloproteinases 2, 9, and 13 by Activated Protein C in Human Osteoarthritic Cartilage Chondrocytes. Arthritis Rheumatol. 2014;66(6):1525–36.
125. Beckett J, Jin W, Schultz M, Chen A, Tolbert D, Moed BR, et al. Excessive running induces cartilage degeneration in knee joints and alters gait of rats. J Orthop Res. 2012;30(10):1604–10.
126. Reznick AZ, Menashe O, Bar-Shai M, Coleman R, Carmeli E. Expression of matrix metalloproteinases, inhibitor, and acid phosphatase in muscles of immobilized hindlimbs of rats. Muscle and Nerve. 2003;27(1):51–9.
127. Kolb C, Mauch S, Peter H-H, Krawinkel U, Sedlacek R. The matrix metal-loproteinase RASI-1 is expressed in synovial blood vessels of a rheumatoid arthritis patient. Immunol Lett. 1997;57:83–8.
128. Shapiro SD, Kobayashi DK, Ley TJ. Cloning and Characterization of a Unique Elastolytic Metalloproteinase Produced by Human Alveolar Macrophages*. J Biol Chem. 1993;268(32):4664–71.
129. Hou P, Troen T, Ovejero MC, Kirkegaard T, Andersen TL, Byrjalsen I, et al. Matrix metalloproteinase- 12 (MMP-12) in osteoclasts- new lesson on the involvement of MMPs in bone resorption. Bone. 2004;34:37–47.
130. Pasternak B, Aspenberg P. Metalloproteinases and their inhibitors-diagnostic and therapeutic opportunities in orthopedics. Acta Orthop. 2009;80(6):693–703.
131. Hou W-S, Li W, Keyszer G, Weber E, Levy R, Klein MJ, et al. Comparison of Cathepsins K and S Expression Within the Rheumatoid and Osteoarthritic

Synovium. Arthritis Rheum. 2002;46(3):663–74.
132. Barry ZT, Platt MO. Cathepsin S Cannibalism of Cathepsin K as a Mechanism to Reduce Type I Collagen Degradation. J Biol Chem. 2012;287(33):27723–30.
133. Parks AN, Nahata J, Edouard N-E, Temenoff JS, Platt MO, Coulter WH. Sequential, but not Concurrent, Incubation of Cathepsin K and L with type I Collagen Results in extended proteolysis. Sci Rep. 2019;9(1):1–12.
134. Ye M, Kim S, Park K. Issues in long-term protein delivery using biodegradable microparticles. Vol. 146, Journal of Controlled Release. 2010. p. 241–60.
135. Hennink WE, van Nostrum CF. Novel crosslinking methods to design hydrogels. Vol. 64, Advanced Drug Delivery Reviews. 2012. p. 223–36.
136. Doroski DM, Levenston ME, Temenoff JS. Cyclic Tensile Culture Promotes Fibroblastic Differentiation of Marrow Stromal Cells Encapsulated in Poly(Ethylene Glycol)-Based Hydrogels. Tissue Eng Part A. 2010;16(11):3457–66.
137. Qiu Y, Lim JJ, Scott L, Adams RC, Bui HT, Temenoff JS. PEG-based hydrogels with tunable degradation characteristics to control delivery of marrow stromal cells for tendon overuse injuries. Vol. 7, Acta Biomaterialia. 2011. p. 959–66.
138. Campos E, Branquinho J, Carreira AS, Carvalho A, Coimbra P, Ferreira P, et al. Designing polymeric microparticles for biomedical and industrial applications. Vol. 49, European Polymer Journal. 2013. p. 2005–21.
139. Ifkovits JL, Burdick JA. Review: Photopolymerizable and Degradable Biomaterials for Tissue Engineering Applications. Tissue Eng. 2007;13(10):2369–85.
140. Reyes CD, Garcia AJ. Engineering integrin-specific surfaces with a triple-helical collagen-mimetic peptide. J Biomed Mater Res Part A. 2003;65(4):511–23.
141. Browning MB, Cereceres SN, Luong PT, Cosgriff-Hernandez EM. Determination of the in vivo degradation mechanism of PEGDA hydrogels. J Biomed Mater Res - Part A. 2014;102(12):4244–51.
142. Van De Wetering P, Metters AT, Schoenmakers RG, Hubbell JA. Poly(ethylene glycol) hydrogels formed by conjugate addition with controllable swelling, degradation, and release of pharmaceutically active proteins. Vol. 102, Journal of Controlled Release. 2005. p. 619–27.
143. Parlato M, Johnson A, Hudalla GA, Murphy WL. Adaptable poly(ethylene glycol) microspheres capable of mixed-mode degradation. Acta Biomater. 2013;9(12):9270–80.
144. Secret E, Crannell KE, Kelly SJ, Villancio-Wolter M, Andrew JS. Matrix metalloproteinase-sensitive hydrogel microparticles for pulmonary drug delivery of small molecule drugs or proteins. J Mater Chem B. 2015;3:5634.
145. Patterson J, Hubbell JA. Enhanced proteolytic degradation of molecularly engineered PEG hydrogels in response to MMP-1 and MMP-2. Biomaterials. 2010;
146. Rice MA, Anseth KS. Controlling Cartilaginous Matrix Evolution in Hydrogels with Degradation Triggered by Exogenous Addition of an Enzyme. Tissue Eng Eng. 2007;13(4):683–91.
147. Rice MA, Sanchez-Adams J, Anseth KS. Exogenously Triggered, Enzymatic Degradation of Photopolymerized Hydrogels with Polycaprolactone Subunits:

Experimental Observation and Modeling of Mass Loss Behavior. Biomacromolecules. 2006;7:1968–75.
148. Benoit DSW, Collins SD, Anseth KS. Multifunctional hydrogels that promote osteogenic human mesenchymal stem cell differentiation through stimulation and sequestering of bone morphogenic protein 2. Adv Funct Mater. 2007;17(13):2085–93.
149. DuBose JW, Cutshall C, Metters AT. Controlled release of tethered molecules via engineered hydrogel degradation: Model development and validation. J Biomed Mater Res - Part A. 2005;74(1):104–16.
150. Yurt RW, Leid RW, Austen KF, Silbert JE. Native Heparin from Rat Peritoneal Mast Cells. J Biol Chem. 1977;252(2):518–21.
151. Liang Y, Kiick KL. Heparin-functionalized polymeric biomaterials in tissue engineering and drug delivery applications. Vol. 10, Acta Biomaterialia. 2014. p. 1588–600.
152. Hettiaratchi MH, Miller T, Temenoff JS, Guldberg RE, Mcdevitt TC. Heparin microparticle effects on presentation and bioactivity of bone morphogenetic protein-2. Biomaterials. 2014;35:7228–38.
153. Seto SP, Miller T, Temenoff JS, Coulter WH. Effect of Selective Heparin Desulfation on Preservation of Bone Morphogenetic Protein-2 Bioactivity after Thermal Stress. Bioconjug Chem. 2015;26(2):286–93.
154. Sakiyama-Elbert SE. Incorporation of heparin into biomaterials. Acta Biomater. 2014;10(4):1581–7.
155. Xu JH, Dong PF, Zhao H, Tostado CP, Luo GS. The Dynamic Effects of Surfactants on Droplet Formation in Coaxial Microfluidic Devices. Langmuir. 2012;28(9250–9258).
156. Headen DM, Aubry G, Lu H, García AJ. Microfluidic-based generation of size-controlled, biofunctionalized synthetic polymer microgels for cell encapsulation. Adv Mater. 2014;26(19):3003–8.
157. Ricchetti ET, Aurora A, Iannotti JP, Derwin KA. Scaffold devices for rotator cuff repair. J Shoulder Elb Surg. 2012 Feb;21(2):251–65.
158. Konttinen YT, Mandelin J, Li TF, Salo J, Lassus J, Liljeström M, et al. Acidic cysteine endoproteinase cathepsin K in the degeneration of the superficial articular hyaline cartilage in osteoarthritis. Arthritis Rheum. 2002;46(4):953–60.
159. Enwemeka CS. Inflammation, Cellularity, and Fibrillogenesis in Regenerating Tendon: Implications for Tendon Rehabilitation. Phys Ther. 1989;69(10):816–25.
160. Sulejmani F, Pokutta-Paskaleva A, Salazar O, Karimi M, Sun W. Mechanical and Structural Analysis of the Pulmonary Valve in Congenital Heart Defects: A Presentation of Two Case Studies. J Mech Behav Biomed Mater. 2018;
161. Thote T, Lin ASP, Raji Y, Moran S, Stevens HY, Hart M, et al. Localized 3D analysis of cartilage composition and morphology in small animal models of joint degeneration. Osteoarthr Cartil. 2013 Aug;21(8):1132–41.
162. Kupai K, Szucs G, Cseh S, Hajdu I, Csonka C, Csont T, et al. Matrix metalloproteinase activity assays: Importance of zymography. J Pharmacol Toxicol Methods. 2010;61(2):205–9.
163. Xie L, Lin ASP, Levenston ME, Guldberg RE, Woodruff GW. Quantitative assessment of articular cartilage morphology via EPIC-μCT. Osteoarthr Cartil.

17:313–20.
164. Palmer AW, Guldberg RE, Levenston ME, Woodruff GW. Analysis of cartilage matrix fixed charge density and three-dimensional morphology via contrast-enhanced microcomputed tomography. Proc Natl Acad Sci U S A. 2006;103(51):19255–60.
165. Willett NJ, Thote Z T, Hart M, Moran S, Guldberg RE, Kamath R V, et al. Quantitative pre-clinical screening of therapeutics for joint diseases using contrast enhanced micro-computed tomography. 2016;
166. Killian ML, Cavinatto L, Shah SA, Sato EJ, Ward SR, Havlioglu N, et al. The effects of chronic unloading and gap formation on tendon-to-bone healing in a rat model of massive rotator cuff tears. J Orthop Res. 2014;32(3):439–47.
167. Buckland-Wright C, Sc D. Subchondral bone changes in hand and knee osteoarthritis detected by radiography. Osteoarthr Cartil. 2004;12:10–9.
168. Reece DS, Thote T, Lin ASP, Willett NJ, Guldberg RE. Contrast enhanced μCT imaging of early articular changes in a pre-clinical model of osteoarthritis. Osteoarthr Cartil. 2018;26(1):118–27.
169. Bose K. Proteases in Apoptosis: Pathways, Protocols and Translational Advances. 2015.
170. Keppler D, Walter R, Perez C, Sierra F. Increased expression of mature cathepsin B in aging rat liver. Cell Tissue Res. 2000;302:181–8.
171. Drake FH, Dodds RA, James IE, Connor JR, Debouck C, Richardson S, et al. Cathepsin K, but Not Cathepsins B, L, or S, Is Abundantly Expressed in Human Osteoclasts. J Biol Chem. 1996;271(21):12511–6.
172. Krieger JR, Ogle ME, Mcfaline-Figueroa J, Segar CE, Temenoff JS, Botchwey EA, et al. Spatially localized recruitment of anti-inflammatory monocytes by SDF-1α-releasing hydrogels enhances microvascular network remodeling. Biomaterials. 2016;77:280–90.
173. Quinlan E, López-Noriega A, Thompson E, Kelly HM, Cryan SA, O'Brien FJ. Development of collagen-hydroxyapatite scaffolds incorporating PLGA and alginate microparticles for the controlled delivery of rhBMP-2 for bone tissue engineering. Vol. 198, Journal of Controlled Release. 2015. p. 71–9.
174. Maleki M, Ghanbarvand F, Behvarz MR, Ejtemaei M, Ghadirkhomi E. Comparison of mesenchymal stem cell markers in multiple human adult stem cells. Int J Stem Cells. 2014;7(2):118–26.
175. Sharma RR, Pollock K, Hubel A, McKenna D. Mesenchymal stem or stromal cells: A review of clinical applications and manufacturing practices. Transfusion. 2014;54(5):1418–37.
176. Novinec M, Grass RN, Stark WJ, Turk V, Baici A, Lenarčič B. Interaction between Human Cathepsins K, L, and S and Elastins Mechanism Of Elastinolysis And Inhibition By Macromolecular Inhibitors. 2007;
177. Mealy JE, Rodell CB, Burdick JA. Sustained Small Molecule Delivery from Injectable Hyaluronic Acid Hydrogels through Host-Guest Mediated Retention. J Mater Chem B. 2015;3(40):8010–9.
178. Pritchard EM, Valentin T, Boison D, Kaplan DL. Incorporation of proteinase inhibitors into silk-based delivery devices for enhanced control of degradation and drug release. Vol. 32, Biomaterials. 2011. p. 909–18.

179. Goutallier D, Postel JM, Bernageau J, Lavau L, Voisin MC. Fatty muscle degeneration in cuff ruptures. Pre- and postoperative evaluation by CT scan. Clin Orthop Relat Res. 1994;(304):78—83.
180. Matsen F. Clinical practice. Rotator-cuff failure. Artic New Engl J Med. 2008;
181. Matava MJ, Purcell DB, Rudzki JR. Partial-Thickness Rotator Cuff Tears. Am J Sports Med. 2005;33(9):1405–17.
182. Page-Mccaw A, Ewald AJ, Werb Z. Fibrillar collagen Enzymatic redundancy Enzymatic compensation Matrix metalloproteinases and the regulation of tissue remodelling. Nat Rev | Mol CELL Biol. 2007;8.
183. Konttinen YT, Mandelin J, Li TF, Salo J, Lassus J, Liljeström M, et al. Acidic cysteine endoproteinase cathepsin K in the degeneration of the superficial articular hyaline cartilage in osteoarthritis. Arthritis Rheum. 2002;46(4):953–60.
184. Doan TN, Bernard FC, McKinney JM, Dixon JB, Willett NJ. Endothelin-1 inhibits size dependent lymphatic clearance of PEG-based conjugates after intra-articular injection into the rat knee. Acta Biomater. 2019;93:270–81.
185. Weiler M, Kassis T, Dixon JB. Sensitivity analysis of near-infrared functional lymphatic imaging. J Biomed Opt. 2012;17(6):066019.
186. Razavi MS, Nelson TS, Nepiyushchikh Z, Gleason RL, Dixon JB. The relationship between lymphangion chain length and maximum pressure generation established through in vivo imaging and computational modeling. Am J Physiol - Hear Circ Physiol. 2017;313(6):H1249–60.
187. Miranda MO, Bureau NJ. Supraspinatus Myotendinous Junction Injuries: MRI Findings and Prevalence. Am J Roentgenol. 2019;212(1):W1–9.
188. Sato EJ, Killian ML, Choi AJ, Lin E, Esparza MC, Galatz LM, et al. Skeletal muscle fibrosis and stiffness increase after rotator cuff tendon injury and neuromuscular compromise in a rat model. J Orthop Res. 2014 Sep 1;32(9):1111–6.
189. Boerckel JD, Kolambkar YM, Dupont KM, Uhrig BA, Phelps EA, Stevens HY, et al. Effects of protein dose and delivery system on BMP-mediated bone regeneration. Vol. 32, Biomaterials. 2011. p. 5241–51.
190. Wilcox D, Mason RW. Inhibition of cysteine proteinases in lysosomes and whole cells. Biochem J. 1992;285(2):495–502.
191. Riggin CN, Chen M, Gordon JA, Schultz SM, Soslowsky LJ, Khoury V. Ultrasound-Guided Dry Needling of the Healthy Rat Supraspinatus Tendon Elicits Early Healing Without Causing Permanent Damage. J Orthop Res. 2019;37(9):2035–42.
192. Meyer DC, Pirkl C, Pfirrmann CWA, Zanetti M, Gerber C. Asymmetric atrophy of the supraspinatus muscle following tendon tear. J Orthop Res. 2005;23(2):254–8.
193. Visse R, Nagase H. Matrix metalloproteinases and tissue inhibitors of metalloproteinases: Structure, function, and biochemistry. Circ Res. 2003;92(8):827–39.
194. Sheikh Z, Brooks PJ, Barzilay O, Fine N, Glogauer M, Stampfl J. Macrophages, Foreign Body Giant Cells and Their Response to Implantable Biomaterials. Materials (Basel). 2015;8:5671–701.
195. Vasiliauskas R, Liu D, Cito S, Zhang H, Shahbazi M-A, Sikanen T, et al. Simple Microfluidic Approach to Fabricate Monodisperse Hollow Microparticles for

Multidrug Delivery. Appl Mater Interfaces. 2015;7:14822–32.
196. Duncanson WJ, Lin T, Abate AR, Seiffert S, Shah RK, Weitz DA. Microfluidic synthesis of advanced microparticles for encapsulation and controlled release. Lab Chip. 2012;12:2135–45.
197. Wilde CG, Hawkins PR, Coleman RT, Levine WB, Delegeane AM, Okamoto PM, et al. Cloning and Characterization of Human Tissue Inhibitor of Metalloproteinases-3. 1994;13(7):711–8.
198. Mancuso P, Raman S, Glynn A, Barry F, Murphy JM. Mesenchymal Stem Cell Therapy for Osteoarthritis: The Critical Role of the Cell Secretome. Front Bioeng Biotechnol. 2019;7(9):1–9.
199. van Rooijen N, Hendrikx E. Liposomes for specific depletion of macrophages from organs and tissues. In: Liposomes. Springer; 2010. p. 189–203.